The Huckleberry Ridge Tuff, Yellowstone: evacuation of multiple magmatic systems in a complex episodic eruption

Elliot J. Swallow[1], Colin J. N. Wilson[1,*], Bruce L. A. Charlier[1] and John A. Gamble[1,2]

[1]School of Geography, Environment and Earth Sciences, Victoria University, PO Box 600, Wellington 6140, New Zealand

[2]School of Biological, Earth & Environmental Sciences, University College Cork, Cork, Ireland

*Corresponding author

Email address; colin.wilson@vuw.ac.nz

ABSTRACT

The 2.08 Ma, ~2,500 km^3 Huckleberry Ridge Tuff (HRT) eruption, Yellowstone, generated two fall deposits and three ignimbrite members (A, B, C), accompanying a ~95 x 65 km caldera collapse. Field data imply that the pre-A fall deposits took weeks to be erupted, then breaks of weeks to months occurred between members A and B, and years to decades between B and C. We present compositional and isotopic data from single silicic clasts (pumice or fiamme) in the three ignimbrite members, plus new data from co-eruptive mafic components to reconstruct the nature and evacuation history of the HRT crustal magmatic complex. Geochemical data, building on field characteristics, are used to group nine silicic clast types into seven compositional suites (A1-A3; B1; C1-C3) within their respective members A, B and C. Isotopic data are then added to define four magmatic systems that were tapped simultaneously and/or sequentially during the eruption. Systems 1 and 2 fed the initial fall deposits and then vented throughout member A, accompanied by trace amounts of mafic magma. In member A, volumetrically dominant system 1 is represented by a rhyolite suite (A1: 73.0-77.7 wt % SiO_2, 450-1680 ppm Ba) plus a distinct low-silica rhyolite suite (A2: 69.2-71.6 wt % SiO_2, >2,500 ppm Ba). System 2 yielded only a low-Ba, high-silica rhyolite suite (A3: 76.7-77.4 wt % SiO_2, ≤250 ppm Ba). Glass compositions in pumices from systems 1 and 2 show clustering, indicative of the same multiple melt-dominant bodies identified in the initial fall deposits and earliest ignimbrite. Member B samples define suite B1 (70.7-77.4 wt % SiO_2, 540-3040 ppm Ba) derived from magmatic system 1 (but not 2) that had undergone mixing and reorganisation during the A:B time break, accompanying mafic magma inputs. Mafic scoria erupted in upper member B cover similar compositions to the member A clasts, but extend over a much broader compositional range. Member C clast compositions reflect major changes during the B:C time break, including rejuvenation of magmatic system 2 (last seen in member A) as suite C3 (75.3-77.2 wt % SiO_2, 100-410 ppm Ba), plus the appearance of two new suites with strong crustal signatures. Suite C2 is another rhyolite (74.7-77.6 wt % SiO_2, with Ba decreasing with silica from 2840 to 470 ppm) that defines magmatic system 3. Suite C2 also shows clustered glass compositions, suggesting that multiple melt-dominant bodies were a repetitive feature of the HRT magmatic complex. Suite C1, in contrast, is dacite to rhyolite (65.6-75.0 wt % SiO_2, with Ba increasing with silica from 750 to 1710 ppm) that defines magmatic system 4. Compositions from magmatic systems 1 and 2 dominantly reflect fractional crystallisation, but include partial melting of cumulates related to earlier intrusions of the same mafic magmas as those syn-eruptively vented. Country rock assimilation was limited to minor amounts of a more radiogenic (with

respect to Sr) evolved contaminant. In contrast, systems 3 and 4 show similar strongly crustal isotopic compositions (despite their differences in elemental composition) consistent with assimilation of Archean rocks via partial melts derived from cumulates associated with contrasting mafic lineages. System 3 links to the same HRT mafic compositions co-erupted in members A and B. In contrast, system 4 links to olivine tholeiite compositions erupted in the Yellowstone area before, sparsely during, and following the HRT itself. All four magmatic systems were housed beneath the HRT caldera area. Systems 1 and 2 were hosted in Archean crust that had been modified by Cretaceous/Eocene magmatism, whereas systems 3 and 4 were hosted within crust that retained Archean isotopic characteristics. The extreme compositional diversity in the HRT highlights the spatial and temporal complexities that can be associated with large-volume silicic magmatism.

Keywords: Huckleberry Ridge Tuff; rhyolite; radiogenic isotopes; Yellowstone; magmatic systems

INTRODUCTION

Quaternary silicic (dacite to rhyolite in this context) magmatic systems have generated many caldera-forming explosive eruptions that would lead to global impacts and consequences if repeated today (Mason *et al*., 2004; Self, 2006). The largest of these (supereruptions) involve the eruption of >10^{15} kg (~450 km^3) of magma (Sparks *et al*., 2005; Wark & Miller, 2008). Of necessity, understanding of their crustal magmatic systems has been incrementally developed, through studies of eruption deposits to reconstruct their geochemical nature and infer the characteristics of the parental magmatic system, and through numerical modelling of the generation, accumulation and eruptive triggering of these vast volumes of magma.

Studies of past eruptions have included the analysis of a broad spectrum of erupted materials, including one or more of whole-rock samples (i.e. bulk welded ignimbrite: e.g. Hildreth *et al*., 1984, 1991), single clasts (i.e. individual pumice/fiamme: e.g. Bacon & Druitt, 1988; Streck & Grunder, 1997; Hildreth & Wilson, 2007; Folkes *et al*., 2011), crystal cargoes (e.g. Bindeman *et al*., 2008; Ellis & Wolff, 2012; Rivera *et al*., 2014; Wolff & Ramos, 2014) and glass compositions (e.g. Nash *et al*., 2006; Roberge *et al*., 2013; Westgate *et al*., 2013). These works and others have highlighted significant diversity in silicic volcanism. A majority of silicic eruption deposits fall into two categories. First there are crystal-rich dacites, which

are relatively homogeneous on the bulk-rock scale (e.g., Fish Canyon Tuff, Colorado; Bachmann *et al*., 2002) and have been labelled 'monotonous intermediates' (Hildreth, 1981; Christiansen, 2005; Bachmann & Bergantz, 2008; Bachmann & Huber, 2016). These are thought to represent rejuvenation/mobilisation of a crystal-rich magmatic mush body (e.g. Huber *et al*., 2011, 2012; Parmigiani *et al*., 2014). Second, there are crystal-poor rhyolites that are widely, although not exclusively (e.g. Streck, 2014), thought to represent rhyolitic melts extracted from a crystal-rich mush zone (Brophy, 1991; Bachmann & Bergantz, 2004; Hildreth, 2004) with subsequent minor crystallisation. We focus on the latter here.

Crystal-poor rhyolites generally show some intra-eruptive compositional variations (Hildreth, 1981; Christiansen, 2005; Bachmann & Bergantz, 2008; Bachmann & Huber, 2016). Works reviewed in Hildreth (1981) related whole-rock, single clast, mineral and/or glass compositional heterogeneities and zonations in eruption deposits to the inverted vertical zonation of the magmatic system, and overwhelmingly invoked a single magma body as the source. Subsequent work has used this framework to explain compositional variations in a similar way, whether those variations are gradational (e.g. Bishop Tuff, California: Hildreth & Wilson, 2007, Chamberlain *et al*., 2015; Carpenter Ridge Tuff, Colorado: Bachmann *et al*., 2014) or stepwise (e.g. Crater Lake, Oregon: Bacon & Druitt, 1988; Rattlesnake Tuff, Oregon: Streck & Grunder, 1997; Grizzly Peak Tuff, Colorado: Fridrich & Mahood, 1987). This compositional variability has, in turn, been related to variations in T, fO_2 and H_2O in the magmatic system that are manifested in one or more of: fractional crystallisation-controlled evolution of the magma (e.g. Streck & Grunder, 1997; Hildreth & Wilson, 2007; Chamberlain *et al*., 2015), variations in crystal contents (e.g., Bacon & Druitt, 1988), or partial melting of a crystalline residuum (Deering *et al*., 2011; Wolff *et al*., 2015; Wolff, 2017). In other systems, however, unzoned crystal-poor deposits have also been recorded (e.g. Oruanui, Taupo Volcanic Zone: Wilson *et al*., 2006; Allan *et al*., 2017).

Whether chemically variable or not, eruption deposits are typically inferred to represent the evacuation of a single melt-dominant body. However, some examples show compositional diversity inferred to represent the simultaneous or sequential evacuation of multiple melt-dominant bodies (e.g. Oruanui, Kidnappers/Rocky Hill, and Mamaku-Ohakuri eruptions, Taupo Volcanic Zone: Allan *et al*., 2012; Cooper *et al*., 2012, 2016; Bégué *et al*., 2014; and the Snake River Plain: Ellis & Wolff, 2012; Ellis *et al*., 2014). These bodies, in turn, may be interpreted to represent melt extractions from a unitary, heterogenous mush zone (Bégué *et al*., 2014; Ellis *et al*., 2014) or from multiple magmatic systems (Allan *et al*., 2012; Cooper *et al*., 2012, 2016). In contrast to these complexities, numerical models for such

volcanism focus on the formation and evacuation of a single magma body (e.g., Jellinek & DePaolo, 2003; Gregg *et al*., 2012, 2015; Caricchi *et al*., 2014; de Silva & Gregg, 2014) and do not, therefore, take into account effects of the associated stress field (and hence eruption behaviour) of multiple melt-dominant bodies (Gudmundsson, 2012; Cashman & Giordano, 2014).

The formation of parental magma bodies to super-eruptions is typically inferred to take of the order of 10^5-10^6 years (e.g. Jellinek & DePaolo, 2003). This arises from a presumption of a relationship between eruption size and the pre-eruptive repose period (Smith, 1979; Reid, 2008) although other studies demonstrate no such relationship exists (e.g. Wilson, 1993; Wilson *et al*., 2009). Although some examples show evidence for prolonged accumulation of the melt-dominant body (e.g. Crater Lake: Bacon, 1983; Bishop Tuff: Chamberlain *et al*., 2014a), others have demonstrated very rapid accumulation (e.g. Oruanui and Taupo: Wilson & Charlier, 2009; Allan *et al*., 2013, 2017; Pamukcu *et al*., 2015; Barker *et al*., 2016). In addition, there is also evidence for the rapid (sometimes decadal) recovery and regeneration of magmatic systems following large caldera-forming eruptions (e.g., Barker *et al*., 2014, 2016; Cooper *et al*., 2016, 2017; Hildreth *et al*., 2017). These studies highlight a dichotomy of timescales associated with silicic systems. Although melt-dominant bodies can accumulate rapidly, the generation of their chemical signatures, through some combination of fractional crystallisation, assimilation, or magma mixing (Christiansen & McCurry, 2008; Bindeman & Simakin, 2014), is a longer term process, as indicated by the long-term broad chemical similarities of erupted materials (e.g. Mazama: Bacon, 1983; Taupo: Barker *et al*., 2015; Bruneau-Jarbidge: Cathey & Nash, 2004; Yellowstone: Girard & Stix, 2010, Loewen & Bindeman, 2015; Stelten *et al*., 2015; Troch *et al*., 2017). Broad chemical uniformity may be observed over long periods at such systems that masks the diversities seen on smaller scales in isotopic and/or crystal compositions. Such diversities may indicate that the melt-dominant bodies result from amalgamation of melt and/or crystals from a wide range of sources, including silicic fractionates from mafic precursors, partial melts of solidified intrusions and enriched partial melts from silicic country rocks (e.g. Bindeman *et al*., 2008; Charlier *et al*., 2008; Christiansen & McCurry, 2008; Wolff & Ramos, 2014; Stelten *et al*., 2017). A constant factor amongst these diversities, however, is the role of mafic magma, which provides thermal and chemical inputs into silicic systems, modulating their behaviour and potentially triggering eruption (e.g. Sparks *et al*., 1977; Hildreth, 1981; Loewen & Bindeman, 2015; Barker *et al*., 2015, 2016; Till *et al*., 2015; Stelten *et al*., 2017).

To provide a case-study of the wide range of possible processes and products in large-scale silicic volcanism and associated magmatism we present a geochemical investigation of the Huckleberry Ridge Tuff (HRT) at Yellowstone. In particular, we document the major element, trace element and isotopic compositions of single pumices, fiamme and their associated groundmass glasses and crystal cargoes, from the three ignimbrite members of the tuff. These results are combined with limited new data from co-erupted mafic materials, plus published information (Myers *et al*., 2016; Swallow *et al*., 2018a, 2018b), to provide insights into the variability of the HRT erupted products, the nature of the multiple magmatic and crustal sources, and the way in which such huge systems are generated and evacuated during a supereruption.

GEOLOGICAL BACKGROUND

Yellowstone Plateau volcanic field

Quaternary volcanic products in the Yellowstone area, including the HRT, are generally grouped together as the Yellowstone Plateau volcanic field (YPVF). The YPVF lies at the eastern end of the Snake River Plain, a 700 km long, ENE-trending volcano-tectonic depression comprising a series of eastward-younging silicic caldera centres and intercalated basaltic lava flows (Armstrong *et al*., 1975; Pierce & Morgan, 1992, 2009). The ~16 Ma to present, time-progressive volcanism, elevated heat flow, fluid geochemistry and tectonic setting are consistent with movement of the North American plate over a stationary mantle plume, with complexities arising from asthenospheric flow around the foundered Farallon slab (Pierce & Morgan, 1992, 2009; Lowenstern & Hurwitz, 2008; James *et al*., 2011; Lowenstern *et al*., 2014; Zhou *et al*., 2018). Volcanism along the Snake River Plain is bimodal, with basaltic lavas (dominantly olivine tholeiites) and high-silica rhyolitic lavas and tuffs forming nearly all the eruption products (Christiansen, 2001; Christiansen & McCurry, 2008).

The ~2.1 Ma history of the YPVF is grouped into three volcanic cycles, with dominantly effusive, basaltic and silicic activity bracketing three climactic, caldera-forming silicic eruptions, of which the HRT was the first (Christiansen, 2001). Geochemical investigations of YPVF silicic eruptives have primarily focused on (a) whole-rock samples (i.e. whole pieces of welded ignimbrite), either for bulk chemical characteristics (Doe *et al*., 1982; Hildreth *et al*., 1984, 1991; Christiansen, 2001) or focused single-crystal studies (Bindeman & Valley, 2001; Bindeman *et al*., 2008; Ellis *et al*., 2012; Rivera *et al*., 2014, 2016; Singer *et*

al., 2014; Wotzlaw *et al*., 2015); or (b) samples of lavas, principally from younger effusive episodes (Girard & Stix, 2009, 2010; Watts *et al*., 2012; Loewen & Bindeman, 2015; Stelten *et al*., 2015, 2017, 2018; Till *et al*., 2015; Befus & Gardner, 2016; Troch *et al*., 2017). Broad-scale investigations have indicated that the high-silica rhyolites of the YPVF are not simply highly fractionated melts from a mafic precursor, due to the absence of intermediate compositions and the offset between the Sr and Pb isotopic fields of YPVF rhyolites and tholeiitic basalts (Doe *et al*., 1982; Hildreth *et al*., 1991; Christiansen & McCurry, 2008). It was therefore inferred that the rhyolites were derived from partial melting of middle crust comprising Archaean basement and Cenozoic tholeiitic basalt intrusions (Doe *et al*., 1982; Hildreth *et al*., 1991), followed by extensive fractionation of feldspars and ferromagnesian minerals (Christiansen & McCurry, 2008). Heterogeneity observed in the crystal cargoes from single eruptive units attest to a diverse range of initial melt compositions that accumulate and hybridise to smooth out isotopic variations (Bindeman *et al*., 2008; Wotzlaw *et al*., 2015; Stelten *et al*., 2017). Larger-scale variations in isotopic systematics were attributed to shallow (upper crustal) processes, including the partial melting of the foundering magma chamber roof or assimilation of hydrothermally altered country rock (Doe *et al*., 1982; Hildreth *et al*., 1984, 1991; Bindeman & Valley, 2001; Bindeman *et al*., 2008; Troch *et al*., 2018). What is universally accepted, however, is the prominent role mafic magmas play in Yellowstone rhyolitic volcanism (e.g. Hildreth *et al*., 1991), whether through providing chemical and thermal inputs into a long-lived crystal mush zone (Stelten *et al*., 2015), generating melt-dominant bodies through partial melting of upper crustal rocks (Loewen & Bindeman, 2015; Troch *et al*., 2018), providing fractionated melts to the rhyolitic system (Stelten *et al*., 2017), or causing eruptive triggering (Till *et al*., 2015).

Huckleberry Ridge Tuff

The 2.08 Ma, ~2,500 km^3 HRT (Fig. 1) represents the first and largest of the three caldera-forming eruptions in the YPVF (Christiansen, 2001). It comprises three ignimbrite members (A, B and C) and two fall deposits: initial pre-A fall deposits and others between members B and C. The only significant difference from the presentation by Christiansen (2001) is that most of the rheomorphic ignimbrite exposed to the southwest of the caldera is recognised by us as being member A, not member B. The overall published consensus is that the HRT was erupted geologically rapidly from discrete parts of a single, zoned magma body and was

emplaced in thermal terms as a composite sheet (Reynolds, 1977; Christiansen, 1979, 2001; Hildreth *et al*., 1984, 1991).

However, fieldwork by C.J.N. Wilson, to be presented elsewhere, has indicated that the eruption was episodic, with evidence for time breaks observed within and between eruptive deposits (Fig. 2; Supplementary Data Fig. S1). Several lines of evidence point to this conclusion. First, the initial fall deposits display reworking structures and fine ash tops to individual horizons, indicative of episodic activity and hiatuses in the eruption. Coupled with information from volatile concentrations in quartz-hosted melt inclusions and re-entrants that suggest slow magma rise rates, it is inferred that fall deposition occurred over a period of some weeks (Myers *et al*., 2016). Second, there are welding contrasts between members A and B (particularly where deposits are thinnest), and the rheomorphic folding of member A (as recognised by us) is in contrast to a planar member B in exposures along the Teton River valley (Fig. S1). Estimates for the timing of rheomorphism are problematic, but field observations and palaeomagnetic data imply that the folding occurred before any devitrification of member A, and was almost entirely finished by the time member B was emplaced (Embree & Hoggan, 1999; Geissman *et al*., 2010). These constraints suggest a time gap of weeks to months occurred between the emplacement of members A and B. Third, widespread breaks in welding intensity occur across the contact between members B and C, but these are balanced against the fumarolic alteration of pre-C fall deposits (Fig. S1) and/or member C ignimbrite by hot gases from the underlying A+B packages. Using comparisons to the Valley of Ten Thousand Smokes ignimbrite from the 1912 eruption of Katmai, where fumaroles emanating from an ignimbrite of roughly comparable thickness and temperature diminished within years and were largely extinct within 20 years (see summary in Hildreth & Fierstein, 2012), we infer there to be time gap between B and C of years to decades in length. This revised chronostratigraphic framework provides context to the geochemical overview presented here.

Although reported whole-rock major and trace elemental compositional variations are minor, significant isotopic heterogeneity is present (Doe *et al*., 1982; Hildreth *et al*., 1984, 1991; Christiansen, 2001). Whole-rock Sr, Pb and Nd isotopic data show that members A and B are similar, whereas member C is distinctly more crustally influenced, interpreted to reflect the rapid assimilation of a foundering upper crustal chamber roof following eruption of members A and B (Doe *et al*., 1982; Hildreth *et al*., 1984, 1991). However, any crustal contaminant is precluded from being hydrothermally altered, based on the uniformity of whole-rock O isotopic values in the HRT, in sharp contrast to subsequent variations (Hildreth

et al., 1984, 1991). Isotopic heterogeneity is also observed within crystal populations from single HRT samples, with zircons showing clustering in Hf, but smaller variations in O isotopes, interpreted as reflecting a heterogeneous magmatic system comprising distinct magma reservoirs with separately dominant crustal and mantle signatures (Bindeman & Valley, 2001; Bindeman *et al*., 2008; Wotzlaw *et al*., 2015). However, these heterogeneities are difficult to relate to specific magmatic domains due to the lack of sample context, arising from the use of whole-rock samples (as distinct from the individual juvenile clasts used in this study). Diversities in crystal characteristics can thus not be linked to specific magma compositions, only to the broad stratigraphic units. Consequently, current inferences about the architecture of the HRT magmatic system, which is proposed by the above authors to have been heterogeneous and to have undergone rapid formation and evolution, are limited.

Studies on the pre-A fall deposits and basal member A ignimbrite indicated that the upper levels of the HRT silicic magmatic system comprised multiple, laterally-adjacent, discrete, melt-dominant bodies that represented two distinct host magmatic lineages (Myers *et al*., 2016; Swallow *et al*., 2018a). The initial fall stages of the eruption saw the simultaneous and sequential tapping of three melt-dominant bodies before escalating into the evacuation of nine bodies (including the earlier three) at the onset of ignimbrite member A deposition and associated caldera collapse after the eruption of ~50 km^3 of magma (Swallow *et al*., 2018a). However, the nature of these bodies and their two host magmatic lineages was not clear. They could represent:

(a) complexity only within the upper levels of a magmatic system that merged downwards into homogeneity at deeper levels tapped during later stages of the eruption,

(b) two magmatic lineages that remained discrete throughout eruption (e.g. Kidnappers: Cooper *et al*., 2012, 2016), or

(c) the first stages of an increasing magmatic complexity from the fall deposits to later in the eruption (e.g. Mamaku/Ohakuri: Bégué *et al*., 2014).

Here we present data from single pyroclasts from members A, B and C in order to test these three possibilities and provide an overall petrogenetic story for the HRT. For the most part, however, the HRT is densely welded, devitrified and vapour-phase altered. Juvenile materials, that were inferred to have been molten at the time of eruption, were preferentially collected from the limited number of sites where macroscopic glassy clasts were present (Fig. 1; Supplementary Data Electronic Appendix 1), but otherwise fiamme were collected from devitrified but otherwise unaltered tuff. Our data thus delimit the full compositional range and degree of compositional clustering in the silicic juvenile materials, but (unlike in the fall

deposits: Myers *et al*., 2016; Swallow *et al*., 2018a) we are not able to interrogate any systematic compositional zonation that might have been present within the individual ignimbrite members.

In the light of the complexities encountered in the field and subsequently revealed in the analytical data for the silicic materials we present a consistent descriptive framework (Fig. 3). We categorise the sampled juvenile clasts, using field-based observations of clast characteristics (e.g. colour, crystal contents and sizes, pumice textures) and eruptive unit, into nine *types* (Table 1). We then use our geochemical data to group these juvenile materials into seven compositional *suites* that share common features or distinctive trends and are distinct to specific ignimbrite members. The suites in turn are attributed, with the addition of isotopic data, to four distinctive *magma systems* which, together with the mafic components (Swallow *et al*., 2018b and this study) collectively make up the *magmatic complex* that yielded the total juvenile products of the overall HRT eruption.

JUVENILE COMPONENTS OF THE HRT

Members A and B

Juvenile silicic components (abbreviated to J) in members A and B are clasts that range from poorly to extremely vesicular (but are mostly pumice in non-welded tuff). The most common pumice (**type J1**: Table 1; Fig. 4a,b) is white where freshest, tan where thermally oxidised, and exhibits a continuous spectrum in vesicle textures from a rounded, cellular foam through to elongated vesicles yielding a fibrous texture, with common crystal schlieren and 'adobe-type' textures, the latter matching those in some Bishop Tuff pumices (Hildreth & Wilson, 2007). Variations from type J1 pumice (and their equivalent devitrified fiamme) include dense, poorly vesicular juvenile material that, where glassy, is dark grey to black through the exsolution of iron oxide microlites (**type J2**: Fig. 4c). A third type is represented by black to dark brown, poorly vesicular clasts that are visually distinctive through containing 10-20 % euhedral feldspar crystals up to 8-10 mm in length (**type J3**: Fig. 4d). In upper member B (and sparsely in A), mingled clasts occur (**type J4**: Fig. 4e), with centimetre-scale lumps or lenses of scoria plus (occasionally) type J3 material, distributed within type J1 pumice.

The silicic clasts are moderately porphyritic, with 11-22 wt % crystals, but extending to 35 wt % in some samples, as determined through crystal-glass separation using heavy liquids (Supplementary Data Electronic Appendix 2). The crystal phases are generally coarse grained, with single crystals up to 7-8 mm and crystal aggregates or clots occasionally up to 2

cm across. The crystal assemblage is dominated by quartz, sanidine and plagioclase, either as single crystals or crystal aggregates. Ferromagnesian minerals are a minor component, and include pyroxene, olivine and Fe-Ti oxides.

Member C

Juvenile silicic components in member C are visually distinctive, both with respect to each other and to the clast types in members A and B (Table 1; Fig. 4), and are described as five types.

- Non-vesicular black juvenile material occurs as angular to rounded clasts which range in shape from equant in normally welded tuff to highly elongate, stretched clasts in rheomorphic ignimbrite (**type J5**: Table 1; Fig. 4f). These clasts have not been found in non-welded or glassy material. They contain few crystals: sparse feldspar and only rare quartz.
- Material visually identical to type J5 clasts (and labelled here as **type J6** material) is found as minor intrusions (up to tens of metres across) invading densely welded member C ignimbrite in exposures along the northern scarp of the Red Mountains. The intrusions are inferred to be closely related in time to the emplacement of member C as their contacts show crenulated and embayed contacts with the host ignimbrite and have only poorly developed chilled margins. The presence of these intrusions implies a local source beneath this area, and that the corresponding magma suite was able to reach shallow levels in the aftermath of the eruption in a small-scale episode of resurgence.
- Glassy pumices were collected from non-welded to sintered ignimbrite at sites along the Teton River (particularly locality 332: Fig. 1; Supplementary Data Electronic Appendix 1). These clasts are rounded, contain equant vesicles and are crystal-moderate (**type J7**: 11-15 wt % crystals: Fig. 4g). The finer-scale vesicular texture in these pumices and notably smaller crystal sizes preclude them from being simply being pick-ups from earlier deposits.
- Glassy pumices of contrasting appearance to type J7 were collected from the non-welded base of member C at locality 057 (Fig. 1; Supplementary Data Electronic Appendix 1). The clasts are light brown-grey or pale creamy brown in colour, elongate to platey in shape and extremely vesicular, fibrous and crystal-poor to moderate (**type J8**: 7-11 wt % crystals: Fig. 4h).

- Devitrified fiamme (**type J9**) from densely welded, often rheomorphic, ignimbrite in the Red Mountains and on Huckleberry Mountain. The clasts are pale yellow- to mid-grey, often vuggy, are sometimes micro- to macro-spherulitic and contain similar crystal proportions to pumices found elsewhere in non-welded member C (type J8). They contrast with type J5 clasts in being more flattened, and paler in colour due to coarser devitrification micro-textures.

All but one of the juvenile clast types in member C have finer crystal sizes (<3 mm) and crystal-poorer natures (<15 wt % crystals) than nearly all clasts in members A and B. Quartz, commonly bi-pyramidal, and feldspar (both plagioclase and sanidine) dominate, with trace amounts of pyroxene, olivine and Fe-Ti oxides. The exception is pumices that are physically identical to J1-type or to J4-type pumices found in member B and are also chemically similar to those member B pumices (see below for further discussion). These pumices in C have been found only in areas along the Teton River southwest of the caldera where a non-welded top to member B was exposed at the time of member C emplacement. For these reasons we infer that these variant C clasts (labelled 'B-in-C') represent syn-eruptive pick-ups from the non-welded top of member B and are considered in with member B in terms of their compositions.

Juvenile mafic materials

As well as our silicic juvenile clast data, we also present new data from the juvenile mafic materials in members A and B, augmenting the data in Swallow *et al*. (2018b). Juvenile mafic material has not been found in member C deposits. Where found as individual clasts, these are, in general, poorly flattened (even in dense-welded tuff) yet show textures (e.g. chilled margins) indicating that they were quenched against the host tuff. The samples include poorly-vesicular material from parts of member A south of the caldera (including the earliest-erupted material), additional scoria from mingled type J4 pumices from member B south of the caldera, and six scoria clasts from glassy to devitrified (but not vapour-phase altered) member B north of the caldera.

METHODS

Sample selection

All samples analysed are listed in Supplementary Data Electronic Appendix 1. For the silicic materials, glassy pumices were sampled whenever possible, but individual devitrified fiamme

were also sampled to compare with the glassy material. In a few cases (mostly the basal vitrophyre in member A), groundmass glass was sampled from single fiamme where the whole clast could not be extracted. Mafic materials reported in Swallow *et al*. (2018b) represent single clasts. These are devitrified where found in devitrified material of members A and B, but are glassy when contained within glassy pumices sampled in member B. In cases where mingled clasts occur in upper member B, the individual components, distinguished by colour, crystal content and vesicle texture, were broken out separately. The additional mafic samples reported here are from devitrified and glassy material both south and north of the caldera and from members A and B. We stress that this study only uses single clast data, and no whole-rock (i.e. bulk tuff) material was analysed.

Single clast analysis

Samples were washed, trimmed of any adhering matrix and dried before being crushed in a Rocklabs Boyd crusher to ~2 mm diameter. This material was then split. At least 100 g of crushed material, providing a representative sample, was milled using an agate TEMA ring mill to the homogenous fine powder which was then used for major and trace element, and isotopic ratio determinations. Single clast major (and Ba) element abundances were determined by X-Ray Fluorescence (XRF) on fused discs at the Open University, U.K. (OU), and the universities of Auckland (AU) and Waikato (WU), New Zealand, all based on the methods of Ramsey *et al*. (1995). Individual 2 s.d.% relative precisions, determined through repeated analysis of multiple standards in each laboratory, are <3 % for almost all major element oxides, with most <1 %, and offsets from preferred or recommended values are generally <5% for all elements. Samples duplicated between laboratories show offsets of <5 % for all major and minor element oxides >0.1 wt % in abundance with Ba offsets ≤5 % (Supplementary Data Electronic Appendix 3).

Trace element analysis of rock powders was conducted using inductively-coupled plasma mass-spectrometry (ICP-MS) at Victoria University of Wellington, New Zealand (VUW). Due to the zircon-bearing nature of the samples, powders were digested using ammonium fluoride (Hu *et al*., 2013). Solutions were analysed on a ThermoFisher Element2 sector-field ICP-MS at VUW. Concentrations were determined using a calibration curve generated from gravimetric daughter dilutions of a 1 ppm mother solution comprised of certified and traceable standard solutions of all elements of interest. Procedural blanks were <0.1 ppb for all elements, with most close to, or at detection limits. Repeated analyses of rock standards

GSP-2 and JR-1 yielded offsets from preferred values of <10 % for all elements except Ho, Er (<15 %), Y (<20 %) and Zn (>20 %), and 2 s.d.% similarly of <10 % for all elements (Supplementary data Electronic Appendix 3).

For the isotopic work, Sr, Nd, and Pb were separated from the same solution used for trace element determination. Sr and Nd separation methods broadly followed those of Pin *et al*. (2014), whereas for Pb separation, we employed the traditional bromide separation technique on an additional aliquot of the same solution (see Supplementary Data). An aliquot containing ≥200 ng Pb was dissolved in 1M HBr and twice passed through AG1-X8 anion resin. For Nd and Sr, a separate aliquot was initially passed through AG50-WX8 cation resin, to reduce – in the case of the Sr - the abundance of Rb in the samples. This Sr fraction was further purified by passing through Sr-spec resin. Chromatographic separation of Nd from a REE-bearing column cut was undertaken using LN-spec resin.

Isotopic ratio measurements were conducted on the same ThermoFisher Triton Thermal Ionisation Mass spectrometer (TIMS) instrument, initially at the OU and later at VUW. Dried Sr fractions were loaded onto a single Re filament assembly in concentrated HNO_3 and a TaF_2 emitter solution (Birck, 1986; Charlier *et al*., 2006). Measurements were corrected for fractionation to $^{86}Sr/^{88}Sr = 0.1194$, and ^{85}Rb was measured to correct for any ^{87}Rb interference at mass 87 using $^{87}Rb/^{85}Rb = 0.385707$ (Rosman & Taylor, 1998). The average of repeated analyses of NBS987 gave $^{87}Sr/^{86}Sr = 0.710255 \pm 0.0000013$ (2 s.d., $n = 25$). The $^{87}Sr/^{86}Sr$ ratios from different runs were normalised to a common value of 0.71025 for NBS987 (following Thirlwall, 1991). The procedural blank was 200 pg, and considered insignificant compared to the ~1000 ng loaded onto each filament. The fractionation corrected $^{87}Sr/^{86}Sr$ ratios were age-corrected (AC) using 2.08 Ma (Rivera *et al*., 2014; Singer *et al*., 2014; Wotzlaw *et al*., 2015), to account for radiogenic ingrowth due to the large Rb/Sr in some samples.

Nd fractions were loaded onto a double Re filament assembly using HCl and a H_3PO_4 loading solution. The $^{143}Nd/^{144}Nd$ was corrected for instrumental fractionation to $^{146}Nd/^{144}Nd = 0.7219$, and corrected for Ce and Sm interferences using $^{140}Ce/^{142}Ce = 7.97279$ and $^{144}Sm/^{147}Sm = 0.20667$ (Rosman & Taylor, 1998). Repeated analyses of J&M and La Jolla standards yielded values of 0.511818 ± 0.000004 (2 s.d., $n = 26$) and 0.511845 ± 0.000002 (2 s.d., $n = 6$) respectively, both similar to the long-term laboratory average (J&M: 0.511821 ± 0.000002, 2 s.d.) and the value of Thirlwall (1991) for La Jolla (0.511856 ± 0.000007, 2 s.d.).

Procedural blank was 300 pg. We express the Nd isotopic values in ε_{Nd} notation (DePaolo & Wasserburg, 1976) which is calculated from measured $^{143}Nd/^{144}Nd$ ratios by:

$$\varepsilon_{Nd} = \left[\frac{\left(^{143}Nd/^{144}Nd\right)_{meas}}{\left(^{143}Nd/^{144}Nd\right)_{CHUR}} - 1\right] \times 10^4,$$

where the $^{143}Nd/^{144}Nd$ value of CHUR (chondritic uniform reservoir) = 0.51263 (Bouvier *et al*., 2008).

Pb fractions were analysed using the double-spike method (Todt *et al*., 1996). After column chemistry, the sample was divided and half loaded onto a single Re filament using a H_3PO_4-silica gel mix loading solution (Gerstenberger & Haase, 1997). Subsequently, the remaining half was mixed with the loading solution and a $^{207}Pb/^{204}Pb$ spike, then loaded onto a separate filament (Thirlwall, 2000). The unspiked natural and spiked samples were analysed during separate analytical sessions, followed by deconvolution using a modified Newton-Raphson inversion to determine the isotopic ratios. Values for standard NBS981 were $^{206}Pb/^{204}Pb = 16.945 \pm 0.001$, $^{207}Pb/^{204}Pb = 15.503 \pm 0.001$ and $^{208}Pb/^{204}Pb = 36.737 \pm 0.004$ (2 s.d., $n = 32$). Isotopic measurements from different analytical sessions were normalised to the NBS981 values of Todt *et al*. (1996). The procedural blank was 2 ng, considered insignificant when compared to the >200 ng analysed and thus no blank correction was applied.

In situ analysis

The remaining crushed material was sieved to 1 mm and any >1 mm crystals picked out. Material from glassy, non-mingled pumices was then immersed in lithium polytungstate heavy liquid (adjusted to ~2.4 g/cm^3) to separate glass and crystals. Weights of the starting materials and separated crystals were recorded in order to derive the crystal wt %. Samples were subsequently dry-sieved at 0.5 mm and wet-sieved at 250, 125 and 63 μm mesh. Crystals were picked from the 0.5-1 mm size fraction and set in 25 mm epoxy mounts with the crystals oriented parallel to their *c*-axes where possible. Glass was picked from the 250-500 μm sieve fraction and similarly mounted. The mounts were polished, coated with a ~25 nm carbon film and analysed by wavelength dispersive electron probe microanalysis (EPMA) on a JXA 8230 Superprobe at VUW. All samples were initially imaged using backscattered electron imaging. Crystals were analysed using a 15 kV accelerating voltage, a 12 nA beam

current, and a ~1 μm spot size. All elements in feldspars and pyroxenes were analysed with 30 s count time on peak and a 15 s background count. Ti, Si, Mg, Fe and Al in olivines were similarly analysed with 30/15 s count times, whereas Ca, Mn and Ni were analysed over 60 s (peak) and 30 s (background) to improve precision and accuracy. Glass was analysed using a 15 kV accelerating voltage and a defocused 20 μm spot size. To reduce the effect of alkali migration a 2 nA beam current was used to analyse Si, Al, Na, K, Fe and Ca, with Si and Na analysed first, as recommended by Humphreys *et al*. (2006). Ti, Mg and Mn were then analysed using an 8 nA current. Peak and background count times were 15/8 (Na), 30/15 (Si, Al), 40/20 (K, Ca, Ti, Mg) and 60/20 s (Fe, Mn). Unknown samples were bracketed by internationally accredited samples to monitor accuracy and precision of the analytical sequence and to monitor instrumental drift. Standards data are given in Supplementary Data Electronic Appendices 4 and 5.

In situ trace element analysis of glass fragments derived from crushed pumices, encompassing the same area as analysed by EPMA, was conducted at VUW using laser ablation inductively-coupled plasma mass spectrometry (LA-ICP-MS) on a RESOlution S155-SE 193 nm Excimer Laser coupled with an Agilent 7500CS ICP-MS. Two 70 μm diameter pre-ablation pulses were used to clean the sample surface at the site of ablation, followed by analysis using a 35 μm spot. Synthetic glass GSD-1G was used for calibration of ^{29}Si concentrations, derived from EPMA analyses, and used as an internal standard. NIST 612, BCR-2G and BHVO-2G were also analysed repeatedly as secondary standards. Unknown samples were bracketed by calibration and secondary standards. Data were processed using LaserTRAM software (Loewen & Kent, 2012) to derive concentrations. Standard data are given in Supplementary Data Electronic Appendix 4.

SINGLE CLAST GEOCHEMISTRY

Major elements

The silicic juvenile materials reported here show a wide diversity, from dacite to high-silica rhyolite (66-79 wt % SiO_2, recalculated volatile free: Table 2; Supplementary Data Electronic Appendix 3). A number of distinct trends are observed for major (and trace) element compositions, even within single ignimbrite members, and we define seven suites (A1, A2, A3, B1, C1, C2, C3) based on their compositional characteristics and trends; these are letter-labelled by their host ignimbrite member. In general, the physical appearances and host

stratigraphic units of the nine clast types are closely reflected in their compositional characteristics and groupings into the seven suites.

- **Suite A1** incorporates most of the type J1 pumices and fiamme (see Table 1) found in member A. Suite A1 forms a coherent trend (73.0-77.7 wt % SiO_2; Figs 5-7; Supplementary Data Figs S2-S4) that is elevated in alkalis ($Na_2O + K_2O$ = 8.3-9.3 wt %) and Al_2O_3 (11.7-13.8 wt %) but depleted in Fe_2O_3 (1.2-3.0 wt %), P_2O_5 (0.01-0.04 wt %) and TiO_2 (0.09-0.39 wt %) relative to other HRT juvenile materials.
- **Suite A2** is represented by the visually distinctive type J3 clasts with their large intact feldspars, plus a lesser number of clasts which visually resemble the other J1 clasts in having fragmented and/or aggregated feldspar/quartz crystals. Collectively, these clasts are chemically distinctive with 69.2-71.6 wt % SiO_2. Suite A2 is enriched in Al_2O_3 (13.8-14.9 wt %), Fe_2O_3 (3.8-5.0 wt %) and TiO_2 (0.39-0.57 wt %), but slightly depleted in total alkalis ($Na_2O + K_2O$ = 8.5-9.2 wt %) relative to the least-evolved end of suite A1 (Figs 5-7; Supplementary Data Figs S2-S4), with an intervening compositional gap.
- **Suite A3** covers a narrow range of compositions that is continuous with the most-evolved end of suite A1 on the basis of major elements (e.g. 76.7-77.2 wt % SiO_2, 11.9-12.4 wt % Al_2O_3: Figs 5-7; Supplementary Data Figs S2-S4), but is separated out on the basis of trace elements, particularly Ba (see below).
- **Suite B1** is represented by a single compositional trend in member B. Suite B1 comprises clasts of types J1 (including the 'B in C' samples found as pick-ups in member C), J3 and the rhyolitic component in type J4. Suite B1 compositions cover most of the compositional range seen in member A (suites A1 and A2) but with no compositional gap evident (e.g. 70.6-77.4 wt % SiO_2, 11.4-13.8 wt % Al_2O_3, 1.5-4.6 wt % Fe_2O_3, 7.1-9.1 wt % $Na_2O + K_2O$: Figs 5-7; Supplementary Data Figs S2-S4), setting aside two anomalous (slightly silicified) samples (Supplementary Data Electronic Appendix 3).
- **Suite C1**: dacite to rhyolite (66-75 wt % SiO_2) that is represented by clast types J5 and J6. Suite C1 is notably enriched in CaO (1-4 wt %), Fe_2O_3 (3.6-11.5 wt %) and P_2O_5 (0.03-0.39 wt %), and depleted in Al_2O_3 (11.4-12.1 wt %) relative to compositions from members A and B (Figs 5-7; Supplementary Data Figs S2-S4). At its silica-rich end, this suite overlaps with part of suite C2.

- **Suite C2**: high-silica rhyolite (75-78 wt % SiO_2) that is represented by clast types J8 and J9, with rare type J5 examples. This suite is moderate in its Fe_2O_3 (1.3-3.3 wt %) and TiO_2 contents (0.12-0.29 wt %: Supplementary Data Figs. S2, S3).
- **Suite C3**: another high-silica rhyolite suite (75-77 wt % SiO_2), represented by clast type J7. It is further depleted in Fe_2O_3 (1.6-1.8 wt %) and TiO_2 (0.10-0.11 wt %) relative to suites C1 and C2 (Figs. S2, S3) and is closely similar to suite A3 compositions from member A.

Compositional suites A1, A2, B1, and C2 in their major element characteristics trend back towards HRT mafic compositions (Swallow *et al*., 2018b), whereas suite C1 shows a marked contrast, leading to bifurcations in many of the major element plots. All member C suites are depleted in total alkalis relative to the suites in members A and B (C1 and C3: $Na_2O + K_2O$ = 7.4-8.6 wt %) with suite C1 particularly so ($Na_2O + K_2O$ = 5.0-7.1 wt %: Fig. 5). Overall, there are no discernible differences in major element compositions between devitrified and glassy pumice and fiamme, and in particular there are no signs of significant alkali mobility. Although pumices typically have higher loss on ignition (LOI) measurements, K/Na ratios, which would be expected to increase with hydration (Hildreth & Wilson, 2007), broadly overlap (Supplementary Data Fig. S5). Higher LOI values (3-5.6 wt %) in some clasts (including mafic clasts) seem to partly reflect minor contamination by a carbonate phase, identified in greater amounts (up to ~20 wt %) in other clasts (data not presented here) from thin section inspection and testing with dilute acid.

Trace elements

The trace element characteristics of the HRT silicic samples show extraordinary diversity (Table 2; Supplementary Data Electronic Appendix 3) and link to the compositional suites identified primarily from field observations of pyroclast types and their major element compositions. In particular, Ba abundances measured by XRF in all samples highlight these groupings (Fig. 8). In member A, suite A2 is Ba-rich (2540-4170 ppm) and distinct from suite A1. A low-Ba cluster of analyses distinguishes suite A3 (Ba = 49-300 ppm) from the A1 suite (Ba = 410-2400 ppm). The trace element characteristics of member B samples, as with major elements, define a single suite (B1: Ba = 540-3040 ppm), but highest and lowest Ba abundances comparable to suites A2 and A3, respectively, are absent. In contrast, the three suites in member C based on major element compositions are also delineated in Ba

abundances (C1 = 750-1710 ppm; C2 = 450-2840 ppm; C3= 100-280 ppm). Notably, the last of these is closely comparable to the A3 suite in its low values.

Full trace element analyses for selected samples that were chosen on the basis of their XRF Ba concentrations were conducted by solution ICP-MS (Supplementary Data Electronic Appendix 3). Suite A1 clasts show wide compositional variation in many trace elements (e.g. 110-162 ppm Rb, 16-60 ppm Sr, 158-347 ppm Zr, 40-56 ppm Nb: Figs 8-11, Supplementary Data Figs S6-S8). Weak compositional gaps distinguish suites A1 from A2 (69-110 ppm Rb, 76-100 ppm Sr, 509-704 ppm Zr, 40-46 ppm Nb) and A3 (161, 201 ppm Rb, 12 ppm Sr, 155, 158 ppm Zr, 53, 61 ppm Nb). Coherency in major-element compositions within the B1 suite is mirrored in the trace elements, with compositions straddling the A1-A2 divide but not extending to the most extreme compositions present in suites A2 or A3 (overall 59-173 ppm Rb, 15-67 ppm Sr, 149-488 ppm Zr; Figs 8, Supplementary Data Figs S6-S8).

Member C suites are distinct in other trace elements both from each other and (with one exception) from the suites in members A and B. Suite C1 is characterised by overall higher Sc (4.7- 46 ppm) and Sr (182 -321 ppm), lower Ba (750 -1710 ppm) and comparable Zr (310 - 890 ppm) concentrations with respect to the maximum concentrations of members A and B suites (Figs 8, 9, 11, S7), with the latter two positively correlated with SiO_2. Suite C2 exhibits large ranges in trace elements over small ranges in SiO_2. This suite is characterised by Ba (470-2380 ppm), Sr (17-120 ppm) and Zr (200-360 ppm) values that are negatively correlated with SiO_2 (Figs 8, 9, S7). Both suites C1 and C2 are distinctly lower in Nb (17-33 ppm: Fig. 10) relative to the suites from members A and B. Suite C3 is, however, comparable to suite A3 in most elements (e.g. 100-280 ppm Ba, 5-42 ppm Sr, 59-66 ppm Nb, 166-189 ppm Zr: Figs 8-10; Supplementary Data Fig. S7).

Chondrite-normalised (McDonough & Sun, 1995) rare-earth element (REE) diagrams for materials from members A, B and C are shown in Fig. 12. Juvenile clasts from suites A1-3 and B1 in members A and B have broadly similar patterns, with moderate light-REE enrichments (La/Yb = 12-21; Fig. 12). Distinctions between suites are observed in Eu anomalies (where $Eu^* = Eu_N / [Sm_N \times Gd_N]^{0.5}$) in member A suites (A1 = 0.25-0.56; A2 = 0.94; A3 = 0.12-0.18); but Eu* has a narrower but continuous range in suite B1 (0.26-0.90). Suite C1 samples have flatter REE patterns than the suites in members A and B (La/Yb = 11-15) with small, both positive and negative, Eu anomalies (Eu* = 0.80-1.18). Suite C2 has similarly flat trends (La/Yb = 11-20) but more variable Eu anomalies (Eu* = 0.24-1.25). In contrast, suite C3 has flatter REE trends (La/Yb = 6-10) relative to other member C suites

and its suite A3 comparator, but a strong negative Eu anomaly (Eu* = 0.11-0.16), comparable to that in suite A3.

New data from juvenile mafic components

We also present new data from mafic materials in the HRT beyond that given in Swallow *et al*. (2018b; Supplementary Data Electronic Appendix 3). The three materials represented by these data fall into somewhat different compositional areas. Dense to poorly vesicular mafic clasts from member A scatter over a wider field than previously reported, although with some remaining coherent trends (e.g. P_2O_5, Fe_2O_3, TiO_2, CaO, Nb, Sc; Figs 7, 10, 11, Supplementary Data Figs S2-S4). Scoria enclaves from type J4 pumices at locations south of the caldera plot in with the other examples shown by Swallow *et al*. (2018b). However, the scoria from upper member B sampled north of the caldera plots along trends for some elements that contrast sharply with the other mafic clast data. In particular, P_2O_5, Fe_2O_3, TiO_2, Ba, Sr, and Zr have lower abundances and form coherent trends for some clasts that generally align with compositions in the olivine tholeiite field (Figs 5, 7-9; Supplementary Data Figs S2-S4) defined from lavas erupted before and after the HRT (Swallow *et al*., 2018b). Juvenile materials with any kind of tholeiitic affinity had not previously been recognised to be co-erupted with the HRT. The more silicic of the HRT mafic compositions overlap in SiO_2 contents with the melt inclusion compositions reported by Szymanowski *et al*. (2015), but have sharply contrasting characteristics with respects to other major and trace elements that preclude direct comparisons.

Isotopic ratios

Single-clast, age-corrected hereafter (to 2.08 Ma) values of $^{87}Sr/^{86}Sr$ in clasts from members A and B are clustered (0.70958-0.71256: Table 3; Supplementary Data Electronic Appendix 3) with suite A2 clasts falling at the less radiogenic end of the spectrum (0.70958-0.71009: Fig. 13). $^{87}Sr/^{86}Sr$ ratios show correlations with indicators of melt evolution, e.g., positive with Rb/Sr and negative with Ba, with the trend levelling off at higher Rb/Sr and lower Ba values (Fig. 14). Suite C3 clasts are less radiogenic than the suites in members A and B for a given elemental value (e.g. 1/Sr) and exhibit a flat trend with indicators of magma evolution (e.g. Rb/Sr). In sharp contrast, all other member C juvenile components are significantly more radiogenic, as first recognised by Doe *et al*. (1982). $^{87}Sr/^{86}Sr$ values range from 0.72465-0.73026 in clasts ranging from dacite to high-silica rhyolite (Figs. 13, 14). These

samples show a weak positive correlation between isotopic ratios and Rb/Sr and 1/Sr, but similar isotopic ratios across significantly different Ba abundances.

Similar relationships are observed in the Nd isotopic compositions measured on the same dissolutions of the same samples. Samples from members A and B have $^{143}Nd/^{144}Nd$ ratios from 0.51214-0.51220 (ε_{Nd} = -8.5 to -9.6), that are negatively correlated with $^{87}Sr/^{86}Sr$ (Fig. 13). Suite C3 sample YP133 has $^{143}Nd/^{144}Nd = 0.51214 \pm 0.000001$ (2 se; ε_{Nd} = -9.5), identical to suite A3 sample YP255. Other juvenile samples from suites C1 and C2 in member C are less radiogenic: $^{143}Nd/^{144}Nd$ ratios range from 0.51174-0.51170 (ε_{Nd} = -17.3 to -18.2) and are negatively correlated with $^{87}Sr/^{86}Sr$ (Fig. 13). There is no variation in Nd isotopic compositions with any elemental measures of magmatic evolution (e.g. Ba: Supplementary Data Fig. S9).

Pb isotopic compositions of members A and B samples are tightly clustered (Fig. 15), with positive correlations observed between $^{206}Pb/^{204}Pb$ (16.90-17.02), $^{207}Pb/^{204}Pb$ (15.46-15.50) and $^{208}Pb/^{204}Pb$ (37.95-38.06). Values from suite C3 pumices are tightly clustered and comparable those from members A and B ($^{206}Pb/^{204}Pb$ = 16.99-17.00, $^{207}Pb/^{204}Pb$ = 15.35-15.49 and $^{208}Pb/^{204}Pb$ = 38.03-38.06). Other samples from suites C1 and C2 in member C show distinctly different Pb isotopic signatures, with more radiogenic $^{206}Pb/^{204}Pb$ (17.89-18.16) and $^{207}Pb/^{204}Pb$ (15.69-15.78), which are positively correlated and fall along a linear extension of the A and B trend. However, they have less radiogenic $^{208}Pb/^{204}Pb$ (37.87-37.92), which is negatively correlated with $^{206}Pb/^{204}Pb$ and $^{207}Pb/^{204}Pb$ (Fig. 15).

Groundmass glass chemistry

Groundmass glass compositions (by EPMA and LA-ICP-MS on separated shards from crushed pumices) in members A and B are dominantly high-silica rhyolite (75-78 wt % SiO_2: Supplementary Data Electronic Appendix 4) with extensions to low-silica rhyolitic compositions observed in glass from types J3 (mostly 72-74 wt % SiO_2) and J4 clasts (71-77 wt % SiO_2). Glass from members A and B is alkali-rich ($Na_2O + K_2O$ = 7.6-9.4 wt %), with glass from type J2 samples clustered to higher alkalis (8.5-9.3 wt %) and lower CaO (0.24-0.49 wt %) concentrations for a given value of SiO_2 (Supplementary Data Figs. S10-S12). Low-CaO and elevated alkali contents in type J2 sample groundmass glass, which is darkened by Fe-Ti oxide crystallisation, indicates that some alkali mobility may have occurred, and these compositions are set aside. Types J3 and J4 samples extend to higher

CaO values (up to 2.2 and 1.5 wt %, respectively). The negative correlations between Al_2O_3, alkalis and CaO *versus* SiO_2 are consistent with a dominant role for feldspar crystallisation on the glass compositions (Supplementary Data Figs S10-S12).

Groundmass glasses from members A and B form an overall continuum in incompatible trace elements (e.g. 3.7-10.6 ppm U, 100-260 ppm Rb; Supplementary Data Electronic Appendix 4). In detail, however, glasses from suite A1 samples are clustered in composition for some compatible elements (110-730 ppm Ba, 80-140 ppm La, Ba/Rb = 0.49-4.2, Sr/Rb = 0.01-0.1 excluding one outlier; Figs 16, 17). Glasses from suite A2 samples are distinctly Ba-richer (1310-3360 ppm Ba, 90-110 ppm La, Ba/Rb = 9.2-24, Sr/Rb = 0.22-0.47) and from suite A3 samples Ba-poorer (31-62 ppm Ba, 49-81 ppm La, Ba/Rb = 1.3-0.24, Sr/Rb = 0.01-0.04, excluding two outliers). The clustered nature of the glass compositions parallels that observed in the initial fall deposits and basal ignimbrite (Myers *et al*., 2016; Swallow *et al*., 2018a), with close similarities in the cluster averages between the fall deposit/basal ignimbrite and groundmass glasses (Figs. 16, 17). Groundmass glass fragments derived by crushing from single clasts in member A are compositionally homogeneous within themselves, with only limited compositional variation within single pumices, particularly when compared to the overall range observed (Supplementary Data Fig. S13). Glass compositions from type J1 clasts in member B focus at the less-evolved end (e.g. 120-1680 ppm Ba, 62-140 ppm La) of the compositional spectrum shown by suite A1 glass data. Rhyolitic glass from scoria-bearing (type J4) clasts covers the entire glass compositional range of J1 samples in member B (≥180 ppm Ba), but also defines an antithetic trend, extending from the highest-Ba J1 pumice glass to higher Ba and lower La compositions (3100 ppm Ba, 83 ppm La; Fig. 16), similar to the type J3 clast glass in member A.

Groundmass glasses, where available from member C clasts (pumice types J7 and J8), are all high-silica rhyolite (76-78 wt % SiO_2). No glass could be recovered from suite C1 clasts. There are no groundmass glasses found in any member C clasts that plot along the trend defined by suites A1 or B1 clasts. Glasses from type J7 clasts are highly evolved, with low Ba (18-120 ppm), La (45-64 ppm) and Ba/Rb and Sr/Rb ratios (0.07-0.54 and 0.01-0.04, respectively; Figs 16, 17), i.e., similar values to glasses from suite A3 samples. Glasses from type J8 clasts are compositionally unique, however, with elevated, but clustered, Ba compositions (360-2390 ppm) for a given, but relatively uniform, La content (63-89 ppm) when compared to glasses from pumices in members A and B. The type J8 glasses are also poorer in U (5.1-8.5 ppm) for a given value of Rb (140-180 ppm) and plot below the Ba/Rb-Sr/Rb curve (Ba/Rb = 2.2-16.0 and Sr/Rb = 0.1-1.0) relative to the trend in members A and B

(Fig. 17). They are also characteristically depleted in Nb (28-36 ppm) and Th (17-30 ppm) relative to glasses from clasts in members A and B (Electronic Appendix 4).

MINERAL CHEMISTRY

Feldspar

Potassium-rich feldspars in members A and B are dominantly sanidine, but with minor anorthoclase, and commonly contain a significant celsian (Cn: Ba-feldspar) component ($An_{1-10}Ab_{36-65}Or_{29-59}Cn_{0-11}$; Figs 18, 19; Supplementary Data Electronic Appendix 5). Rim compositions have a more restricted range, with lower An and Cn values ($An_{1-7}Ab_{40-65}Or_{29-58}Cn_{0-6}$) with overgrowths (e.g. anti-rapakivi feldspars) being more Cn rich (1.7-7.5 mol%; Fig. 19). Sanidine crystals from suite A3 clasts lie at the potassic end of the range ($An_{1-2}Ab_{39-44}Or_{53-59}Cn_{0-1}$). Potassium-rich feldspars in member C form a similar trend to members A and B, but isolated crystals extend to higher Or values ($An_{0-10}Ab_{21-59}Or_{29-78}Cn_{0-7}$). Sanidine crystals from suite C3 clasts are typically more potassic and have lower Cn contents ($An_{1-4}Ab_{39-46}Or_{49-59}Cn_{0-2}$) than those from suite C2 clasts ($An_{1-9}Ab_{40-59}Or_{29-56}Cn_{0-7}$; Fig. 19).

Plagioclase feldspars from members A and B are mostly andesine to oligoclase, but form a continuum to anorthoclase ($An_{11-46}Ab_{50-76}Or_{3-28}Cn_{0-4}$; Fig. 18). The more potassic compositions are dominated by interior domains and 'plutonic-textured' crystals (see below). Grains from suite A3 samples plot at the albite-richer end of the trend ($An_{15-20}Ab_{71-76}Or_{8-11}Cn_{0}$). Plagioclase compositions in member C are more clustered than in members A and B and are grouped by suite: (a) a trend extending to higher An contents ($An_{33-52}Ab_{46-61}Or_{2-5}Cn_{0}$) dominantly defined by grains in suite C1; (b) an oligoclase-centred cluster ($An_{14-30}Ab_{62-77}Or_{4-15}Cn_{0-2}$) with grains from suite C3 ($An_{14-22}Ab_{68-75}Or_{8-12}Cn_{0-1}$) at the albite-richer end of the cluster; and (c) an anorthoclase cluster ($An_{10-15}Ab_{60-66}Or_{17-27}Cn_{1-4}$) dominated by grains from suite C2.

Texturally, 80% of the sanidines from suite A3 clasts are homogenous (Supplementary Data Electronic Appendix 5) whereas sanidines in clasts from suites A1 and B1 are more commonly zoned in backscattered electron images (57% and 70% of crystals, respectively; Fig. 20) but with no coherent sense of zoning. Suite A2 samples exhibit equal numbers of homogeneous and zoned (to lower Or) sanidines, but also contain crystals with high-Ba overgrowths, represented as either anti-rapakivi textures or sanidine rims (7% of feldspar crystals). Anti-rapakivi textures are also sparsely present in member B samples (2% of feldspar crystals; Fig. 20). Sanidines from member C show approximately equal proportions

of zoned and homogenous crystals irrespective of the compositional suite. In contrast to the sanidine record, plagioclase is dominantly homogeneous in all compositional suites from the entire HRT (>80 % of crystals in each suite).

Feldspar crystals cemented or coated in a carbonate matrix are present in sparse abundance (3% of all feldspar crystals) in suite A1 samples. 'Plutonic-textured' feldspars, characterised by feldspar intergrowths and dissolution textures (Parsons, 1978; Fig. 20), are present in all suites. They typically comprise <10% of feldspar crystals, with the exception of scoria-bearing, type J4 pumices in member B (17%).

Pyroxene

Pyroxene compositions in members A and B show bimodality in their interior compositions (Fig. 21). Low-Ca pyroxenes (hereafter pigeonite for simplicity, despite extending to lower Ca than the pigeonite field of Poldervaart & Hess, 1951) are present as cores, inclusions or intermediate zones ($En_{13-72}Fs_{25-78}Wo_{0-12}$) in ~9% of crystals. Alternatively, interior domains of clinopyroxene composition (i.e. augite) occur, spanning a wide range ($En_{4-40}Fs_{22-55}Wo_{34-43}$). In contrast, rims in members A and B are Fe-rich augite and are tightly clustered ($En_{6-17}Fs_{44-53}Wo_{38-44}$) with no discernible difference between clast compositional types or eruptive suites.

Member C pyroxenes present variable compositions, depending on the clast type and/or locality. Pyroxenes from suite C1 clasts show a continuum from Ca-poor to Ca-rich ($En_{3-45}Fs_{43-68}Wo_{0-43}$) but with only crystals from sample YP648 plotting in the sub-calcic augite field (Fig. 21). In contrast, pyroxenes from samples in suites C2 and C3 show a more clustered compositional nature. Although there is a subset of suite C2 grains with pigeonite compositions ($En_{11-37}Fs_{62-79}Wo_{1-11}$), these are only found in interior domains (similarly to pyroxenes in samples from members A and B) and in crystals apparently in disequilibrium (e.g., containing sieve textures). Augite compositions from suite C2 form a similar compositional trend to those of members A and B, but extend to more Fe-rich compositions ($En_{3-28}Fs_{32-56}Wo_{38-43}$) with rim compositions tightly clustered at the Fe-rich end ($En_{4-41}Fs_{53-55}Wo_{41-43}$). Suite C3 grains are homogenous, tightly clustered and plot within the A and B augite field ($En_{7-11}Fs_{48-52}Wo_{39-44}$) with the exception of one pigeonite grain (out of 15 analysed). Pyroxene crystals in the HRT are dominantly (normally) zoned (>60 % of crystals in all suites: Fig. 21; Supplementary Data Electronic Appendix 5).

Olivine

All olivines are fayalitic but compositional diversity is present within the different juvenile clast types. Olivine crystals are unzoned and homogenous in all samples studied. However, they commonly show oxidation alteration to iron oxides and hydroxides on rims and along fractures (Fig. 22), as noted also in other eruptive units from the YPVF (Troch *et al*., 2017). Olivines in members A and B are similar in composition and encompass the entire range in the HRT (Fa_{86-100}; Supplementary Data Electronic Appendix 3), but some compositional clustering is present. There is bimodality in CaO contents: one cluster has CaO contents ≥0.32 wt %, dominated by crystals from J4-type (mingled) pumices, while the other has modal concentrations of 0.18-0.30 wt % CaO in crystals from J1-type pumices (Supplementary Data Fig. S14). There is a similar bimodality in MgO: a lower MgO cluster (1.4-1.8 wt %) is defined by crystals from suite A1 samples, whereas olivines from other clast types define a cluster with a peak at 1.9-3.0 wt % MgO (Supplementary Data Fig. S15). Member C fayalite compositions (Fa_{94-100}) vary less than in members A and B but show a greater range in CaO (0-0.41 wt %; Supplementary Data Fig. S14). Olivines from suites C1 and C2 are predominantly elevated in CaO (0.24-0.41 wt %) with a minor group with ≤0.04 wt % CaO. They also extend to lower MgO values (0.44-1.48 wt %, with a subset at <0.03 wt %). There are distinct differences, however, between olivines from suites C1 and C2 when compared to those from suite C3. Olivines from suite C3 are more similar to those from members A and B, and compositionally overlap with suite A3 olivines (1.43-2.34 wt % MgO; Supplementary Data Fig. S15).

Accessory phases

As documented by Macdonald & Belkin (2002), chevkinite is present in the HRT (Fig. 22; Supplementary Data Electronic Appendix 3). Individual crystals (0.5-1 mm) are most common in suite A3 samples (9% of picked ferromagnesian minerals) but also occur in J1 clasts from suite B1 (<1 %) and suite C3 (3%). Accessory apatite and zircon are also present. Fe-Ti oxide pairs are also present, but almost always one or both of these phases show exsolution textures (indicative of sub-solidus oxidation) and as such were not analysed.

ESTIMATES OF INTENSIVE VARIABLES

Temperature

Because of the scarcity of non-exsolved Fe-Ti oxide pairs, zircon saturation calibrations (Supplementary Data Electronic Appendix 4) for groundmass glasses were used to estimate pre-eruptive melt temperatures for samples where zircon was inferred to be stable through petrography or Zr abundances decreasing with SiO_2 (i.e. all except type J5, suite C1 samples). We used the Watson & Harrison (1983) calibration due to its consistency with other temperature estimates for the HRT (Myers *et al*., 2016; Swallow *et al*., 2018a). Types J1 and J2 clasts from members A and B yield a wide temperature range (790-890 °C; Supplementary Data Fig. S16; Electronic Appendix 4). Suite A3 pumices cluster at the cooler end of the range (790-840 °C), while suite A2 pumices yield higher temperatures (890-960 °C). Similarly, rhyolitic glasses from scoria-bearing J4 clasts in member B yield a wide temperature range (820-950 °C). Type J7 clasts (suite C3) yield comparably lower estimates to their suite A3 counterparts (800-840 °C). In contrast, the diverse glass compositions from type J8 clasts (suite C2) yield a wide range of temperature estimates (820-900 °C) and show a bimodal distribution (Supplementary Data Fig. S16). If single-clast compositions are used for devitrified member C clasts (type J9; also suite 2) from the Red Mountains (810 °C) and Huckleberry Mountain (870-900 °C), their model temperatures are comparable to those of type-J8 samples.

Two-feldspar thermometry (Elkins & Grove, 1990) was also applied to plagioclase inclusions in sanidine and vice versa (Supplementary Data Electronic Appendix 5). All feldspar compositions were normalised to Cn-free (following Swallow *et al*., 2018a). Types J1 and J2 clasts from members A and B yield a large range in model temperatures (770-950 °C) with medians of 840 °C and 860 °C, respectively, slightly hotter than the respective median zircon model temperatures for each group (830 and 840 °C; Supplementary Data Fig. S16). Type J1 clasts in suite A2 pumices yield hotter estimates (840-920 °C) that overlap with the cooler end of the zircon saturation range for the same suite. Type J1 clasts in suite A3 pumices are offset to cooler temperatures (750-820 °C; median 790 °C), ~20 °C cooler than the zircon median (810 °C). Wide temperature ranges, comparable to those derived from zircon saturation estimates, are returned from member B samples; type J1 clasts yield a comparable range to member A (770-940 °C), whereas scoria-bearing type J4 clasts extend to 760-990 °C. In member C, type J7 clasts (suite C3) yield a wider range (770-860 °C) than their suite A3 comparators, but a similar median (790 °C). Type J8 samples (suite C2) show

the largest temperature range of all compositional groups (720-920 °C) encompassing the range in compositionally equivalent devitrified clasts from Huckleberry Mountain (780-900 °C). Sparse suitable feldspars from type J5 (suite C1) clasts in member C yield a wide range of temperatures, extending to implausibly cooler temperatures (650-810 °C).

Utilising the presence of pigeonite compositions as cores or inclusions in augite crystals, two-pyroxene thermometry was also undertaken (Supplementary Data Electronic Appendix 5). Out of 58 potential pairings, however, only four passed the Putirka (2008) Fe-Mg exchange equilibrium test of $K_D = 1.09 \pm 0.14$. Using the calibration of Brey & Köhler (1990), temperature estimates were obtained in crystals from clasts of types J1 (870 °C), J4 (1010 °C), J8 (1100 °C) and J5 (820 °C). Temperature estimates using the calibration of Putirka (2008) for low Mg# clinopyroxenes yielded implausible results (temperatures up to 1810 °C).

Oxidation state and H_2O content

The presence of fayalite, magnetite and quartz in all compositional suites constrains the oxygen fugacity for the HRT magmas to be close to the QFM buffer, consistent with other studies of YSRP rhyolites (Christiansen & McCurry, 2008; Almeev *et al*., 2012; Befus & Gardner, 2016). The plagioclase-melt hygrometer of Waters & Lange (2015) was used to estimate pre-eruptive melt H_2O contents (Supplementary Data Electronic Appendix 5), using zircon saturation thermometry estimates due to the wide range of two-feldspar model temperatures. Other inputs are measured rim compositions, mean major element groundmass glass compositions (or single clast compositions for devitrified member C samples), and a pressure of 200 MPa (Myers *et al*., 2016, their electronic appendix 1). We use mean temperature estimates to calculate mean H_2O contents. Samples from suite A1 yield 2.7-3.6 wt % H_2O, a similar range to that from type J1 clasts in member B (suite B1: 2.1-3.6 wt % H_2O). In comparison, maximum contents in suite A3 pumices are higher (3.8-4.0 wt % H_2O), whereas contents in samples from suite A2 and type J4 clasts in suite B1 are lower (1.2-1.3 and 1.7-3.0 wt % H_2O, respectively). Suite C3 pumices yield similar H_2O contents (3.7-4.0 wt %) to their suite A3 counterparts, whereas suite C2 samples yield H_2O contents of 2.0-3.5 wt %, with one outlier at 4.1 wt %. For suite C1 samples the hygrometer yields unlikely maximum estimates of 8.5 wt % H_2O, but this reflects the anomalously low model temperatures (which could only be done by two-feldspar thermometry) in these samples. Comparison of the hygrometer between melt inclusion data from the early HRT fall deposits

(Myers *et al*., 2016; 3.3-4.9 wt % H_2O) and the associated plagioclase and groundmass glasses (4.0-4.5 wt % H_2O; E. J. Swallow, unpublished data cited in Myers *et al*., 2016) suggests that the hygrometer is accurate. However, consideration of likely uncertainties in model temperatures would suggest that variations of ± 1.2 wt % H_2O could apply to individual determinations. The ranges listed above should thus be taken as indicative.

Although pyroxenes are limited in constraining temperatures, the presence of pigeonite only as cores or inclusions is significant. In contrast to the HRT, the 'hot and dry' (Branney *et al*., 2008) Snake River Plain ignimbrites commonly have co-existing population(s) of phenocrystic pigeonite and augite within any one eruption (Cathey & Nash, 2004; Ellis & Wolff, 2012). Experimental work on these materials (Almeev *et al*., 2012; Bolte *et al*., 2015) provides constraints, as follows.

- At water contents of <0.5 wt %, pigeonite is a near-liquidus phase (~1000 °C) but augite replaces pigeonite as the earliest-forming pyroxene at higher water contents (Almeev *et al*., 2012).
- Augite was not observed in experiments at H_2O > 1.3 wt % (Almeev *et al*., 2012).
- Ca-rich augite compositions (i.e. >40 mol% Wo), as seen predominantly in rim compositions in the HRT, are only observed in experiments with moderate-high melt H_2O contents (>1 wt % at 925 °C to >3 wt % at 825 °C; Almeev *et al*., 2012).
- Augite is generally stable at lower temperatures than pigeonite and the range in conditions where both can co-exist is narrow (Bolte *et al*., 2015).

These constraints suggest that the HRT magmatic systems were initially H_2O-poor, and that pigeonite, possibly with co-existing augite, was stable. Increasing H_2O contents and decreasing temperatures during evolution of the various magma systems preferentially favoured augite stability and a continuing increase in H_2O contents led to an increase in the augite Wo content, as displayed in augite rim compositions (Fig. 21).

Pressure

Pre-eruptive storage pressures were estimated from groundmass glass major element compositions using the Determining Rhyolite Pressures (DERP) geobarometer of Wilke *et al*. (2017; Supplementary Data Electronic Appendix 4), which requires glasses to have equilibrated with quartz and at least one feldspar. Although criticised by Gualda *et al*. (2019) the DERP model remains a valid approach for the HRT glasses as the glasses are mildly

corundum normative and are closer in composition to those used to define the DERP model than those used to define the alternative rhyolite-MELTS model (Wilke *et al*., 2019).

Types J1 and J2 clasts from member A (suite A1) yield a similar distribution and range of model pressures from ~100-450 MPa (Supplementary Data Fig. S17). The lower figure is consistent with the lowest pressures (80 MPa) derived from quartz-hosted melt inclusions in the initial fall deposits (Myers *et al*., 2016). Type J3 clasts (suite A2) yield a tail of greater model pressures (mostly >800 MPa; Supplementary Data Fig. S17), although these are outside the range of model calibration (Wilke *et al*., 2017). Although some samples return impossible negative pressures, type J1 clasts in member B (suite B1) yield a broader distribution of pressures than their counterparts in member A, but have similar mean and median values (320 and 330 MPa, respectively, in member A; 310 and 320 MPa in member B). Scoria-bearing type J4 clasts in member B show a bimodal distribution, with one mode (~330 MPa) similar to J1 clasts, and the other at ~800 MPa (Supplementary Data Fig. S17). In member C, type J8 (suite C2) samples extend to lower model pressures (mean 200 MPa, median 230 MPa) when compared to J7 samples (mean 260 MPa, median 270 MPa), while the latter estimates are closely similar to their member A, suite A3 comparators (mean 270 MPa, median 270 MPa).

However, pressure estimates can only be as precise as the input data. We tested the DERP model using an average major element glass composition from all analyses in this study and absolute 2 s.d. EPMA uncertainties derived from multiple analyses of glass standards (e.g. SiO_2 ± 1.16 wt %; K_2O ± 0.48 wt %). Approximate differences in model pressures of ±50 MPa from SiO_2 and ±100 MPa from K_2O are calculated using these typical analytical uncertainties. In comparison, variations in input H_2O contents of ±2 wt %, around a starting point of the mean glass composition and 4 wt % H_2O, yield pressure differences of approximately ±20 MPa. As a result, we consider that pressure differences of less than ~100 MPa are effectively unresolvable with the analytical uncertainties attained in this study (which are typical of EPMA data). This is important to note as pressures estimated using EPMA data on (hydrated) natural glasses can be a recurring focal point of debate regarding the nature of large magmatic systems (e.g. Gualda & Ghiorso, 2013; Chamberlain *et al*., 2015; Wilke *et al*., 2019).

DISCUSSION

The HRT provides an unparalleled example of compositional diversity within the deposits of a large silicic, caldera-forming eruption that in itself was complex and prolonged (Fig. 2, Supplementary Data Fig. S1). The initial fall deposits represent episodic activity, inferred to have occupied some weeks, with time for reworking and numerous short hiatuses in eruption, matched by evidence from melt inclusion volatile abundances for slow magma ascent (Myers *et al*., 2016; Swallow *et al*., 2018a). Ignimbrite members A and B were separated by weeks to months, and members B and C by years to decades. This chronostratigraphic interpretation provides a framework within which the observed extraordinary compositional diversity can be placed.

Magmatic systems in the HRT

To provide a central focus for discussion, the elemental and isotopic characteristics of the seven silicic suites (A1, A2, A3; B1; C1, C2, C3) are used here to define four magmatic systems that at various stages simultaneously and successively fed the HRT eruption (Fig. 23). The defining chemical and isotopic characteristics of each system are summarised in Table 4 and reviewed below. Note that our geochemical and isotopic data indicate that the HRT magmatic systems were discrete entities (cf. Cooper *et al*., 2012, 2016) and not subtly different components of a heterogeneous single system (cf. Bégué *et al*., 2014).

Magmatic system 1

Magmatic system 1 is inferred to be volumetrically dominant in terms of eruption products, based on the relative abundance of clasts observed and analysed (including the glass compositions in Swallow *et al*., 2018a), and the overall proportion (~90 volume %: Christiansen, 2001) of members A and B in the HRT. Magmatic system 1 hosted the melt-dominant bodies that were evacuated for most of the initial fall deposits (glass clusters FGC/OGC3 and IGC2 to IGC8 of Swallow *et al*., 2018a) and ignimbrite members A and B (suites A1, A2 and B1: Fig. 23). Products of this system show wide ranges in geochemical composition (e.g. 410-4170 ppm Ba) but a moderate isotopic range (e.g. $^{87}Sr/^{86}Sr$ = 0.71009-0.71256: Figs 8, 14). Single clast compositions are enriched in alkalis, Al_2O_3, Zr and Ba, and depleted in FeO, TiO_2, CaO, Sr and Sc relative to the three other systems (Figs 5-12; Supplementary Data Figs S2-S4, S7). Clustered glass compositions are interpreted to reflect multiple melt-dominant bodies which capped the system (Figs 16, 17), some of which were

tapped from the eruption onset (Myers *et al*., 2016) and others which first vented at the onset of member A emplacement (Swallow *et al*., 2018a). In its mineralogical characteristics, sanidines from this system contain >0.4 mol% Cn and pyroxenes are typically Fe-rich clinopyroxene, sometimes with pigeonite cores, and are tightly clustered in composition (Figs 19, 21). No material has been found with the compositional characteristics of suite B1 but with the small crystal sizes present in all juvenile ejecta found in member C, implying that magmatic system 1 was not vented during member C activity, and that it was distinct from magmatic system 2.

Magmatic system 2

Magmatic system 2, minor in volume when compared to system 1, is represented by the low-Ba glass in the initial fall deposits (FGC/OGC1+2, IGC1 of Swallow *et al*., 2018a), and clasts of suites A3 and C3 in ignimbrite members A and C, respectively (Fig. 23). Although suite A3 compositions arguably fall on a continuum with those of suite A1 (Figs 5-7), the contrasting evacuation history relative to magmatic system 1 (i.e., its absence in member B and reappearance in member C: Fig. 23), the distinctive sanidine (<0.35 mol% Cn: Fig. 19) and olivine compositions (Figs S14, S15), and the lack of mixing/mingling with any other compositional suite make it distinct. Although suite A3 samples have comparable isotopic compositions to the materials from magmatic system 1, suite C3 samples are less radiogenic with respect to Sr (Fig. 14) for a given elemental abundance (although no different in Nd or Pb isotopes: Figs 15, Supplementary Data Fig. S9) and the pumices have contrasting textures and smaller crystal sizes. System 2 was vented from the very start of the eruption in the earliest fall deposits (Myers *et al*., 2016), then stopped, and re-started in early member A ignimbrite activity (Swallow *et al*., 2018a). It was not vented during eruption of member B, then was reactivated during the B:C time break to produce new melt-dominant magma that was vented in minor amounts during eruption of member C ignimbrite.

Magmatic system 3

Magmatic system 3 is represented by suite C2 clasts, which are the dominant lineage in member C. It is inferred to be the second largest system represented within the HRT on the basis of the relative abundance of suite C2 clasts within the dominant observed volume of member C ignimbrite. Suite C2 covers a comparable compositional range to the suites in magmatic system 1 (e.g. Ba 450-2840 ppm: Fig. 8), but is offset to higher SiO_2 abundances.

Products of this system exhibit a unique compositional trend with large variations in trace elements occurring over a narrow SiO_2 range (75-78 wt %; e.g. Figs 8, 9, 12). They are depleted in Nb (27-32 ppm) relative to member A and B samples, but have moderate Fe_2O_3 (1.3-3.3 wt %) and TiO_2 (0.12-0.29 wt %) concentrations (Figs 10, S2, S3). Products of this magmatic system have strongly crustal isotopic signatures (e.g. $^{87}Sr/^{86}Sr$ = 0.72590-0.73026: Figs. 13, 14; cf. Doe *et al*., 1982) and in this are closely linked to system 4. Groundmass glass compositions from this system are clustered, again suggesting the presence of multiple melt-dominant bodies (Figs 16, 17; cf. Myers *et al*., 2016; Swallow *et al*., 2018a), although glass compositional trends are offset from those in members A and B. Characteristic crystal compositions include Fe-rich olivines and Cn-rich sanidines (Figs. 19, S14, S15).

Magmatic system 4

Magmatic system 4 is represented by suite C1 samples and is the minor of the two newly-erupted systems contributing to ignimbrite member C, based on the observed minor volumetric abundances of clasts of type 5 in member C ignimbrite. Despite their moderate SiO_2 contents, suite C1 samples return remarkably crustal isotopic compositions (e.g., $^{87}Sr/^{86}Sr$ = 0.72464-0.72486: Figs 13-15). Suite C1 samples are distinctly elevated in CaO, Fe_2O_3, Sc and Sr, and lower in Al_2O_3, Ba and Nb relative to the other magmatic systems (Figs 6-11, S2, S4), comparable in some respects to those compositions of magmatic system 3, but distinct in others (e.g. Sr, Zr: Figs 9, S7). Like other member C material, suite C1 samples have small crystal sizes (<3 mm) and contain pyroxenes along a continuum between the pigeonite and augite fields (Fig. 21).

To add to these complexities, system 1 alone shows evidence from compositional variations and the direct eruption of homogeneous and mingled clasts in members A and B, for extensive interaction with mafic magmas. Although most of these compositions belong to the 'HRT mafics' grouping documented by Swallow *et al*. (2018b), some material with tholeiitic affinities also interacted with and was erupted from magmatic system 1 to be incorporated in upper member B material distributed north of the caldera. Magmatic system 2 shows no indicators of syn-eruptive interaction with mafic compositions, but has compositional and isotopic links to magmatic system 1 and thus an indirect linkage to the HRT mafic magmas. Magmatic system 3 also has some compositional links to the distinctive HRT mafics, but also shows no signs of direct interaction, and is isotopically distinct from both systems 1 and 2. In contrast, system 4 shows compositional trends with respect to SiO_2

that are aligned in several respects to the fields defined by YPVF olivine tholeiite lavas (suite M2: Swallow *et al*., 2018b; e.g., Figs 5, 8, 10, S7), although, again, no evidence for syn-eruptive interaction has been found.

Petrogenesis of HRT silicic melts

Here we consider the processes that influenced the origins of the compositions erupted from the four HRT magmatic systems. Detailed quantitative petrogenetic modelling is not possible at this stage for two reasons. First, the overall range of mafic compositions erupted into member A is very broad, and no clear end-member 'primitive' composition can be identified. The spread of data increases markedly with the scoria erupted into member B, and it is apparent in particular from some elements (Fe_2O_3, P_2O_5, TiO_2, CaO, Ba, Sr, Zr: Figs 7-9, S2-S4, S7) that renewed influxes of mafic magma into member B included other magmas with tholeiitic affinities. A distinctive mafic end-member is thus hard to define. Second, we lack the data on trace element or isotopic compositions in the mineral phases that would serve to accurately define the respective end-members or fractionation pathways. We thus discuss a range of possible processes below to arrive at generalised conclusions about the pathways to generation of the HRT silicic compositions. An overall summary flow chart of the processes discussed is given in Fig. 24 and the time-sequence of erupted materials summarised in Fig. 25.

Magmatic systems 1 and 2

On the basis of their similar major element and isotopic features, we petrogenetically link magmatic systems 1 and 2 here. The HRT (and other YPVF rhyolites) were previously proposed to be generated by partial melting of tholeiitic intrusions (Doe *et al*., 1982; Hildreth *et al*., 1991; Christiansen, 2001; Christiansen & McCurry, 2008). In contrast, our data from magmatic systems 1 and 2 strongly imply a petrogenetic link to the distinctive HRT mafic material (suite M1, rich in alkalis, Ba and Zr: Swallow *et al*., 2018b), erupted with member A. In particular, the Pb isotopic compositions of samples from magmatic systems 1 and 2 and the HRT mafic samples overlap (Fig. 15), suggesting that they share a common root zone. Based on this feature, we explore the petrogenesis of magmatic system 1, focusing first on the least-evolved compositions from suite A1, plus suite A2, before discussing intra-suite variations and relationships between systems 1 and 2.

Clasts from magmatic systems 1 and 2 have more radiogenic $^{87}Sr/^{86}Sr$ ratios than any HRT mafics (Fig. 13), although the differences are minor in comparison to those with suites C1 and C2, and $^{143}Nd/^{144}Nd$ ratios are similar in the rhyolitic and mafic samples (Fig. 13). These data thus preclude a significant petrogenetic role for the highly radiogenic (with respect to Sr) Archean country rocks (e.g. Doe *et al*., 1982; Wooden & Mueller, 1988; Hildreth *et al*., 1991; Frost *et al*., 2006). In detail, however, Sr isotopic compositions form an asymptotic increasing trend when plotted against indices of melt evolution (Fig. 14). This increase, and the offset of the silicic components in members A and B to higher $^{87}Sr/^{86}Sr$ values at similar elemental concentrations relative to the mafic suites (e.g. Ba: Fig. 14), implies some minor incorporation of an evolved, radiogenic (with respect to Sr) component during melt evolution. This component cannot be any of the strongly crustally influenced melts of suites C1 and C2 because corresponding mixing trends in either elemental abundances (e.g. Nb) or other isotopic (e.g. Pb) compositions (Figs. 10, 15) are lacking. Overall, the moderate Sr isotopic diversity within magmatic systems 1 and 2 and slight positive correlation with 1/Sr (particularly relative to magmatic system 3), suggest that the final evolution of magmas in systems 1 and 2 was mostly controlled by fractional crystallisation., but with minor assimilation These inferences are also supported by the relative uniformity of Nd isotopic ratios with degrees of fractionation (Supplementary Data Fig. S9; Wolff *et al*., 2015).

Fractional crystallisation model. Potential analogues to the HRT silicic compositions are the rhyolites of Cedar Butte (eastern Snake River Plain), interpreted to reflect extensive (~80 %, 4.3 kbar) fractional crystallisation of a basaltic trachyandesite comparable to the HRT mafic compositions (McCurry *et al*., 2008; Whitaker *et al*., 2008). In parallel to the HRT rhyolites, McCurry *et al*. (2008) also reported minor increases in radiogenic Sr isotopes, correlated with melt evolution. We therefore consider fractional crystallisation from an HRT mafic parent (or melting of a compositionally related protolith) for generation of the least evolved compositions within magmatic systems 1 and 2. In turn, as magmatic system 2 is of smaller volume, we focus on system 1, specifically suites A1 and A2 (as suite B1 is a combination of these).

Overall, a simple fractional crystallisation model is precluded, however, by the behaviour of highly incompatible elements such as Rb, Nb and U, which show increasing concentrations in member A mafics on either side of the compositional gap, but a uniformity across the gap (e.g. Figs 10, S6). Therefore, when plotted together, these incompatible

elements show a broad continuum between HRT mafics, suite A2 and suite A1 material (Supplementary Data Fig. S18). These relationships are inconsistent with a simple fractional crystallisation model and would require coincidental changes in behaviour of these diverse elements at intermediate compositions. We therefore conclude that extreme fractional crystallisation alone of a HRT mafic parent is implausible as the sole mechanism for generation of the silicic suites.

Partial melting model. Alternatively, the HRT rhyolites could be generated through partial melting of mid-crustal intrusions of HRT mafic lineage type. Two simple, end-member, one-stage partial melting scenarios are considered.

First, partial melting of a source similar in composition to the most-evolved of the member A mafics suite. This scenario is unlikely due to the comparable concentrations of strongly incompatible elements (e.g. Nb, Rb) between the most-evolved HRT mafic composition and suite A2 material (Supplementary Data Figs S6, S18). Generation of melts with such similar incompatible element concentrations to the protolith would require either large degrees of melting (close to 100%) and/or an increase in compatibility of the elements in residual phases. The former is precluded by large increases (SiO_2) and decreases (e.g. Ba, Zr) in other elements between the two compositional suites. Although the bulk compatibility of Rb would be elevated with residual alkali feldspar (suggested by the decrease in Ba), Nb concentration changes would require the presence of a Nb-rich phase, for which evidence is lacking (Swallow *et al*., 2018b).

Second, partial melting of a cumulate derived from magmas similar to the member A mafics suite. From the trends in the mafics suite M1 (Swallow *et al*., 2018b) any hypothetical cumulate source should contain residual apatite (decrease in P_2O_5, LREE), plagioclase (broad decrease in Sr) and pyroxene (decrease in Sc with increasing SiO_2). Partial melting of such a cumulate would therefore generate melts enriched in these elements relative to the melts from which the cumulate formed. However, the HRT silicic compositions are further depleted in P_2O_5, Sr and Sc than any compositions within the mafics suite.

Fractionation-partial melting model. We infer that a multi-stage fractionation-partial melting model (similar to that of Reubi & Blundy, 2008) is required for the silicic melts of systems 1 and 2, involving compositions not sampled by us at the surface. Assuming an igneous protolith (Protolith 1 in Fig. 26) that is in part a cumulate, constraints on this model are as follows:

(1) Generation of a melt composition, continuing the fractionation trend from the HRT member A mafic materials, that is more evolved than any erupted mafic material sampled. This melt would have Nb, Rb and other incompatible element concentrations higher than those of the HRT mafics, suite A2 material and the least-evolved suite A1 material. To match the incompatible element concentrations between this melt and the rhyolites, there has to be further fractional crystallisation of an assemblage from this melt that is incompatible element depleted, with some abstraction of an enriched melt (not known to be erupted, and/or not sampled here).

(2) Subsequent melting of the crystallised protolith would then generate silicic melts with moderately enriched concentrations of incompatible elements, similar to those in suite A2 and least-evolved suite A1 samples. The protolith would need to be sanidine- and zircon-bearing to explain the decreases in Ba and Zr contents across the SiO_2 compositional gap.

(3) Continued decreases of P_2O_5, Sc and Sr throughout the entire sequence imply continuing roles for apatite, pyroxene and plagioclase as fractionating phases and/or as residual phases in any partially melted protolith. A role for pyroxene in the cumulate residuum is consistent with the depression of MREE in the silicic samples (Fig. 12), as seen elsewhere (Olin & Wolff, 2010). However, although P_2O_5 abundances decrease throughout the sequence, LREE concentrations become decoupled and plateau across the compositional gap before increasing between suites A2 and A1 (Supplementary Data Fig. S19). This decoupling could be related to the very low P_2O_5 contents in suites A1 and A2 (Fig. 7).

We therefore propose a two-stage evolutionary model for the least-evolved suite A1 compositions (Figs 24, 26). Mafic magmatism associated with the Yellowstone plume injected HRT mafic compositions as intrusions into the lower to mid crust. Melt losses from these cooling and crystallising intrusions (to form other, unsampled, intrusive or extrusive rocks) depleted the magmas in Nb, Rb and U and the remaining magma solidified to broadly trachydacitic (~65 wt % SiO_2), sanidine-, plagioclase-, pyroxene-, apatite- and zircon-bearing intrusions. Subsequent partial melting of these intrusions then generated a Ba- and Zr-poorer low-silica rhyolite melt.

Relationships between the A2 and A1 suites. Relationships between suite A2 and the least-evolved suite A1 compositions are constrained by: (a) the compositional gap and offset in single clast and glass compositions between the two suites (Figs 8, 16, 17); and (b) the similar, but slightly less crustally influenced isotopic signatures and absence of an Eu

anomaly in suite A2 samples (Figs 12-14). Three possible origins for the suite A2 magmas then arise:

(1) thorough mixing between mafic material and the least-evolved suite A1 magmas (e.g., Streck & Grunder, 1999). This origin is unlikely because suite A2 samples show no physical evidence of mingling and their compositions are offset from a tie-line between the least-evolved high-silica rhyolite and the HRT mafics (e.g. P_2O_5, Ba: Figs 7, 8).

(2) as the low-silica rhyolite feedstock material for the main high-silica rhyolite body in the HRT (e.g. Allan *et al*., 2017), consistent with the coherency of suites A1 and A2 compositions, particularly for compatible elements (e.g. Ba, Zr: Figs. 8, S7). However, crystal textures are variable within the suite A2 material. Sanidine crystals occasionally contain Ba-rich overgrowths and the compositions of rims are typically less-evolved than the cores (Figs 18, 19), inconsistent with growth as phenocrysts in an evolving melt-dominant magma body. Furthermore, the zircon model temperature estimates are offset to higher temperatures than two-feldspar model temperatures in suite A2 samples (Supplementary Data Fig. S16), in contrast to the alignment between model estimates in other juvenile components that are inferred to be controlled by fractional crystallisation. As such, any interpretation of the suite A2 magma type as a direct precursor to the suite A1 rhyolites is not favoured.

(3) as partial melts of the cumulate, or mush, related to the evolution of the A1 suite. The HRT suite A2 compositions extend up to, but not across, the trachyte-rhyolite boundary (Fig. 5). Evolution of the A1 suite was driven by a feldspar-rich crystallisation assemblage (predominantly sanidine), as indicated by the continued increase in SiO_2 throughout the sequence and the earlier onset of sanidine crystallisation relative to quartz at all H_2O contents in experimental studies on similar materials (Almeev *et al*., 2012). Any resulting mush will thus be sanidine-rich (i.e. syenitic), and less-evolved than both the initial magma composition and any residual melt. Re-melting of this crystal-rich residuum would therefore yield trachytic magmas (Wolff, 2017) but would require an influx of heat and/or volatiles, generally attributed to mafic magma (Deering *et al*., 2011; Bachmann *et al*., 2014; Wolff *et al*., 2015; Wolff, 2017), which is demonstrably present in both members A and B (Christiansen, 2001; Swallow *et al*., 2018b). Such a mafic influx would be consistent with the less-evolved, Ba-richer rims seen on suite A2 sanidines, and higher zircon saturation model temperatures.

Therefore, we propose that magma with a composition intermediate between the suite A2 and least-evolved suite A1 materials, i.e. in the compositional gap, was formed through partial melting of an intermediate protolith (protolith 1: Fig. 26) and began to evolve through

the crystallisation of a feldspar-dominant assemblage (with accessory ferromagnesian minerals, apatite and zircon). The resultant melts, parental to suite A1, became enriched in LREE, Nb, and Rb, and depleted in Ba, Zr and Sr. The onset of chevkinite crystallisation began to lower LREE concentrations in the subsequent melts (e.g. McCurry *et al*., 2008). Variable degrees of crystallisation led to a heterogeneous feldspar-rich mush (protolith 2) from which were extracted multiple melt-dominant bodies that experienced further evolution. An increase in temperature due to an influx of mafic magma into the lower parts of the mush zone then led to partial melting of protolith 2 to yield the LREE-depleted suite A2 magma. This petrogenetic model differs from that proposed for Cedar Butte rhyolites (McCurry *et al*., 2008) due to the contrasting LREE-enriched low-silica rhyolite suite A1 samples relative to LREE-depleted suite A2 material in the HRT.

Variations within suites A1 and A3. Glass compositions in the initial fall deposits and basal member A (Swallow *et al*., 2018a) cover the same compositional ranges as glasses in all analysed suites' A1 and A3 pumices, implying that the first-erupted ignimbrite tapped all the range in suite A1 and A3 melts. The overall trend can be modelled by ~60 % crystallisation from the least- to most-evolved compositions. Isotopic data, showing increasing $^{87}Sr/^{86}Sr$ with degrees of evolution (Fig. 14), indicate some assimilation. However, although single clast elemental and isotopic data show a simple and coherent trend, glass data are clustered and show two evolutionary trends, one between clusters and another, contrastingly inclined series of intra-cluster trends (Figs. 16, 17). For these relationships to be controlled by assimilation alone, two assimilants affecting all the distinct melt-dominant bodies would thus need to be present. This is considered implausible: highly enriched assimilants would skew the isotopic data (Doe *et al*., 1982), and while less enriched silicic rocks occur in the region (e.g. Meen & Eggler, 1989), these are not plausible contaminants because the amounts required to cause the isotopic variations are not matched by major element variations. Compositional variations in suite A1 could also reflect mixing between a highly-evolved magma (i.e. suite A3) and a less-evolved end-member that realistically would be suite A2 or mafic magmas. Single clast and glass LREE (e.g. La) compositional trends preclude both scenarios, however, with the suite A1 compositions trending away from both possible end-members (Figs 16, S8).

Overall, the variations within the samples from suites A1 and A3 are inferred to be predominantly driven by fractional crystallisation. This inference is supported by the curved trend between Rb or Rb/Sr and SiO_2 in type J1 clasts in member A, in contrast to the

scattered but linear trend shown by member B type J4 mingled pumices (Supplementary Data Figs S6, S20). Elemental and isotopic diversities within suites A1 and A3 reflect a mildly heterogeneous mush source, with variations in concurrent, dominant sanidine-controlled fractional crystallisation and minor assimilation, generating the inter-cluster trends. Extraction and ascent of magmas from this source initiated a more plagioclase-dominant crystallisation assemblage, plausibly through changing pressure, generating shallower-sourced trends within each suite (Swallow *et al*., 2018a).

It could be considered that the compositions seen in suite A3 samples (magmatic system 2) represent further crystallisation of the same parental melts as for system 1. However, the distinctive nature of crystalline materials from system 2 (e.g. sanidine core and rim compositions: Figs 18, 19), the absence of suite A3 compositions from member B, and their independent rejuvenation and eruption as suite C3 in member C (see discussion below) indicate that magmatic system 2 was physically separated from system 1 at the time of the eruption. System 2 was also separated from the focus of mafic inputs, due to the absence of any evidence for mixing or mingling between suite A3 pumices and mafic compositions. A physical separation of magmatic system 2 would also explain the offset to cooler temperatures (by ~30 °C: Supplementary Data Electronic Appendix 4) and the compositional gap between suite A3 and the evolved end of the A1 suite in some trace elements (Figs 8, S16).

Magmatic systems 3 and 4

Whilst a highly enriched (crustal) component is implicated in the generation of magmatic systems 3 and 4, what is striking is the isotopic uniformity, but chemical dichotomy, between these systems (Figs 6, 9, 13, 14). Variations in Sr isotopic ratios, coupled with relatively uniform Nd and Pb isotopic ratios, have previously been related to lower Sr concentrations in YPVF rhyolitic melts and therefore greater susceptibility to isotopic modification by assimilation (Hildreth *et al*., 1991; Wolff *et al*., 2015). However, the compositional suites representing the two, member C systems have contrasting Sr concentrations (C1 = 230-320 ppm; C2 = 17-180 ppm) and therefore require separate consideration. Both systems, however, have similar but more radiogenic Sr and Pb and less radiogenic Nd compositions (Figs 13, 15) and positive trends between $^{87}Sr/^{86}Sr$ and Rb/Sr and 1/Sr (Fig. 14), collectively indicative of crustal contamination. Although $^{206}Pb/^{204}Pb$ and $^{207}Pb/^{204}Pb$ ratios are more radiogenic than those from magmatic systems 1 and 2, $^{208}Pb/^{204}Pb$ ratios are less radiogenic and

negatively correlated with other Pb isotope ratios (Fig. 15). This contrast points to a crustal component with low initial Th/U being involved in the generation of both member C systems. This component, however, is inferred to be Archean, due to the $^{206}Pb/^{204}Pb$ *versus* $^{207}Pb/^{204}Pb$ slope defined by HRT silicic samples yielding a pseudo-isochron of 3.06 Ga (Supplementary Data Fig. S21), similar to the 2.6-3.0 Ga pseudo-isochrons from the mafic suites analysed in Swallow *et al*. (2018b). Consequently, the assimilant requires Pb isotopic ratios of $^{206}Pb/^{204}Pb \geq 17.9$, $^{207}Pb/^{204}Pb \geq 15.7$ and $^{208}Pb/^{204}Pb \leq 37.9$. Published geochemical data for crustal materials from the Wyoming craton (e.g. Wooden & Mueller, 1988; Hildreth *et al*., 1991; Frost *et al*., 2006) show wide ranges and suggest that a plausible Archean assimilant with crust-like isotopic characteristics, low initial Th/U and with variable elemental chemistry could be found, but no suitable end-member composition has yet been reported.

Magmatic system 3. Compositions from this system span a wide range (e.g. 410-2280 ppm Ba: Fig. 8) and form the distinctive suite C2 trend. Correlations between increasing $^{87}Sr/^{86}Sr$ values and degrees of evolution in the suite (e.g., increasing Rb/Sr, decreasing Ba: Fig. 14) indicate that assimilation was also important in generating the intra-suite variation. However, the curved Rb and Rb/Sr trends in Figs S6 and S20 suggests that fractional crystallisation was the dominant process for controlling intra-suite trend variation (as in magmatic systems 1 and 2). Overall decreasing Sr, Ba, Zr and Sc abundances within the whole suite attest to feldspar, zircon and pyroxene fractionation within the system (Figs 8, 9, 11, S7), consistent with the increasingly negative Eu anomalies with evolution in the type J8 pumice samples (Fig. 12). Clustered glass and single clast compositions from type J8 pumices that almost cover the entire range in suite C2 (410-2160 ppm Ba) indicate that system 3 (like systems 1 and 2) included multiple independent melt-dominant bodies (Figs 16, 17). The kinked trend in the glass Sr/Rb *versus* Ba/Rb ratios (Fig. 17) is inferred to reflect variations in the crystallising assemblage, with initial plagioclase-dominant followed by sanidine-dominant fractionation, as reflected qualitatively through percentages of picked crystals (Supplementary Data Electronic Appendix 2). Similarly, the intra-cluster trends also indicate continued compositional evolution following formation of the individual melt-dominant bodies.

The parental melt for magmatic system 3 is notably elevated in Ba, Zr and Sr, and depleted in Nb and Rb relative to that for magmatic systems 1 and 2. From the isotopic systematics, we consider partial melting/assimilation of country rocks as a main petrogenetic mechanism. The low Nb and Rb concentrations of suite C2 materials require the influence of

at least one residuum component, comprising a feldspar and zircon rich assemblage. The high Ba and Zr contents of suite C2 samples further implies that any mafic component is related to the HRT mafics rather than olivine tholeiite compositions. The interaction could be direct (i.e. mixing of HRT mafic melts and partial melts of a silicic cumulate) or indirect (i.e. mixing of partial melts from cumulates of both HRT mafics and a highly silicic assimilant). The Pb isotopic compositions of suite C2 samples also align with the fields of HRT mafics and members A and B. However, any melt compositions associated with the HRT mafic materials, either as magmas or partial melts of derivative cumulates, would realistically have ≤70 wt % SiO_2, i.e. much less evolved than the ~75 wt % SiO_2 of the least-evolved suite C2 compositions. Simple binary mixing to generate the least-evolved high SiO_2 trend magma would therefore require a highly silicic end-member that would also need to be enriched in Sr (~250-350 ppm) and depleted in Na_2O+K_2O (~6-7 wt %), Ba (~1500-2500 ppm), Zr (~250-500 ppm) and Nb (~15-25 ppm) relative to the more primitive end-member. Given that documented shallow crustal rocks in the region extend to measured $^{87}Sr/^{86}Sr = 0.89$ (Frost *et al*., 2006), a ~0.2 increase in $^{87}Sr/^{86}Sr$ isotopic values between the HRT mafics and magmatic system 3 is feasible with this model. Although it is challenging to constrain mixing models with limited constraints on the end-members, this is a logical scenario for the generation of the least-evolved compositions of magmatic system 3. The presence of intergrown feldspars and disequilibrium textures (e.g. sieve textures) in feldspars in suite C2 samples also provides evidence for partial melting of a feldspathic cumulate (Fig. 20).

Magmatic system 4. In sharp contrast to the other HRT silicic compositions, Suite C1 products of magmatic system 4, for many trace elements (e.g. Ba, Zr, La: Figs 8, S7, S8), are aligned towards the field of YPVF olivine tholeiites (Swallow *et al*., 2018b) and the newly analysed member B scoria samples from north of the caldera. However, suite C1 diverges from all mafic end-members in other elements, including Al_2O_3, alkalis (both lower than in mafic end members), Fe_2O_3, Sc and Sr (all higher), suggesting a broad relationship to olivine tholeiites, but not simple mixing between a tholeiitic melt and a high-silica component (Figs 5-11, S2, S7). The high Fe_2O_3 and Sc and low Al_2O_3 contents are indicative of a dominant role for clinopyroxene in genesis of this suite. Cryptic clinopyroxene fractionation at >25 km depths has been inferred to occur in YPVF olivine tholeiites (Thompson, 1975; Hildreth *et al*., 1991). Consequently, there would be large quantities of pyroxene-rich cumulates in the mid-lower crust beneath Yellowstone related to the olivine tholeiite mafic root zone and represented in xenoliths of this assemblage found in lavas erupted just west of the HRT

caldera (Leeman *et al*., 1985; Hildreth *et al*., 1991). The moderate Sr, low Al_2O_3 and lack of large positive Eu anomalies in the suite C1 compositions preclude large degrees of plagioclase melting, consistent with an apparent preferential melting of pyroxene over plagioclase in these cumulate assemblages (Leeman *et al*., 1985) and the pyroxene-dominant cumulates predicted at higher pressures (Thompson, 1975; Hildreth *et al*., 1991). The enriched isotopic signatures and elevated Fe, Ti and P in some tholeiitic Yellowstone basalts (e.g. Gerrit and Snake River tholeiites) has also been attributed to interaction with apatite- and pyroxene-rich cumulates (Hildreth *et al*., 1991). We, therefore, propose that melting of such cumulates by further influx of olivine tholeiitic magmas, coupled with assimilation of surrounding enriched Archean crustal materials, generated the suite C1 compositions defining magmatic system 4.

The HRT magmatic complex

The four magmatic systems defined above are collectively referred to what we here, for convenience, term the HRT magmatic complex, that fed the overall eruption sequence. Here we consider the relationships within and between these different systems and their melt-dominant bodies in terms of their intensive characteristics and spatial relationships (Figs 25, 26).

Temperature and pressure/depth characteristics

For magmatic system 1, temperature estimates are broadly similar to those estimated from the basal member A ignimbrite (Swallow *et al*., 2018a; Supplementary Data Fig. S16). As such, we cannot resolve a systematic temperature gradient within the suite A1 samples. Suite A2 yields zircon saturation temperatures hotter than those in suite A1 samples, consistent with this being a thermally discrete magma body. The scoria-bearing pumices in member B contain a mode (~900 °C) intermediate between those of suites A1 and A2, consistent with suite B1 representing a mingling of those two suites. In contrast, magmatic system 2 (both suites A3 and C3) was 20-30 °C cooler (Supplementary Data Fig. S16), consistent with its physical separation from magmatic system 1 and implying that rejuvenation processes in the B-C time gap generated magmas with similar temperatures as well as compositional characteristics. Magmatic system 3 samples yield widely variable temperatures, reflecting wide variations in single clast and glass compositions (Fig. 16), and these are interpreted to reflect the presence of multiple melt-dominant bodies in this system. The temperature of

magmatic system 4 is unknown, although its generally less-evolved compositions imply that it would have been hotter than system 3. The wide temperature ranges across magmatic systems 1-3 are similar to, but offset to higher values than the ~100 °C range suggested by Rivera *et al*. (2014) from Ti-in-zircon thermometry (using an assumed, constant value for α_{TiO2}). Our combined estimates imply that there were significant thermal variations (>170 °C) within the melt-dominant parts of magmatic systems 1 and 3 prior to evacuation, that magmatic system 2 was slightly cooler and less variable, and system 4 hotter.

In contrast to temperatures, pressure estimates are more consistent across and within compositional suites (Supplementary Data Fig. S17), ranging from ~100-450 MPa within all suites (except A2), corresponding to ~4 to 19 km depths. The former is consistent with the lowest pressures estimated from quartz-hosted melt inclusions in the initial fall deposits (Myers *et al*., 2016) and the latter would roughly match the base of the modern geophysically-imaged inferred silicic magma reservoir (Smith *et al*., 2009; Farrell *et al*., 2014; Huang *et al*., 2015). Taken together, available geobarometry estimates for all rhyolite suites, except A2, yield similar pressures, despite their contrasting compositions, implying that the separate magmatic systems and their melt-dominant bodies were laterally, rather than vertically, separated (Figs. 25, 26). This inference is supported by the absence of a simple composition-depth relationship from melt inclusions (Myers *et al*., 2016), as would be expected in a zoned system (Wallace *et al*., 1999; Cashman & Giordano, 2014; Chamberlain *et al*., 2015), and the simultaneous eruption of multiple, compositionally diverse melt-dominant bodies (Myers *et al*., 2016; Swallow *et al*., 2018a). Suite A2 yields inferences of significantly hotter temperatures and higher pressures, consistent with its absence from the early member A ignimbrite. The ~95 x 65 km mapped HRT caldera (Christiansen, 2001: Fig. 1) offers ample space for an areally extensive magmatic complex to have been present in the shallow crust prior to eruption. In addition, the great and sharply defined isotopic contrasts observed between magma systems 1 plus 2 *versus* 3 plus 4 (Figs. 13-15, S9) are implausible in a vertically stacked configuration of magmatic bodies (cf. Cashman *et al*., 2017) where continuity of isotopic variations would be expected through either pre-eruptive magmatic lineages or syn-eruptive mixing processes.

Compositional characteristics and their syn-eruptive evolution

Analysed clasts of types 1 and 2 from member A form a well-defined, coherent high-silica rhyolite trend represented by suites A1 and A3. Groundmass glass compositions from these

clasts indicate, however, that despite relative uniformity in major elements there is significant trace element diversity (cf. Figs 16, 17, S10-S12). The range in trace element compositions and the clustered nature of the data mirror the pattern seen in the fall deposits and basal member A ignimbrite (Myers *et al*., 2016; Swallow *et al*., 2018a). Glass compositional ranges in these early products indicate that the entire range in melt compositions seen in suites A1 and A3 was tapped at the onset of widespread member A deposition. The clustering of the compositional data, inferred to reflect multiple discrete melt-dominant domains, then continued through members A and B. The relative homogeneity of the glass within single pumices, however, implies that these melt-dominant domains remained separate during continued eruption of member A (Fig. 16). This feature then implies that the contrasting domains identified from glasses in the basal member A ignimbrite did not sit atop a unitary, zoned, melt-dominant body that was progressively tapped, but actually reflected almost the entire extent of the subsurface magmatic systems 1 and 2. Pumices spanning the compositional spectrum show comparable crystal abundances (Table 1), suggesting that all the melt-dominant bodies had broadly similar physical properties (i.e. density, viscosity, crystal content) during the eruption (cf. Tramontano *et al*., 2017). For example, magmatic system 2, dominant at the onset of fall deposition and reappearing in the basal ignimbrite, is also represented by some pumices from member A (suite A3: e.g. YP255 [Table 2], YP416: Supplementary Data Electronic Appendix 3), as shown by the similarity in their groundmass glass compositions to clusters FGC/OGC1+2 and their clustered sanidine rim compositions with a low-Cn sanidine rim peak, characteristic of the fall deposit (Figs 16, 19; Swallow *et al*., 2018a). The only compositional suite not represented at the start of member A ignimbrite is suite A2. Although the A2 samples plot on a continuation of the A1 trend with respect to single clast compositions and glass elemental ratios, their groundmass glass concentration data lie off this trend (Figs 16, 17). On the sampling scale used for this study, this compositional separation is consistent with the presence of a discrete, hotter body containing suite A2 magmas within the deeper parts of magmatic system 1.

Significant changes occurred within the HRT magmatic complex between the eruption of the different ignimbrite members. In member B, although suite A1 is largely replicated as suite B1, there are significant differences. First, magmatic system 2 was not tapped, as indicated by the absence of low-Ba pumice and glass, and lack of a significant mode in low-Cn sanidine rims (Figs 16, 19). The absence of evidence for mixing of HRT mafic material with magmatic system 2 also implies that this system was separate from magmatic system 1. Second, the compositional gap between suites A1 and A2 is infilled by the silicic component

of scoria-bearing (type J4) pumices in member B from localities southwest of the caldera (e.g. Fig. 8). This infilling is also observed in the widely varying groundmass glass compositions, with type J4 pumice glass linking the least-evolved glass compositions of suites A1 (and non-mingled pumices in suite B1) to the field of suite A2 clasts (Fig. 16). The antithetic nature of this trend relative to suite A1 indicates that the filling in of the compositional gap is due to mixing between the less-evolved suite A1 melt and a Ba-enriched melt similar to that in the suite A2 magma. The mixing is not directly with HRT mafic scoria, due to the trend of mixed pumices to low LREE contents (Supplementary Data Fig. S8). The bimodality in olivine compositions from J4-type pumices at sites southwest of the caldera also suggests the occurrence of mixing between a melt that contributed to the non-mingled J1-type clasts and a less-evolved component (Fig. S14). All of these mixing processes are inferred to have occurred in magmatic system 1 in the time gap between eruption of members A and B.

The member B scoria (Swallow *et al*., 2018b) indicates a renewed influx and increased degree of mafic mixing in member B relative to member A. Because the rhyolitic components of individual scoria-bearing pumices cover in composition the entire range of suite B1, mixing of the scoria component was widespread within magmatic system 1 and not limited to less-evolved compositions. However, and unexpectedly, scoria clasts that were not included in the samples documented by Swallow *et al*. (2018b) from member B ignimbrite north of the caldera have compositions that trend towards tholeiitic in several elements (particularly P_2O_5, Ba and Zr: Figs 7, 8, S7, and Supplementary Data Electronic Appendix 3). There were thus compositionally diverse mafic influxes into magma system 1 prior to and during eruption of member B. Further work is required to identify whether there is a contrasting 'tholeiitic' imprint on the rhyolitic clast compositions from member B north of the caldera, but material suitable for single clast analysis has not yet been found.

The compositional record from member C is in marked contrast to that from members A and B. Following the years to decades time break between members B and C (Figs. 2, S1), there was venting of magmatic systems 3 and 4, renewed venting of magmatic system 2, yet an absence of any magmatic system 1 material. With system 2, although glass LREE contents are similar between the relevant suites in members A and C, pumices show contrasting abundances of LREE in single clast groundmass glass. Suite A3 pumices have LREE depletions (i.e. glass/clast <1) whereas suite C3 pumices have enriched LREE contents (i.e. glass/clast >1: Supplementary Data Fig. S22). The difference is inferred to reflect chevkinite abundances, being 9% of the picked ferromagnesian minerals in A3 compared to 3% in C3

(Supplementary Data Electronic Appendix 2). As temperature, pressure and H_2O content estimates are comparable between suites A3 and C3, variations in chevkinite abundance may, therefore, be related to time constraints. Glass clusters from the fall deposits (related to magmatic system 2) show bimodal La concentrations (Swallow *et al*., 2018a), suggesting that the degree of LREE depletion is not uniform within this system and is more pronounced in the most evolved melts. This observation implies that chevkinite crystallisation is primarily a late-stage feature, and that the rapid extraction of the melt for suite C3 from magmatic system 2 prior to eruption of member C precluded significant chevkinite fractionation. Furthermore, the less radiogenic (with respect to Sr) nature of suite C3 versus A3 pumices (Figs 13, 14) suggests also that rapid melt extraction hindered the extent of crustal contamination and therefore limited the Sr isotopic values. In suite C3 compared to suite A3 pumices, although sanidine compositions extend to hotter, more Cn-rich values (Fig. 19), these are predominantly in core compositions and crystals therefore record an overall down-temperature history. Furthermore, up-temperature signals are not observed in other crystal phases (e.g. Fig. 22), model temperature estimates are comparable between suites A3 and C3 (Supplementary Data Fig. S16), and system 2 is inferred to lie away from any foci of mafic influx. The rejuvenation of magmatic system 2 during eruption of member C is thus inferred to reflect factors other than mafic influxes.

Magmatic systems 3 and 4, with their unique trace element and crustal isotopic characteristics, are remarkably distinct from each other and magmatic system 1. We therefore link the highly enriched crustal isotopic signatures in member C material reported by Doe *et al*. (1982) and Hildreth *et al*. (1991) from their associated SiO_2 contents to our suite C2 from magmatic system 3. These signatures were attributed (Hildreth *et al*., 1991; Christiansen, 2001) to syn-eruptive melting of the foundering magma chamber roof following caldera collapse associated with eruption of members A and B. In contrast, our data show that suite C2 is unrelated to rhyolitic melts from members A and B and derives from an independent magmatic system.

Although magmatic system 3 shows a large compositional range (e.g. Fig. 8), compositions are clustered, particularly of groundmass glass (Figs. 16, 17). This feature suggests that magmatic system 3 (like systems 1 and 2) contained multiple melt-dominant bodies that were, based on unimodal pressure estimates (Supplementary Data Fig. S17), predominantly laterally separated. Despite the similar isotopic compositions (Figs 13-15) of magmatic systems 3 and 4, there is no evidence of significant mixing between them, suggesting a physical separation of the two. However, isotopic data equally imply that they

have a shared petrogenetic pathway that is distinct from systems 1 and 2. The lower-silica nature of devitrified samples from system 4, if pressure estimates from groundmass glass from low-silica suite A2 are used for comparison (Fig. S17), implies that melt-dominant material in system 4 was stored at greater depths than that for system 3.

Despite their inferred existence during eruption of members A and B, magmatic systems 3 and 4 did not vent at this time. However, the notably smaller crystal sizes (≥85 % of crystals <1 mm) in clasts from these systems relative to those from magmatic system 1 (up to 4-8 mm: Table 1), suggests that all the member C melt-dominant bodies were generated during the B-C time gap, but from systems that had longer histories. The bipyramidal quartz in clasts from system 3 suites can be interpreted to reflect a pulse of accelerated crystallisation shortly prior to eruption, as prolonged growth tends to result in crystals that have contrasting shapes (Laporte & Provost, 1994; Hosaka *et al*., 1995; Manley, 1996). Euhedral, bi-pyramidal quartz has been experimentally reproduced by moderate undercooling of hydrous silicate melts (Swanson & Fenn, 1986), suggesting that rapid extraction of magma from the root zone to shallow levels led to the onset of quartz crystallisation. Published quartz growth rates support this inference, with 1 mm quartz crystals forming in ~3 ka (using rim growth rates of 10^{-13} m/s: Gualda *et al*., 2012) to ~60 days (using growth rates of $2x10^{-10}$ m/s: Swanson & Fenn, 1986), spanning the years to decades estimate for the B-C time break.

The HRT magmatic complex was thus an extraordinary entity, covering four compositionally and isotopically distinct magmatic systems, each of which had a unique combination of factors controlling its erupted compositions. Magmatic systems 1 and 2 were hosted in crust that was less enriched, inferred to reflect large-scale modification during Eocene (and earlier) Absaroka-type magmatism. Magmatic systems 3 and 4 were hosted in highly enriched Archean crust, and a major crustal boundary must therefore lie across the overall HRT caldera area. The HRT mafic magmas with their notably high concentrations of LILE and HFSE (e.g. Ba and Zr; Figs 8, S7) acted, through their earlier crustal intrusions and cumulates, to control assimilation/fractionation trends in magmatic systems 1, 2 and 3, but only directly interacted syn-eruptively with magmatic system 1. In contrast, magmatic system 4 shows an influence from sources that are closer to the regional Snake River Plain olivine tholeiites in composition. Unexpectedly also, scoria with tholeiitic affinities has also been identified as a component in member B from its northern sector, and it appears that the two contrasting mafic lineages both interacted syn-eruptively into high levels of the re-organised magmatic system 1.

Thermal and chemical drivers of the HRT magmatic complex

The ultimate thermal and chemical drivers of the HRT silicic magmatic complex, as in the YPVF to the present day, are mafic magmas feeding and forming the root zone to the overall area (Hildreth, 1981; Hildreth *et al*., 1991; Christiansen, 2001; Huang *et al*., 2015). Most co-erupted mafic enclaves in members A and B (suite 1 HRT mafics of Swallow *et al*., 2018b; labelled suite M1 here) are related to Craters of the Moon-type eruptives seen elsewhere in the Snake River Plain (Leeman *et al*., 1976; Christiansen & McCurry, 2008; Putirka *et al*., 2009). The HRT suite M1 compositions owe their distinctive features to an origin in lithospheric mantle enriched by high *P-T* fluids emanating from the subducted Farallon slab (Swallow *et al*., 2018b). In contrast to earlier views (Christiansen, 2001; Christiansen & McCurry, 2008), we infer that the great majority of erupted silicic material in the HRT (from magmatic systems 1-3) is related to these HRT mafics, rather than olivine tholeiitic compositions (Suite 2 of Swallow *et al*., 2018b; suite M2 here: Fig. 26). The latter are petrogenetically linked to and are inferred to have been the driver to magmatic system 4, and form a minor component, opportunistically syn-eruptively vented, invading part of magmatic system 1. Both mafic root zones were simultaneously active prior to and during the HRT eruption, reflected in the pre-HRT olivine tholeiitic Junction Butte Basalt (Christiansen, 2001), the presence of suite M1 compositions in members A and B, compositions of both mafic types in member B, and co-eruption of magmatic systems 3 and 4 that show separate affinities to both mafic suites. This contemporaneity is paralleled by work reporting Craters of the Moon-type lavas sandwiched in olivine tholeiite lavas along the Snake River Plain as early as ~3.7 Ma (Potter *et al*., 2018).

The presence of mafic material in members A and B, and elevated temperatures derived from type J4 scoria-bearing pumices (Supplementary Data Fig. S16), support a major thermal role for mafic magma in the HRT system. The distinct stratigraphic occurrence and vesicular nature of scoria in member B, relative to dense mafics in member A, suggest a renewed mafic influx associated with eruption of member B. Although a direct mafic triggering of the member B eruption is not established here, the mixing between melt-dominant bodies (suites A1 and A2 to yield suite B1) in the time break between members A and B may reflect a renewed influx of mafic magma into the silicic part of magmatic system 1. Furthermore, an earlier influx of mafic magma likely led to remelting of sanidine-bearing cumulates and the generation of suite A2 compositions. Although there is no physical evidence of mafic magma influx in member C, the presence of less evolved sanidine compositions in rims relative to

cores in samples from magmatic system 3 is consistent with a late-stage thermal input during formation of the melt-dominant bodies.

Rhyolite petrogenesis at Yellowstone

Recent debate around the dominant mechanism of rhyolite petrogenesis in the YPVF, involves end-member views suggesting crustal partial melting (Bindeman *et al*., 2008; Loewen & Bindeman, 2015) and fractional crystallisation from a long-lived crystal mush zone (Girard & Stix, 2009, 2010; Stelten *et al*., 2015, 2017). Our data indicate that systems conforming to both end-member views were present within the HRT magmatic complex. The diversity of compositions within the HRT, particularly isotopically, is not only unique to the YPVF (Hildreth *et al*., 1984, 1991; Christiansen, 2001) but also in regard to the Snake River Plain as a whole. Large-scale isotopic studies of YSRP volcanic products indicate that although there is an increased crustal signature linked to the volcanic focus traversing the western edge of the North American craton, glass isotopic signatures in silicic tephra erupted through cratonic crust are moderate ($\varepsilon_{Nd} \geq -11$: Nash *et al*., 2006) in contrast to the HRT magmatic systems 3 and 4 ($\varepsilon_{Nd} = -17.3$ to -18.2: Fig. 13). Other rhyolitic pyroclastic products from the Snake River Plain with similar crustal isotopic signatures to the HRT systems, e.g., the Arbon Valley Tuff (Nash *et al*., 2006; Drew *et al*., 2013, 2016), have been linked to the commencement of activity at a new centre (Colón *et al*., 2018). This situation is interpreted as representing either crustally-dominated magmatism prior to the full impingement of a mantle plume, or that the 'crustal' magmatic system was isolated from subsequent more mantle-like isotopic systems (Drew *et al*., 2013). The chemical and isotopic diversity in the HRT show that the latter situation was the case. As the isotopic signatures of the sources to Yellowstone magmas are thought to result from hybridisation of Archean crust, mantle-derived melts and mafic intrusives (Doe *et al*., 1982; Hildreth *et al*., 1991; Swallow *et al*., 2018b), more enriched isotopic signatures therefore logically indicate a greater crustal component. With continued mafic influx, this crustal component will be diluted and result in a trend towards less extreme isotopic compositions, as seen in the YPVF (Hildreth *et al*., 1984, 1991) and farther west in the Snake River Plain (Drew *et al*., 2013, 2016). However, the bimodality in isotopic compositions within the HRT indicates that in this case at least, dilution of the 'crustal' signature was a dominantly spatial rather than a temporal feature. Eocene magmatism of the Absaroka Volcanic Province overlaps with the Yellowstone area (Chadwick, 1970; Christiansen & Yeats, 1992; Feeley, 2003) and would have significantly

hybridised and 'pre-conditioned' the lithosphere beneath for the onset of Quaternary hotspot-related volcanism (Swallow *et al*., 2018b). The isotopic contrasts between magmatic systems 1+2, *versus* 3+4 are thus interpreted to reflect the contrasts between these systems being lodged in crust that was was not affected by Eocene magmatism, versus crust that was, respectively.

Others have also suggested a complex nature to rhyolite petrogenesis, not only in the HRT but in the YPVF as a whole (e.g. Bindeman *et al*., 2008; Watts *et al*., 2012; Wotzlaw *et al*., 2015). These studies suggest that the melt-dominant bodies that have fed volcanism in the YPVF are heterogeneous and either represent discrete long-lived melt-dominant bodies, or the late-stage and rapid accumulation of multiple melt-dominant bodies. We demonstrate here, with a single clast-focused approach, that not only were multiple melt-dominant bodies present to feed the HRT eruption, but also multiple magmatic systems. Wotzlaw *et al*. (2015) report a bimodality of zircon Hf isotopic compositions in member A whole-rock samples, with 'more crustal' and 'more mantle-like' populations. The 'more crustal' population is absent in member B but reappears in member C, in contrast to the 'mantle-like population' that shows the reverse. The appearance of a distinct zircon Hf isotopic population in members A and C, but not B, is parallel to our results on the low-Ba magmatic system 2 which, however, is not strongly crustal in its single clast isotopic signature.

Overview of the Yellowstone magmatic systems

YPVF silicic volcanism has been categorised as a 'hot-dry' system (Loewen & Bindeman, 2016). Although this label is archetypically linked to the pumice-poor, intensely welded ignimbrites of the Snake River Plain, with magmas inferred to be >900 °C and H_2O-poor (Branney *et al*., 2008; Ellis *et al*., 2013), explosive eruption deposits in the YPVF are somewhat different and contain more abundant pumice (Christiansen, 2001). Although the HRT silicic magmas cover a large overall temperature range (e.g. zircon saturation temperatures of 790-960 °C), they were cooler and H_2O-richer (up to 5 wt %: Myers *et al*., 2016; this study) than the earlier Snake River Plain magmas. The HRT rhyolitic magmas are in turn hotter than recent YPVF lava-dominated volcanism, which yields temperature estimates as low as 720 °C, depending on the proxy and calibration used (e.g. Watts *et al*., 2012; Loewen & Bindeman, 2015; Stelten *et al*., 2015; Befus & Gardner, 2016). Two-feldspar thermometry estimates of >900 °C and the presence of pigeonite compositions as cores or inclusions also provide indications of a hotter and H_2O-poorer beginning to the HRT

magmatic complex before its evolution to a cooler and H_2O-richer final state. These transitional characteristics, therefore, mean that the HRT straddles the division between 'hot-dry' and 'cold-wet' types of silicic magmas set by Loewen & Bindeman (2016) at ~825 °C. One could therefore propose that the HRT magmas be classified as 'tepid-moist' on the basis of such an arbitrary division.

Heterogeneity is present in YPVF eruptive products on multiple scales, from crystal populations within a single eruption (e.g. Bindeman *et al*., 2008; Ellis & Wolff, 2012; Watts *et al*., 2012; Wotzlaw *et al*., 2015) to variable compositions across an eruptive episode (e.g. Girard & Stix, 2009, 2010; Loewen & Bindeman, 2015; Stelten *et al*., 2015; Troch *et al*., 2017), both related to heterogeneity within a single magmatic system. The perception of a single magmatic system has fitted in conveniently with the modern, unitary low-velocity zone (i.e. 'magma body') geophysically imaged beneath the YPVF (Smith *et al*., 2009; Farrell *et al*., 2014; Huang *et al*., 2015). Although broad-scale imaging, with a resolution of ~10 km obscuring finer details (e.g. Lowenstern *et al*., 2006), can identify the broad dimensions of large-scale crustal anomalies, analysis of past eruption deposits sheds light on the nature of possible heterogeneities within the 'magma body.' Post-dating the HRT, eruptives of analytically indistinguishable ages, but contrasting magma sources, are known, including the domes post-dating the ~1.3 Ma Mesa Falls Tuff (Troch *et al*., 2017; Stelten *et al*., 2018; Rivera *et al*., 2018), and the two magma types in the 0.63 Ma Lava Creek Tuff (Christiansen, 2001). Even so, the presence of four independent magmatic systems contemporaneously active within the YPVF and having these venting in one (albeit punctuated) eruption is remarkable. Furthermore, the HRT magmatic systems included multiple melt-dominant bodies that did not simply merge downwards into a unitary magma chamber, but retained their distinctive natures deep into the magmatic system. The presence of focused zones of eruptible melt-rich magma within a larger magmatic system is important in consideration of future eruptions and hazard modelling (Christiansen *et al*., 2007). This is because although the current percentage of melt in the YPVF upper crustal magmatic system is thought to be too low to be eruptible (Smith *et al*., 2009; Farrell *et al*., 2014; Huang *et al*., 2015), this melt could be concentrated in regions too small to be detected by present imaging techniques.

The evacuation of multiple melt-dominant bodies in pre-Quaternary YSRP eruptions appears to be common (Perkins *et al*., 1995; Cathey & Nash, 2004; Bonnichsen *et al*., 2008; Ellis & Wolff, 2012). Although there is a lack of single-clast data (Branney *et al*., 2008), the presence of multiple modes in crystal and glass compositions is parallel to what is seen in the HRT. But why multiple melt-dominant bodies should form and remain molten in the crust

prior to eruption is puzzling. Small melt-dominant bodies should solidify quicker than large bodies and therefore be transient features or be kept melt-dominant only through continuing inputs of heat and/or volatiles. Although volcanism in the Snake River Plain is high temperature (>900 °C: Branney *et al*., 2008), and HRT temperature estimates extend to similar values, estimated final storage temperature for the HRT magmas are moderate (~780-900 °C). However, the modern thermal and gas fluxes in the YPVF reflect a large magma flux from the mantle and lower crust, related to the Yellowstone plume (e.g. Lowenstern *et al*., 2006, 2014; Huang *et al*., 2015). If this abundant thermal flux pre-dated the surface volcanism then it could have thermally pre-conditioned the crust to allow small melt-dominant bodies to survive in the upper crust. Another consideration is the tectonic regime along the YRSP related to Basin and Range extension (e.g. Pierce & Morgan, 1992, 2009; Smith *et al*., 2009), as multiple co-existing melt-dominant rhyolite bodies have been reported from rifting areas (e.g. Taupo Volcanic Zone: Shane *et al*., 2007, 2008; Cooper *et al*., 2012; Bégué *et al*., 2014). Extensional tectonics would likely enhance the geothermal gradient in such settings and aid the ascent of magma and rapid formation of melt-dominant bodies (e.g. Allan *et al*., 2013, 2017). It is inferred that a combination of elevated heat flow and extensional tectonics in the early stages of development of the YPVF helped develop the unusually heterogeneous magmatic complex that is represented in the HRT.

Implications for global silicic magmatic systems

Although focused on a single caldera-forming eruption, this study raises several general issues around silicic eruptions and their source magmatic systems.

(1) The HRT, previously considered to represent one eruption (Reynolds, 1977; Hildreth *et al*., 1991; Christiansen, 2001), raises questions surrounding the distinction between one, multi-phase event and multiple distinct eruptions. Were three ignimbrite caldera-forming eruptions to occur today, each separated by periods of months to decades, and exhibiting compositional differences between each eruption, they would likely be considered distinct, at least on human timescales. Evidence for time breaks within eruptive sequences is therefore crucial in providing a framework for geochemical studies and providing a more realistic representation of the eruption cycle. Although this is increasingly challenging further back in the geological record, eruptions separated by similar time gaps have been identified as distinct events (e.g. Barker *et al*., 2016; Cooper *et al*., 2017).

(2) The HRT is another example, albeit extreme in size and complexity, of a silicic eruption tapping multiple melt-dominant bodies (cf. Sampson & Cameron, 1987; Shane *et al*., 2007, 2008; Cooper *et al*., 2012, 2016; Westgate *et al*., 2013; Bégué *et al*., 2014). In contrast, numerical models associated with large silicic magmatic systems do not reflect this complexity and are based on single unitary bodies (e.g. Jellinek & DePaolo, 2003; Gregg *et al*., 2012, 2015; Caricchi *et al*., 2014). The complex configurations of silicic magmatic systems indicated by field-based studies would have important, and variable, thermomechanical effects on the magmatic system (Gudmundsson, 2012), and it is arguably important to narrow the gap between field-based evidence and numerical model assumptions.

(3) There was rapid (syn-eruptive) accumulation of melt-dominant bodies in the HRT, with changes from members A to B within months and B to C within decades. Such rapid behaviour has been inferred elsewhere (e.g. Oruanui: Charlier *et al*., 2008, Allan *et al*., 2013, 2017; Rocky Hill/Kidnappers: Cooper *et al*., 2016, 2017; Santorini: Druitt *et al*., 2012). However, this rapidity is in contrast to the assumption that large magma bodies take 10^5-10^6 years to grow and that their growth to a given size controls the repose period prior to eruption (e.g. Smith, 1979; Jellinek & DePaolo, 2003; Reid, 2008). This study, as with others (e.g., Druitt *et al*., 2012; Till *et al*., 2015; Barker *et al*., 2016; Allan *et al*., 2017) indicates that large-scale silicic magmatic systems can rejuvenate or create eruptible melt-dominant bodies on short timescales, such as within the years-decades time break between members B and C for magmatic systems 2 to 4.

(4) Not only is the presence of multiple independent melt-dominant bodies in the HRT notable, but so also is the presence of multiple independent magmatic systems. The simultaneous or systematic construction and evacuation of magma bodies related to spatially and/or chemically distinct magmatic lineages has been documented elsewhere (e.g. Long Valley: Sampson & Cameron, 1987; Taupo Volcanic Zone: Brown *et al*., 1998; Shane *et al*., 2007, 2008; Allan *et al*., 2012, 2017; Bégué *et al*., 2014; Campi Flegrei: Pistolesi *et al*., 2016), but not on such a large scale. On a broader spatial and temporal scale, periods of intense silicic volcanism comprising multiple caldera-forming eruptions over geologically short periods of time are labelled ignimbrite flare-ups (e.g. Bonnichsen *et al*., 2008; Best *et al*., 2013; Lipman & Bachmann, 2015; Gravley *et al*., 2016). In the Taupo Volcanic Zone, eight caldera-forming eruptions, evacuating 2-3,000 km^3 dense-rock equivalent of material, occurred within an area of 90 x 40 km over a ~100 kyr period (Houghton *et al*., 1995; Gravley *et al*., 2016). In comparison, the HRT erupted ~2,500 km^3 dense-rock equivalent of

material and formed a caldera of ~95 x 65 km (Christiansen, 2001) that encloses the entire collapse area of the TVZ examples. The HRT caldera thus covers an area as large or larger, than other terrestrial volcanic regions that contained multiple magmatic systems that, in the example quoted, were evacuated mostly as singular eruptions separated by periods long enough for erosion and soil formation.

CONCLUSIONS

The 2.08 Ma, ~2,500 km^3 HRT comprises three ignimbrite members (A, B and C) and two sets of fall deposits, an initial one beneath member A and another beneath member C (Christiansen, 2001). The eruption was episodic and prolonged, with spasmodic initial fall activity over several weeks, and with a weeks to months-long time break between members A and B, and a years- to decades-long interlude between members B and C (Figs 2, S1). The eruption products include silicic juvenile material exhibiting a wide diversity of physical characteristics, with variations in the size and abundance of crystals, nature/degree of vesicularity, growth of microlites and mixing with mafic scoria. Crystal-rich (11-22 wt %), vesicular pumices and their devitrified fiamme equivalents (clast type J1) dominate in the sample suite from members A and B, where a coarse-grained (up to 10 mm) crystal assemblage is ubiquitous (Table 1). Scoria-bearing, mingled pumices and fiamme (type J4) are present in member B. Also present in these members are two types (types J2, J3) of less vesicular clasts with darkened groundmass glass, with type J3 containing characteristic coarse euhedral feldspars. Member C juvenile clast types (types J5 to J9) are uniformly distinct for their consistently small crystal sizes (<3 mm) and crystal-poorer natures (<15 wt %). In contrast, however, member C clast types range in physical characteristics from dense black material (J5) to highly vesicular pumices (J8) and their devitrified fiamme equivalents (J9).

The physical diversity of juvenile clasts in the HRT is mirrored in a remarkable degree of geochemical diversity within and between the ignimbrite members. This diversity reveals that the magmatic complex that gave rise to the HRT was extraordinary. Taken together, single clast major and trace element, and isotopic compositions, coupled with matrix glass and mineral compositions from samples constrained within a chronostratigraphically controlled framework show the following:

(1) Four magmatic systems, with distinct chemical and radiogenic isotopic signatures (Table 4), were involved during the HRT eruption. From the eruption onset, the initial fall deposits (Myers *et al*., 2016; Swallow *et al*., 2018a) and earliest member A ignimbrite

evacuated two systems, the major magmatic system 1 and the minor low-Ba system 2. The former includes the dominant A1 suite of compositions, separated by a compositional gap from the low-silica A2 suite, which is notably elevated in Ba and Zr. Suite A1 shows wide variations (e.g., 450-1680 ppm Ba) but is separated from suite A3 from magmatic system 2 based on trace elements (e.g., 140-250 ppm Ba) and characterised by low-Cn (<0.35 mol%) sanidine rim compositions. Member B represents the evacuation of only magmatic system 1, with a cessation in evacuation of system 2. Mixing throughout system 1 occurred prior to the eruption of member B, indicated by the closing of the compositional gap in member A (suites A1 and A2 condensed into suite B1), the presence of mixed, scoria-bearing pumices, and greater mineral and glass compositional variations within single clasts relative to member A. The mafic end-member for this mixing event mostly belonged to the distinctive HRT mafics suite of Swallow *et al*. (2018b) (part of suite M1 here), consistent with its long-term role in the petrogenetic development of magmatic system 1. However, analysed scoria from north of the caldera has tholeiitic affinities, and was an apparently opportunistic infiltrator into the silicic magma body during eruption of member B (and subsequently: Pritchard *et al*., 2013). The coherency of crystal compositions between members A and B indicate that the mafic mixing was rapid enough such that there was no development of contrasting overgrowths on crystals (cf. Wark *et al*., 2007; Chamberlain *et al*., 2014b). Member C contains material from two new, compositionally distinct magmatic systems, but with similar, crustally-influenced isotopic compositions: the larger magmatic system 3 and the smaller system 4. System 3 generated high-silica rhyolite magmas that exhibit large trace element compositional variations (e.g. 410-2280 ppm Ba). System 4 generated a range of dacitic to rhyolitic compositions (65.6-75.9 wt % SiO_2), with many compositional trends pointing towards broadly tholeiitic sources, rather than the 'HRT mafics' source. Member C also involved the reappearance of newly-generated magma from system 2 (suite C3) but, conversely, material from magmatic system 1 is absent. Although previous studies have highlighted heterogeneity of the HRT in its isotopic characteristics (e.g. Doe *et al*., 1982; Hildreth *et al*., 1991) and crystal cargo (e.g. Wotzlaw *et al*., 2015), the details presented here highlight the advantages of analysing single pyroclasts and their components.

(2) Elemental and isotopic compositions of products from the different magma systems suggest that a variety of petrogenetic mechanisms operated prior to the HRT eruption. Lead isotopic constraints, coupled with the high-Ba and Zr nature of magmatic system 1, indicate that this and system 2 are petrogenetically related to the co-erupted HRT mafic clasts (Swallow *et al*., 2018b). Moderate offsets to more crustally influenced isotopic compositions

in magmatic systems 1 and 2 relative to HRT mafic compositions suggests a control on rhyolite compositions dominantly by fractional crystallisation with only minor assimilation. Compositional variations and gaps within systems 1 and 2 can be explained through a multi-stage partial melting scenario, with the erupted high-silica rhyolites (e.g., suite A1) extracted from a sanidine-rich mush which was in turn re-melted (e.g. Wolff, 2017) to generate suite A2 compositions. In contrast, magmatic systems 3 and 4 in member C contain significantly more enriched isotopic compositions, consistent with greater degrees of assimilation of Archean crustal rocks (Figs. 13, 26). Whilst the high-Ba nature of magmatic system 3 indicates a continuing role for HRT mafic compositions, in contrast the low-Ba, high-Sc nature of system 4 links it to a pyroxene-bearing olivine tholeiitic root zone. Despite the contrasting elemental compositions between these two member C suites, their isotopic compositions are comparable and can be similarly explained through crustal contamination of partial melts of mafic cumulates, derived from contrasting mafic lineages (system 3-HRT mafics; system 4-olivine tholeiites). These newly-erupted member C systems, coupled with the rejuvenation of the fractional crystallisation-controlled magmatic system 2, illustrate the wide diversity in petrogenetic mechanisms represented in the HRT. This variability suggests that rhyolite petrogenesis in the YPVF is complex and diverse, and may be more complex than considered in other end-member models (cf. Loewen & Bindeman, 2015; Stelten *et al*., 2015).

(3) Groundmass glass compositions from magmatic systems 1-3 (magmatic system 4 is only represented by devitrified material) show clustering, indicative of the presence of multiple, distinct melt-dominant bodies. As this clustering is consistent in the fall deposits (Myers *et al*., 2016; Swallow *et al*., 2018a) and the ignimbrite, this configuration in the relevant magmatic system was not confined to the upper (earlier-erupted) levels but persisted throughout evacuation of the systems. Broadly comparable estimates of storage pressures/depths from volatile contents in melt inclusions (Myers *et al*., 2016) and glass major element compositions (Supplementary Data Fig. S17) imply that these bodies were predominantly laterally rather than vertically separated (Figs. 25, 26). This arrangement appears to be a common feature of large silicic caldera-forming eruptions (e.g. Cooper *et al*., 2012, 2016; Ellis & Wolff, 2012; Bégué *et al*., 2014). However, this complex, multiple-body nature of magmatic systems is not incorporated into numerical models of magma bodies, leading to a gap that requires filling between investigations based on detailed field study and model frameworks, which require simplicity.

(4) Syn-eruptive magmatic processes within the HRT were rapid. Within the inferred weeks to months-long time break between members A and B, mixing related to renewed influx of HRT mafic material occurred, closing the compositional gap present in member A between suites A1 and A2. Furthermore, the absence of material derived from magmatic systems 3 and 4 in members A and B suggests that melt-dominant bodies in these systems were either not present, or were not in a state to be tapped at this stage of the eruption. This observation, at one extreme, constrains rapid formation of these melt-dominant bodies to in the years-decades time break between members B and C, further linked by the uniformly small (<3 mm) crystal size across all member C juvenile material. This time break also saw rejuvenation of magmatic system 2. Whilst further mineral-specific studies are required to better constrain timescales of melt-dominant body formation in the HRT, our inferences on the rapidity with which the HRT systems behaved are consistent with findings from other large-scale silicic systems (e.g. Charlier *et al*., 2008; Allan *et al*., 2013, 2017; Cooper *et al*., 2016, 2017).

(5) Temperature estimates from erupted material in the HRT show a broad range of values, indicating temporal and spatial heterogeneity within the HRT magmatic complex. These estimates (Supplementary Data Fig. S16) yield temperatures of ~780-900 °C that lie between the higher temperatures associated with most Snake River Plain silicic volcanism (>900°C: e.g. Branney *et al*., 2008) and lower temperatures inferred from the youngest episodes of volcanism in the YPVF (<800 °C: e.g., Loewen & Bindeman, 2015; Stelten *et al*., 2015; Befus & Gardner, 2016). Whether this represents a cooling overall magmatic system (e.g. Watts *et al*., 2012) or distinct differences between the various volcanic centres is not clearly established. However, incorporation of the YPVF into the 'hot-dry' rhyolite category associated with the Snake River Plain appears overly simplistic (e.g. Loewen & Bindeman, 2016), and Yellowstone silicic products in general and the HRT eruption products in particular defy simple pigeonholing.

(6) The mapped HRT caldera and total eruptive volume (Christiansen, 2001) are comparable in size to regions in other silicic volcanic provinces that experienced clusters of caldera-forming eruptions ('flare-ups') from multiple volcanic centres over periods of ~10^5 years (e.g. Taupo Volcanic Zone: Houghton *et al*., 1995; Gravley *et al*., 2016). The HRT could be considered some ways as a 'flare-up', but on a compressed timescale, with the effectively collective (rather than separated) eruption of multiple independent magmatic systems. Subsequent volcanism in the YPVF shows evidence for complex mineral

assemblages and stratigraphic relationships (e.g. Christiansen, 2001; Troch *et al*., 2017; Stelten *et al*., 2018; Wilson *et al*., 2018). Our results suggest that other eruptive units in the YPVF deserve closer scrutiny to determine if the situation for the HRT is the norm or exception for large eruptions at Yellowstone.

SUPPLEMENTARY DATA

Supplementary material and electronic appendices of data for this paper are available at Journal of Petrology online.

ACKNOWLEDGEMENTS

C. J. N. Wilson thanks R. L. Christiansen for an introduction to the Huckleberry Ridge Tuff, and the Yellowstone (YELL-05248) and Grand Teton (GRTE-00604) research offices for permission to work in the respective national parks, and the help and support of their staff over many years. Discussions on Yellowstone matters with Simon Barker, Jake Lowenstern, Madison Myers and Paul Wallace are gratefully acknowledged. We also acknowledge the late John Watson, Mike Rowe and Annette Rodgers for XRF analytical services, and thank Adam Kent, Dan Morgan, Ian Schipper and Dan Sinclair for their help with data collection and processing. Detailed reviews by Ben Ellis, Kurt Knesel, Madison Myers and Mike Rowe are much appreciated.

FUNDING

E. J. Swallow acknowledges with thanks the receipt of a Commonwealth Scholarship, administered by Universities New Zealand – Te Pōkai Tara. We also acknowledge past support from the Marsden Fund (grant VUW0813) and award of a James Cook Fellowship to C. J. N. Wilson, both administered by the Royal Society of New Zealand.

REFERENCES

Allan, A. S. R., Wilson, C. J. N., Millet, M.-A. & Wysoczanski, R. J. (2012). The invisible hand: tectonic triggering of a rhyolitic supereruption. *Geology* **40**, 563-566.

Allan, A. S. R., Morgan, D. J., Wilson, C. J. N. & Millet, M.-A. (2013). From mush to eruption in centuries: assembly of the super-sized Oruanui magma body. *Contributions to Mineralogy and Petrology* **166**, 143-164.

Allan, A. S. R., Barker, S. J., Millet, M.-A., Morgan, D. J., Rooyakkers, S. M., Schipper, C. I. & Wilson, C. J. N. (2017). A cascade of magmatic events during the assembly and eruption of a super-sized magma body. *Contributions to Mineralogy and Petrology* **172**, 49.

Almeev, R. R., Bolte, T., Nash, B. P., Holtz, F., Erdmann, M. & Cathey, H. E. (2012). High-temperature low H_2O silicic magmas of the Yellowstone hotspot: an experimental study of rhyolite from the Bruneau-Jarbidge eruptive center, central Snake River Plain, USA. *Journal of Petrology* **53**, 1837-1866.

Armstrong, R. L., Leeman, W. P. & Malde, H. E. (1975). K-Ar dating Quaternary and Neogene volcanic rocks of the Snake River Plain, Idaho. *American Journal of Science* **275**, 225-251.

Bachmann, O. & Bergantz, G. W. (2004). On the origin of crystal-poor rhyolites: extracted from batholithic crystal mushes. *Journal of Petrology* **45**, 1565-1582

Bachmann, O. & Bergantz, G. W. (2008) Deciphering magma chamber dynamics from styles of compositional zoning in large silicic ash flow sheets. *Reviews in Mineralogy and Geochemistry* **69**, 651-674.

Bachmann, O. & Huber, C. (2016). Silicic magma reservoirs in the Earth's crust. *American Mineralogist* **101**, 2377-2404.

Bachmann, O., Dungan, M. A. & Lipman, P. W. (2002). The Fish Canyon magma body, San Juan volcanic field, Colorado: rejuvenation and eruption of an upper-crustal batholith. *Journal of Petrology* **43**, 1469-1503.

Bachmann, O., Deering, C. D., Lipman, P. W. & Plummer, C. (2014). Building zoned ignimbrites by recycling silicic cumulates: insight from the 1,000 km^3 Carpenter Ridge Tuff, CO. *Contributions to Mineralogy and Petrology* **167**, 1025.

Bacon, C. R. (1983). Eruptive history of Mount Mazama and Crater Lake caldera, Cascade Range, USA. *Journal of Volcanology and Geothermal Research* **18**, 57-115.

Bacon C. R. & Druitt, T. H. (1988). Compositional evolution of the zoned calcalkaline magma chamber of Mount Mazama, Crater Lake, Oregon. *Contributions to Mineralogy and Petrology* **98**, 224-256.

Barker, S. J., Wilson, C. J. N., Smith, E. G. C., Charlier, B. L. A., Wooden, J. L., Hiess, J. & Ireland, T. R. (2014). Post-supereruption magmatic reconstruction of Taupo volcano (New Zealand), as reflected in zircon ages and trace elements. *Journal of Petrology* **55**, 1511-1533.

Barker, S. J., Wilson, C. J. N., Allan, A. S. R. & Schipper, C. I. (2015). Fine-scale temporal recovery, reconstruction and evolution of a post-supereruption magmatic system. *Contributions to Mineralogy and Petrology* **170**, 5.

Barker, S. J., Wilson, C. J. N., Morgan, D. J. & Rowland, J. V. (2016). Rapid priming, accumulation and recharge of magma driving recent eruptions at a hyperactive caldera volcano. *Geology* **44**, 323-326.

Befus, K. S. & Gardner, J. E. (2016). Magma storage and evolution of the most recent effusive and explosive eruptions from Yellowstone Caldera. *Contributions to Mineralogy and Petrology* **171**, 30.

Bégué, F., Deering, C. D., Gravley, D. M., Kennedy, B. M., Chambefort, I., Gualda, G. A. R. & Bachmann, O. (2014). Extraction, storage and eruption of multiple isolated magma batches in the paired Mamaku and Ohakuri eruption, Taupo Volcanic Zone, New Zealand. *Journal of Petrology* **55**, 1653-1684.

Best, M. G., Gromme, S., Deino, A. L., Christiansen, E. H., Hart, G. L. & Tingey, D. G. (2013). The 36-18 Ma Central Nevada ignimbrite field and calderas, Great Basin, USA: multicyclic super-eruptions. *Geosphere* **9**, 1562-1636.

Bindeman, I. N. & Simakin, A. G. (2014). Rhyolites-hard to produce, but easy to recycle and sequester: integrating microgeochemical observations and numerical models. *Geosphere* **10**, 930-957.

Bindeman, I. N. & Valley, J. W. (2001). Low- $\delta^{18}O$ rhyolites from Yellowstone: magmatic evolution based on analyses of zircons and individual phenocrysts. *Journal of Petrology* **42**, 1491-1517.

Bindeman, I. N., Fu, B., Kita, N. T. & Valley, J. W. (2008). Origin and evolution of silicic magmatism at Yellowstone based on ion microprobe analysis of isotopically zoned zircons. *Journal of Petrology* **49**, 163-193.

Birck, J. L. (1986). Precision K-Rb-Sr isotopic analysis: application to Rb-Sr chronology. *Chemical Geology* **56**, 73-83.

Bolte, T., Holtz, F., Almeev, R. & Nash, B. (2015). The Blacktail Creek Tuff: an analytical and experimental study of rhyolites from the Heise volcanic field, Yellowstone hotspot system. *Contributions to Mineralogy and Petrology* **169**, 15.

Bonnichsen, B., Leeman, W. P., Honjo, N., McIntosh, W. C. & Godchaux, M. M. (2008). Miocene silicic volcanism in southwestern Idaho: geochronology, geochemistry, and evolution of the central Snake River Plain. *Bulletin of Volcanology* **70**, 315-342.

Bouvier, A., Vervoort, J. D. & Patchett, P. J. (2008). The Lu-Hf and Sm-Nd isotopic composition of CHUR: constraints from unequilibrated chondrites and implications for the bulk composition of terrestrial planets. *Earth and Planetary Science Letters* **273**, 48-57.

Branney, M. J., Bonnichsen, B., Andrews, G. D. M., Ellis, B., Barry, T. L. & McCurry, M. (2008). 'Snake River (SR)-type' volcanism at the Yellowstone hotspot track: distinctive products from unusual high-temperature silicic super-eruptions. *Bulletin of Volcanology* **70**, 293-314.

Brey, G. P. & Köhler, T. (1990). Geothermobarometry in four-phase lherzolites II. New thermobarometers, and practical assessment of existing thermobarometers. *Journal of Petrology* **31**, 1353-1378.

Brophy, J. G. (1991). Composition gaps, critical crystallinity, and fractional crystallization in orogenic (calc-alkaline) magmatic systems. *Contributions to Mineralogy and Petrology* **109**, 173-182.

Brown, S. J. A., Wilson, C. J. N., Cole, J. W. & Wooden, J. (1998). The Whakamaru group ignimbrites, Taupo Volcanic Zone, New Zealand: evidence for reverse tapping of a zoned silicic magmatic system. *Journal of Volcanology and Geothermal Research* **84**, 1-37.

Caricchi, L., Annen, C., Blundy, J., Simpson, G. & Pinel, V. (2014). Frequency and magnitude of volcanic eruptions controlled by magma injection and buoyancy. *Nature Geoscience* **7**, 126-130.

Cashman, K. V. & Giordano, G. (2014). Calderas and magma reservoirs. *Journal of Volcanology and Geothermal Research* **288**, 28-45.

Cashman, K. V., Sparks, R. S. J. & Blundy, J. D. (2017). Vertically extensive and unstable magmatic systems: a unified view of igneous processes. *Science* **355**, eaag3055.

Cathey, H. E. & Nash, B. P. (2004). The Cougar Point Tuff: implications for thermomechanical zonation and longevity of high-temperature, large-volume silicic magmas of the Miocene Yellowstone hotspot. *Journal of Petrology* **45**, 27-58.

Chadwick, R. A. (1970). Belts of eruptive centers in the Absaroka-Gallatin Volcanic Province, Wyoming-Montana. *Geological Society of America Bulletin* **81**, 267-274.

Chamberlain, K. J., Wilson, C. J. N., Wooden, J. L., Charlier, B. L. A. & Ireland, T. R. (2014a). New perspectives on the Bishop Tuff from zircon textures ages and trace elements. *Journal of Petrology* **55**, 395-426.

Chamberlain, K. J., Morgan, D. J. & Wilson, C. J. N. (2014b). Timescales of mixing and mobilisation in the Bishop Tuff magma body: perspectives from diffusion chronometry. *Contributions to Mineralogy and Petrology* **168**, 1034.

Chamberlain, K. J., Wilson, C. J. N., Wallace, P. J. & Millet, M.-A. (2015) Micro-analytical perspectives on the Bishop Tuff and its magma chamber. *Journal of Petrology* **56**, 605-640.

Charlier, B. L. A., Ginibre, C., Morgan, D., Nowell, G. M., Pearson, D. G., Davidson, J. P. & Ottley, C. J. (2006). Methods for the microsampling and high-precision analysis of strontium and rubidium isotopes at single crystal scale for petrological and geochronological applications. *Chemical Geology* **232**, 114-133.

Charlier, B. L. A., Wilson, C. J. N. & Davidson, J. P. (2008). Rapid open-system assembly of a large silicic magma body: time resolved evidence from cored plagioclase crystals in the Oruanui eruption deposits, New Zealand. *Contributions to Mineralogy and Petrology* **156**, 799-813.

Christiansen, E. H. (2005). Contrasting processes in silicic magma chambers: evidence from very large volume ignimbrites. *Geological Magazine* **142**, 669-681.

Christiansen, E. H. & McCurry, M. (2008). Contrasting origins of Cenozoic silicic volcanic rocks from the western Cordillera of the United States. *Bulletin of Volcanology* **70**, 251-267.

Christiansen, R. L. (1979). Cooling units and composite sheets in relation to caldera structure. In: Chapin, C. E. & Elston, W. E. (eds) *Ash-Flow Tuffs*. *Geological Society of America Special Papers* **180**, 29-42.

Christiansen, R. L. (2001). *The Quaternary and Pliocene Yellowstone Plateau Volcanic Field of Wyoming, Idaho and Montana*. *U. S. Geological Survey Professional Paper* **729-G**.

Christiansen, R. L. & Yeats, R. S. (1992). Post-Laramide geology of the US Cordilleran region. In: Burchfiel, B. C., Lipman, P. W. & Zoback, M. L. (eds) *The Cordilleran Orogen: Conterminous US*. Boulder, Colorado, Geological Society of America, *The Geology of North America* **G-3**, 261-406.

Christiansen, R. L., Lowenstern. J. B., Smith, R. B., Heasler, H., Morgan, L. A., Nathenson, M., Mastin, L. G., Muffler, L. J. P. & Robinson, J. E. (2007). Preliminary assessment of volcanic and hydrothermal hazards in Yellowstone National Park and vicinity. *U. S. Geological Survey Open File Report* **2007-1071**, 1-94.

Colón, D. P., Bindeman, I. N., Wotzlaw, J.-F., Christiansen, E. H. & Stern, R. A. (2018). Origins and evolution of rhyolitic magmas in the central Snake River Plain: insights from coupled high-precision geochronology, oxygen isotope, and hafnium isotope analyses of zircon. *Contributions to Mineralogy and Petrology* **173**, 11.

Cooper, G. F., Wilson, C. J. N., Millet, M.-A., Baker, J. A. & Smith, E. G. C. (2012). Systematic tapping of independent magma chambers during the 1 Ma Kidnappers supereruption. *Earth and Planetary Science Letters* **313-314**, 23-33.

Cooper, G. F., Wilson, C. J. N., Millet, M.-A. & Baker, J. A. (2016). Generation and rejuvenation of a supervolcanic magmatic system: a case study from Mangakino volcanic centre, New Zealand. *Journal of Petrology* **57**, 1135-1170.

Cooper, G. F., Morgan, D. J. & Wilson, C. J. N. (2017). Rapid assembly and rejuvenation of a large silicic magmatic system: insights from mineral diffusive profiles in the Kidnappers and Rocky Hill deposits, New Zealand. *Earth and Planetary Science Letters* **473**, 1-13.

Deer, W. A., Howie, R. A. & Zussman, J. (1966). *An Introduction to the Rock-Forming Minerals*. Longman, Harlow, U. K.

Deering, C. D., Bachmann, O. & Vogel, T. A. (2011). The Ammonia Tanks Tuff: erupting a melt-rich cap and its remobilized crystal cumulate. *Earth and Planetary Science Letters* **310**, 518-525.

DePaolo, D. J. & Wasserburg, G. J. (1976). Nd isotopic variations and petrogenetic models. *Geophysical Research Letters* **3**, 249-252.

de Silva, S. & Gregg, P. M. (2014). Thermomechanical feedbacks in magmatic systems: implications for growth, longevity, and evolution of large caldera-forming magma reservoirs and their supereruptions. *Journal of Volcanology and Geothermal Research* **282**, 77-91.

Doe, B. R., Leeman, W. P., Christiansen, R. L. & Hedge, C. E. (1982). Lead and strontium isotopes and related trace elements as genetic tracers in the upper Cenozoic rhyolite-basalt association of the Yellowstone Plateau volcanic field. *Journal of Geophysical Research* **87**, 4785-4806.

Drew, D. L., Bindeman, I. N., Watts, K. E., Schmitt, A. K., Fu, B. & McCurry, M. (2013). Crustal-scale recycling in caldera complexes and rift zones along the Yellowstone hotspot track: O and Hf isotopic evidence in diverse zircons from voluminous rhyolites of the Picabo volcanic field, Idaho. *Earth and Planetary Science Letters* **381**, 63-77.

Drew, D. L., Bindeman, I. N., Loewen, M. W. & Wallace, P. J. (2016). Initiation of large-volume silicic centres in the Yellowstone hotspot track: insights from H_2O- and F-rich

quartz-hosted rhyolitic melt inclusions in the Arbon Valley Tuff of the Snake River Plain. *Contributions to Mineralogy and Petrology* **171**, 10.

Druitt, T. H., Costa, F., Deloule, E., Dungan, M. & Scaillet, B. (2012). Decadal to monthly timescales of magma transfer and reservoir growth at a caldera volcano. *Nature* **482**, 77-80.

Elkins, L. T. & Grove, T. L. (1990). Ternary feldspar experiments and thermodynamic models. *American Mineralogist* **75**, 544-559.

Ellis, B. S. & Wolff, J. A. (2012). Complex storage of rhyolite in the central Snake River Plain. *Journal of Volcanology and Geothermal Research* **211-212**, 1-11.

Ellis, B. S., Mark, D. F., Pritchard, C. J. & Wolff, J. A. (2012). Temporal dissection of the Huckleberry Ridge Tuff using the $^{40}Ar/^{39}Ar$ dating technique. *Quaternary Geochronology* **9**, 34-41.

Ellis, B. S., Wolff, J. A., Boroughs, S., Mark, D. F., Starkel, W. A. & Bonnichsen, B. (2013). Rhyolite volcanism of the central Snake River Plain: a review. *Bulletin of Volcanology* **75**, 745.

Ellis, B. S., Bachmann, O. & Wolff, J. A. (2014). Cumulate fragments in silicic ignimbrites: The case of the Snake River Plain. *Geology* **42**, 431-434.

Embree, G. F. & Hoggan, R. D. (1999). Secondary deformation within the Huckleberry Ridge Tuff and adjacent Pliocene units near the Teton Dam: Road log to the regional geology of the eastern margin of the Snake River Plain, Idaho. In: Hughes, S. S. & Trackray, G. D. (eds), *Guidebook to the Geology of Eastern Idaho*. Pocatello, Idaho Museum of Natural History, p. 181–203.

Farrell, J., Smith, R. B., Husen, S. & Diehl, T. (2014). Tomography from 26 years of seismicity revealing the spatial extent of the Yellowstone crustal magma reservoir extends well beyond the Yellowstone caldera. *Geophysical Research Letters* **41**, 3068-3073.

Feeley, T. C. (2003). Origin and tectonic implications of across-strike geochemical variations in the Eocene Absaroka volcanic province, United States. *Journal of Geology* **111**, 329-346.

Folkes, C. B., de Silva, S. L., Wright, H. M. & Cas, R. A. F. (2011). Geochemical homogeneity of a long-lived large silicic system; evidence from the Cerro Galán caldera, NW Argentina. *Bulletin of Volcanology* **73**, 1455-1486.

Fridrich, C. J. & Mahood, G. A. (1987). Compositional layers in the zoned magma chamber of the Grizzly Peak Tuff. *Geology* **15**, 299-303.

Frost, C. D., Frost, B. R., Kirkwood, R. & Chamberlain, K. R. (2006). The tonalite-trondhjemite-granodiorite (TTG) to granodiorite-granite (GG) transition in the late Archean plutonic rocks of the central Wyoming province. *Canadian Journal of Earth Sciences* **43**, 1419-1444.

Geissman, J. W., Holm, D., Harlan, S. S., & Embree, G. F. (2010). Rapid, high-temperature formation of large-scale rheomorphic structures in the 2.06 Ma Huckleberry Ridge Tuff, Idaho, USA. *Geology* **38**, 263-266.

Gerstenberger, H. & Haase, G. (1997). A highly effective emitter substance for mass spectrometric Pb isotope ratio determinations. *Chemical Geology* **136**, 309-312.

Girard, G. & Stix, J. (2009). Magma recharge and crystal mush rejuvenation associated with early post-collapse Upper Basin Member rhyolites, Yellowstone caldera, Wyoming. *Journal of Petrology* **50**, 2095-2125.

Girard, G. & Stix, J. (2010) Rapid extraction of discrete magma batches from a large differentiating magma chamber: the Central Plateau Member rhyolites, Yellowstone caldera, Wyoming. *Contributions to Mineralogy and Petrology* **160**, 441-465.

Gravley, D. M., Deering, C. D., Leonard, G. S. & Rowland, J. V. (2016). Ignimbrite flare-ups and their drivers: a New Zealand perspective. *Earth-Science Reviews* **162**, 65-82.

Gregg, P. M., de Silva, S. L., Grosfils, E. B. & Parmigiani, J. P. (2012). Catastrophic caldera-forming eruptions: thermomechanics and implications for eruption triggering and maximum caldera dimensions on Earth. *Journal of Volcanology and Geothermal Research* **241-242**, 1-12.

Gregg, P. M., Grosfils, E. B. & de Silva, S. L. (2015). Catastrophic caldera-forming eruptions II: the subordinate role of magma buoyancy as an eruption trigger. *Journal of Volcanology and Geothermal Research* **305**, 100-113.

Gualda, G. A. R. & Ghiorso, M. S. (2013). The Bishop Tuff giant magma body: an alternative to the Standard Model. *Contributions to Mineralogy and Petrology* **166**, 755-775.

Gualda, G. A. R., Pamukcu, A. S., Ghiorso, M. S., Anderson, A. T. Jr, Sutton, S. R. & Rivers, M. L. (2012). Timescales of quartz crystallization and the longevity of the Bishop giant magma body. *PLoS ONE* **7**, e37492.

Gualda, G. A. R., Bégué, F., Pamukcu, A. S. & Ghiorso, M. S. (2019). Rhyolite-MELTS vs DERP—Newer does not make it better: a comment on 'The effect of anorthite content and water on quartz-feldspar cotectic compositions in the rhyolitic system and implications for geobarometry' by Wilke *et al*. (2017; Journal of Petrology, 58, 789-818), *Journal of Petrology* (in press: doi:10.1093/petrology/egz003).

Gudmundsson, A. (2012). Magma chambers: formation, local stresses, excess pressures and compartments. *Journal of Volcanology and Geothermal Research* **237-238**,19-41.

Hildreth, W. (1981). Gradients in silicic magma chambers: implications for lithospheric magmatism. *Journal of Geophysical Research* **86**, 10153-10192.

Hildreth, W. (2004). Volcanological perspectives on Long Valley Mammoth Mountain and Mono Craters: several contiguous but discrete systems. *Journal of Volcanology and Geothermal Research* **136**, 169-198.

Hildreth, W. & Fierstein, J. (2012). The Novarupta-Katmai eruption of 1912—largest eruption of the twentieth century: centennial perspectives. *U. S. Geological Survey Professional Paper* **1791**, 1-259.

Hildreth, W. & Wilson, C. J. N. (2007). Compositional zoning of the Bishop Tuff. *Journal of Petrology* **48**, 951-999.

Hildreth, W., Christiansen, R. L. & O'Neill, J. R. (1984). Catastrophic isotopic modification of rhyolitic magma at times of caldera subsidence Yellowstone Plateau volcanic field. *Journal of Geophysical Research* **90**, 8339-8369.

Hildreth, W., Halliday, A. N. & Christiansen, R. L. (1991). Isotopic and chemical evidence concerning the genesis and contamination of basaltic and rhyolitic magma beneath the Yellowstone Plateau volcanic field. *Journal of Petrology* **32**, 63-138.

Hildreth, W., Fierstein, J. & Calvert, A. (2017). Early post-caldera rhyolite and structural resurgence at Long Valley caldera, California. *Journal of Volcanology and Geothermal Research* **335**, 1-34.

Hosaka, M., Miyata, T. & Sunagawa, I. (1995). Growth and morphology of quartz crystals synthesized above the transition temperature. *Journal of Crystal Growth* **152**, 300-306.

Houghton, B. F., Wilson, C. J. N., McWilliams, M. O., Lanphere, M. A., Weaver, S. D., Briggs, R. M. & Pringle, M. S. (1995). Chronology and dynamics of a large silicic magmatic system: central Taupo Volcanic Zone, New Zealand. *Geology* **23**, 13-16.

Hu, Z., Zhang, W., Liu, Y., Chen, H., Gasching, R. M., Zong, K., Li, M., Gao, G. & Hu, S. (2013). Rapid bulk rock decomposition by ammonium fluoride (NH_4F) in open vessels at an elevated digestion temperature. *Chemical Geology* **355**, 144-152.

Huang, H.-H., Lin, F.-C., Schmandt, B., Farrell, J., Smith, R. B. & Tsai, V. C. (2015). The Yellowstone magmatic system from the mantle plume to the upper crust. *Science* **348**, 773-776.

Huber, C., Bachmann, O. & Dufek, J. (2011). Thermo-mechanical reactivation of locked crystal mushes: melting induced internal fracturing and assimilation processes in magmas. *Earth and Planetary Science Letters* **304**, 443-454.

Huber, C., Bachmann, O. & Dufek, J. (2012) Crystal-poor versus crystal-rich ignimbrites: a competition between stirring and reactivation. Geology **40**, 115-118

Humphreys, M. C. S., Kearns, S. L. & Blundy, J. D. (2006). SIMS investigation of electron-beam damage to hydrous rhyolitic glasses: implications for melt inclusion analysis. *American Mineralogist* **91**, 667-679.

James, D. E., Fouch, M. J., Carlson, R. W. & Roth, J. B. (2011). Slab fragmentation, edge flow and the origin of the Yellowstone hotspot track. *Earth and Planetary Science Letters* **311**, 124-135.

Jellinek, A. M. & DePaolo, D. J. (2003). A model for the origin of large silicic magma chambers: precursors of caldera-forming eruptions. *Bulletin of Volcanology* **65**, 363-381.

Laporte, D. & Provost, A. (1994). The equilibrium crystal shape of silicates: implications for the grain-scale distribution of partial melts. *EOS, Transactions of the American Geophysical Union* **75**, 364.

Le Bas, M. J. & Streckeisen, A. L. (1991). The IUGS systematics of igneous rocks. *Journal of the Geological Society, London* **148**, 825-833.

Leeman, W. P., Vitaliano, C. J. & Prinz, M. (1976). Evolved lavas from the Snake River Plain: Craters of the Moon National Monument, Idaho. *Contributions to Mineralogy and Petrology* **56**, 35-60.

Leeman, W. P., Menzies, M. A., Matty, D. J. & Embree, G. F. (1985). Strontium, neodymium and lead isotopic compositions of deep crustal xenoliths from the Snake River Plain: evidence for Archean basement. *Earth and Planetary Science Letters* **75**, 354-368.

Lipman, P. W. & Bachmann, O. (2015). Ignimbrites to batholiths: integrating perspectives from geological, geophysical, and geochronological data. *Geosphere* **11**, 705-743.

Loewen, M. W. & Bindeman, I. N. (2015). Oxygen isotope and trace element evidence for three-stage petrogenesis of the youngest episode (260-79 ka) of Yellowstone rhyolitic volcanism. *Contributions to Mineralogy and Petrology* **170**, 39.

Loewen, M. W. & Bindeman, I. N. (2016). Oxygen isotope thermometry reveals high magmatic temperatures and short residence times in Yellowstone and other hot-dry rhyolites compared to cold-wet systems. *American Mineralogist* **101**, 1222-1227.

Loewen, M. W. & Kent, A. J. R. (2012). Sources of elemental fractionation and uncertainty during the analysis of semi-volatile metals in silicate glasses using LA-ICP-MS. *Journal of Analytical Atomic Spectrometry* **27**, 1502-1508.

Lowenstern, J. B. & Hurwitz, S. (2008). Monitoring a supervolcano in repose: heat and volatile flux at the Yellowstone caldera. *Elements* **4**, 35-40.

Lowenstern, J. B., Smith, R. B. & Hill, D. P. (2006). Monitoring super-volcanoes: geophysical and geochemical signals at Yellowstone and other large caldera systems. *Philosophical Transactions of the Royal Society of London A***364**, 2055-2072.

Lowenstern, J. B., Evans, W. C., Bergfeld, D. & Hunt, A. G. (2014). Prodigious degassing of a billion years of accumulated radiogenic helium at Yellowstone. *Nature* **506**, 355-358.

Ludwig, K. R. (2008). Isoplot/Ex version 3.7. A geochronological toolkit for Microsoft Excel. *Berkeley Geochronological Center, Special Publication* **4**.

Macdonald, R. & Belkin, H. E. (2002). Compositional variation in minerals of the chevkinite group. *Mineralogical Magazine* **66**, 1075-1098.

Manley, C. R. (1996). Morphology and maturation of melt inclusions in quartz phenocrysts from the Badlands rhyolite lava flow, southwestern Idaho. *American Mineralogist* **81**, 158-168.

Mason, B. G., Pyle, D. M. & Oppenheimer, C. (2004). The size and frequency of the largest explosive eruptions on Earth. *Bulletin of Volcanology* **66**, 735-748.

McCurry, M. & Rodgers, D. W. (2009). Mass transfer along the Yellowstone hotspot track I: petrologic constraints on the volume of mantle-derived magma. *Journal of Volcanology and Geothermal Research* **188**, 86-98.

McCurry, M., Hayden, K. P., Morse, L. H. & Mertzman, S. (2008). Genesis of post-hotspot A-type rhyolite of the Eastern Snake River Plain volcanic field by extreme fractional crystallization of olivine tholeiite. *Bulletin of Volcanology* **70**, 361-383.

McDonough, W. F. & Sun, S.-s. (1995). The composition of the Earth. *Chemical Geology* 120, 223-253.

Meen, J. K. & Eggler, D. H. (1989). Chemical and isotopic compositions of Absaroka granitoids, southwestern Montana. *Contributions to Mineralogy and Petrology* **102**, 462-477.

Myers, M. L., Wallace, P. J., Wilson, C. J. N., Morter, B. K. & Swallow, E. J. (2016). Prolonged ascent and episodic venting of discrete magma batches at the onset of the Huckleberry Ridge supereruption, Yellowstone. *Earth and Planetary Science Letters* **451**, 285-297.

Nash, B. P., Perkins, M. E., Christensen, J. N., Lee, D.-C. & Halliday, A. N. (2006). The Yellowstone hotpot in space and time: Nd and Hf isotopes in silicic magmas. *Earth and Planetary Science Letters* **247**, 143-156.

Olin, P. H. & Wolff, J. A. (2010). Rare earth and high field strength element partitioning between iron-rich clinopyroxenes and felsic liquids. *Contributions to Mineralogy and Petrology* **160**, 761-775.

Pamukcu, A. S., Gualda, G. A. R., Bégué, F. & Gravley, D. M. (2015). Melt inclusion shapes: timekeepers of short-lived giant magma bodies. *Geology* 43, 947-950.

Parmigiani, A., Huber, C. & Bachmann, O. (2014). Mush microphysics and the reactivation of crystal-rich magma reservoirs. *Journal of Geophysical Research: Solid Earth* **119**, 6308-6322.

Parsons, I. (1978). Feldspars and fluids in cooling plutons. *Mineralogical Magazine* **42**, 1-17.

Perkins, M. E., Nash, W. P., Brown, F. H. & Fleck, R. J. (1995). Fallout tuffs of Trapper Creek, Idaho-a record of Miocene explosive volcanism in the Snake River Plain volcanic province. *Geological Society of America Bulletin* **107**, 1484-1506.

Pierce, K. L. & Morgan, L. A. (1992). The track of the Yellowstone hot spot: volcanism, faulting, and uplift. In: Link, P. K., Kuntz, M. A. & Platt, L. B. (eds) *Regional Geology of Eastern Idaho and Western Wyoming*. *Geological Society of America Memoirs* **179**, 1-53.

Pierce, K. L. & Morgan, L. A. (2009) Is the track of the Yellowstone hotspot driven by a deep mantle plume? — Review of volcanism, faulting, and uplift in light of new data. *Journal of Volcanology and Geothermal Research* **188**, 1-25.

Pin, C., Gannoun, A. & Dupont, A. (2014). Rapid simultaneous separation of Sr, Pb and Nd by extraction chromatography prior to isotope ratios determination by TIMS and MC-ICP-MS. *Journal of Analytical Atomic Spectrometry* **29**, 1858-1870.

Pistolesi, M., Isaia, R., Marianelli, P., Bertagnini, A., Fourmentraux, C., Albert, P. G., Tomlinson, E. L., Menzies, M. A., Rosi, M. & Sbrana, A. (2016). Simultaneous eruptions from multiple vents at Campi Flegrei (Italy) highlight new eruption processes at calderas. *Geology* **44**, 487-490.

Poldervaart, A. & Hess, H. H. (1951). Pyroxenes in the crystallization of basaltic magma. *Journal of Geology* **59**, 472-489.

Potter, K. E., Shervais, J. W., Christiansen, E. H. & Vetter, S. K. (2018). Evidence for cyclical fractional crystallization, recharge, and assimilation in basalts of the Kimama drill core, central Snake River Plain, Idaho: 5.5-million-years of petrogenesis in a mid-crustal sill complex. *Frontiers in Earth Science* **6**, 10.

Pritchard, C. J., Larson, P. B., Spell, T. L. & Tarbert, K. D. (2013). Eruption-triggered mixing of extra-caldera basalt and rhyolite complexes along the East Gallatin-Washburn fault zone, Yellowstone National Park, WY, USA. *Lithos* **175-176**, 163-177.

Putirka, K. D. (2008). Thermometers and barometers for volcanic systems. *Reviews in Mineralogy and Geochemistry* **69**, 61-120.

Putirka, K. D., Kuntz, M. A., Unruh, D. M. & Vaid, N. (2009). Magma evolution and ascent at the Craters of the Moon and neighboring volcanic fields, southern Idaho, USA: implications for the evolution of polygenetic and monogenetic volcanic fields. *Journal of Petrology* **50**, 1639-1665.

Ramsey, M. H., Potts, P. J., Webb, P. C., Watkins, P., Watson, J. S. & Coles, B. J. (1995). An objective assessment of analytical method precision: comparison of ICP-AES and XRF for the analysis of silicate rocks. *Chemical Geology* **124**, 1-19.

Reid, M. R. (2008). How long does it take to supersize an eruption? *Elements* **4**, 23-28.

Reubi, O. & Blundy, J. (2008). Assimilation of plutonic roots, formation of high-K 'exotic' melt inclusions and genesis of andesitic magmas at Volcán de Colima, Mexico. *Journal of Petrology* **49**, 2221-2243.

Reynolds, R. L. (1977). Paleomagnetism of welded tuffs of the Yellowstone group. *Journal of Geophysical Research* **82**, 3677-3693.

Rivera, T. A., Schmitz, M. D., Crowley, J. L. & Storey, M. (2014). Rapid magma evolution constrained by zircon petrochronology and $^{40}Ar/^{39}Ar$ sanidine ages for the Huckleberry Ridge Tuff, Yellowstone, USA. *Geology* **42**, 643-646.

Rivera, T. A., Schmitz, M. D., Jicha, B. R. & Crowley, J. L. (2016). Zircon petrochronology and $^{40}Ar/^{39}Ar$ sanidine dates for the Mesa Falls Tuff: crystal-scale records of magmatic evolution and the short lifespan of a large Yellowstone magma chamber. *Journal of Petrology* **57**, 1677-1704.

Rivera, T. A., Furlong, R., Vincent, J., Gardiner, S., Jicha, B. R., Schmitz, M. D. & Lippert, P. C. (2018). Volcanism at 1.45 Ma within the Yellowstone volcanic field, United States. *Journal of Volcanology and Geothermal Research* **357**, 224-238.

Roberge, J., Wallace, P. J. & Kent, A. J. R. (2013). Magmatic processes in the Bishop Tuff rhyolitic magma based on trace elements in melt inclusions and pumice matrix glass. *Contributions to Mineralogy and Petrology* **165**, 237-257.

Rosman, K. J. R. & Taylor, P. D. P. (1998). Isotopic compositions of the elements 1997. *Pure and Applied Chemistry* **70**, 217-235.

Sampson, D. E. & Cameron, K. L. (1987). The geochemistry of the Inyo volcanic chain: multiple magma systems in the Long Valley region, eastern California. *Journal of Geophysical Research* **92**, 10403-10421.

Self, S. (2006). The effects and consequences of very large explosive volcanic eruptions. *Philosophical Transactions of the Royal Society of London A***364**, 2073-2097.

Shane, P., Martin, S. B., Smith, V. C., Beggs, K. F., Darragh, M. B., Cole, J. W. & Nairn, I. A. (2007). Multiple rhyolite magmas and basalt injection in the 17.7 ka Rerewhakaaitu eruption episode from Tarawera volcanic complex, New Zealand. *Journal of Volcanology and Geothermal Research* **164**, 1-26.

Shane, P., Nairn, I. A., Smith, V. C., Darragh, M., Beggs, K. & Cole, J. W. (2008). Silicic recharge of multiple rhyolite magmas by basaltic intrusion during the 22.6 ka Okareka eruption episode, New Zealand. *Lithos* **103**, 527-549.

Singer, B. S., Jicha, B. R., Condon, D. J., Macho, A. S., Hoffman, K. A., Dierkhising, J., Brown, M. C., Feinberg, J. M. & Kidane, T. (2014). Precise ages of the Réunion event and Huckleberry Ridge excursion: episodic clustering of geomagnetic instabilities and the dynamics of flow within the outer core. *Earth and Planetary Science Letters* **405**, 25-38.

Smith, R. B., Jordan, M., Steinberger, B., Puskas, C. M., Farrell, J., Waite, G. P., Husen, S., Chang, W.-L. & O'Connell, R. (2009). Geodynamics of the Yellowstone hotspot and mantle plume: seismic and GPS imaging, kinematics and mantle flow. *Journal of Volcanology and Geothermal Research* **188**, 26-56.

Smith, R. L. (1979). Ash-flow magmatism. In: Chapin, C. E. & Elston. W. E. (Eds) *Ash-Flow Tuffs*. *Geological Society of America Special Papers* **180**, 5-27.

Sparks, R. S. J., Sigurdsson, H. & Wilson, L. (1977). Magma mixing: a mechanism for triggering acid explosive eruptions. *Nature* **267**, 315-318.

Sparks, R. S. J., Self, S., Grattan, J., Oppenheimer, C., Pyle, D. & Rymer, H. (2005). *Super-eruptions: Global Effects and Future Threats*. *Report of the Geological Society of London Working Group*. London, The Geological Society, 24 pp

Stelten, M. E., Cooper, K. M., Vazquez, J. A., Calvert, A. T. & Glessner, J. G. (2015). Mechanisms and timescales of generating eruptible rhyolitic magmas at Yellowstone caldera from zircon and sanidine geochronology and geochemistry. *Journal of Petrology* **56**, 1607-1642.

Stelten, M. E., Cooper, K. M., Wimpenny, J. B., Vazquez, J. A. & Zin, Q.-Z. (2017). The role of mantle-derived magmas in the isotopic evolution of Yellowstone's magmatic system. *Geochemistry, Geophysics, Geosystems* **18**, 1350-1365.

Stelten, M. E., Champion, D. E. & Kuntz, M. A. (2018). The timing and origin of pre- and post-caldera volcanism associated with the Mesa Falls Tuff, Yellowstone Plateau volcanic field. *Journal of Volcanology and Geothermal Research* **350**, 47-60.

Streck, M. J. (2014). Evaluation of crystal mush extraction models to explain crystal-poor rhyolites. *Journal of Volcanology and Geothermal Research* **284**, 79-94.

Streck, M. J. & Grunder, A. L. (1997). Compositional gradients and gaps in high-silica rhyolites of the Rattlesnake Tuff, Oregon. *Journal of Petrology* **38**, 133-163.

Streck, M. J. & Grunder, A. L. (1999) Enrichment of basalt and mixing of dacite in the rootzone of a large rhyolitic chamber: inclusions and pumices from the Rattlesnake Tuff, Oregon. *Contributions to Mineralogy and Petrology* **136**, 193-212.

Swallow, E. J., Wilson, C. J. N., Myers, M. L., Wallace, P. J., Collins, K. S. & Smith, E. G. C. (2018a). Evacuation of multiple magma bodies and the onset of caldera collapse in a supereruption, captured in glass and mineral compositions. *Contributions to Mineralogy and Petrology* **173**, 33.

Swallow, E. J., Wilson, C. J. N., Charlier, B. L. A. & Gamble, J. A. (2018b). Mafic inputs into the rhyolitic magma system of the 2.08 Ma Huckleberry Ridge eruption, Yellowstone. *American Mineralogist* **103**, 757-775.

Swanson, S. E. & Fenn, P. M. (1986). Quartz crystallization in igneous rocks. *American Mineralogist* **71**, 331-342.

Szymanowski, D., Ellis, B. S., Bachmann, O., Guillong, M. & Phillips, W. M. (2015). Bridging basalts and rhyolites in the Yellowstone-Snake River Plain volcanic province: the elusive intermediate step. *Earth and Planetary Science Letters* **415**, 80-89.

Thirlwall, M. F. (1991). Long-term reproducibility of multicollector Sr and Nd isotope ratio analysis. *Chemical Geology* **94**, 85-104.

Thirlwall, M. F. (2000) Inter-laboratory and other errors in Pb isotope analyses investigated using a ^{207}Pb-^{204}Pb double spike. *Chemical Geology* **163**, 299-322.

Thompson, R. N. (1975). Primary basalts and magma genesis II. Snake River Plain, Idaho, USA. *Contributions to Mineralogy and Petrology* **52**, 213-232.

Till, C. B., Vazquez, J. A. & Boyce, J. W. (2015). Months between rejuvenation and volcanic eruption at Yellowstone caldera, Wyoming. *Geology* **43**, 695-698.

Todt, W., Cliff, R. A., Hanser, A. & Hofmann, A. W. (1996). Evaluation of a ^{202}Pb-^{205}Pb double spike for high-precision lead isotope analysis. In: Basu, A. & Hart, S. (eds) *Earth*

Processes: Reading the Isotopic Code. *American Geophysical Union, Geophysical Monograph* **95**, 429-437.

Tramontano, S., Gualda, G. A. R. & Ghiorso, M. S. (2017). Internal triggering of volcanic eruptions: tracking overpressure regimes for giant magma bodies. *Earth and Planetary Science Letters* **472**, 142-151.

Troch, J., Ellis, B. S., Mark, D. F., Bindeman, I. N., Kent, A. J. R., Guillong, M. & Bachmann, O. (2017). Rhyolite generation prior to a supereruption: insights from the Island Park-Mount Jackson rhyolite series. *Journal of Petrology* **58**, 29-52.

Troch, J., Ellis, B. S., Harris, C., Ulmer, P. & Bachmann, O. (2018). The effect of prior hydrothermal alteration on the melting behaviour during rhyolite formation in Yellowstone, and its importance in the generation of low-$\delta^{18}O$ magmas. *Earth and Planetary Science Letters* **481**, 338-349.

Wallace, P. J., Anderson, A. T. & Davis, A. M. (1999). Gradients in H_2O, CO_2 and exsolved gas in a large-volume silicic magma system: interpreting the record preserved in melt inclusions from the Bishop Tuff. *Journal of Geophysical Research* **104**, 20097-20122.

Wark, D. A. & Miller, C. F. (Eds) (2008). Supervolcanoes. *Elements* **4**, 11-49.

Wark, D. A., Hildreth, W., Spear, F. S., Cherniak, D. J. & Watson, E. B. (2007). Pre-eruption recharge of the Bishop magma system. *Geology* **35**, 235-238.

Waters, L. E. & Lange, R. A. (2015). An updated calibration of the plagioclase-liquid hygrometer-thermometer applicable to basalts through rhyolites. *American Mineralogist* **100**, 2172-2184.

Watson, E. B. & Harrison, T. M. (1983). Zircon saturation revisited: temperature and composition effects in a variety of crustal magma types. *Earth and Planetary Science Letters* **64**, 295-304.

Watts, K. E., Bindeman, I. N. & Schmitt, A. K. (2012). Crystal scale anatomy of a dying supervolcano: an isotope and geochronology study of individual phenocrysts from voluminous rhyolites of the Yellowstone caldera. *Contributions to Mineralogy and Petrology* **164**, 45-67.

Westgate, J. A., Pearce, N. J. G., Perkins, W. T., Preece, S. J., Chesner, C. A. & Muhammad, R. F. (2013). Tephrochronology of the Toba Tuffs: four primary glass populations define the 75-ka Youngest Toba Tuff, northern Sumatra, Indonesia. *Journal of Quaternary Science* **28**, 772-776.

Whitaker, M. L., Nekvasil, H., Lindsley, D. H. & McCurry, M. (2008). Can crystallization of olivine tholeiite give rise to potassic rhyolites?—an experimental investigation. *Bulletin of Volcanology* **70**, 417-434.

Wilke, S., Holtz, F., Neave, D. A. & Almeev, R. (2017). The effect of anorthite and water on quartz-feldspar cotectic compositions in the rhyolitic system and implications for geobarometry. *Journal of Petrology* **58**, 789-818.

Wilke, S., Holtz, F., Li, X., Neave, D. A. & Almeev, R. R. (2019). Rhyolite-MELTS vs DERP – Reply to comment by Gualda *et al*. on 'The effect of anorthite content and water on quartz-feldspar cotectic compositions in the rhyolitic system and implications for geobarometry' by Wilke *et al*. (2017), Journal of Petrology, 58, No. 4, 789-818. *Journal of Petrology* (in press: doi: 10.1093/petrology/egz002).

Wilson, C. J. N. (1993). Stratigraphy, chronology, styles and dynamics of late Quaternary eruptions from Taupo volcano, New Zealand. *Philosophical Transactions of the Royal Society of London A* **343**, 205-306.

Wilson, C. J. N. (2009). Physical volcanology of the Huckleberry Ridge Tuff. *EOS, Transactions of the American Geophysical Union* **90**, Fall Meeting Supplement Abstract V23C-2085.

Wilson, C. J. N. & Charlier, B. L. A. (2009). Rapid rates of magma generation at contemporaneous magma systems, Taupo volcano, New Zealand: insights from U-Th model-age spectra in zircons. *Journal of Petrology* **50**, 875-907.

Wilson, C. J. N., Blake, S., Charlier, B. L. A. & Sutton, A. N. (2006). The 26.5 ka Oruanui eruption, Taupo volcano, New Zealand: development characteristics and evacuation of a large rhyolitic magma body. *Journal of Petrology* **47**, 35-69.

Wilson, C. J. N., Gravley, D. M., Leonard, G. S. & Rowland, J. V. (2009). Volcanism in the central Taupo Volcanic Zone, New Zealand: tempo, styles and controls. In: Thordarson, T., Self, S., Larsen, G., Rowland, S. K. & Hoskuldsson, A. (eds) *Studies in Volcanology: The Legacy of George Walker*. *Special Publications of IAVCEI* **2**, 225-247.

Wilson, C. J. N., Stelten, M. E. & Lowenstern, J. B. (2018). Contrasting perspectives on the Lava Creek Tuff eruption, Yellowstone, from new U-Pb and $^{40}Ar/^{39}Ar$ age determinations. *Bulletin of Volcanology* **80**, 53.

Wolff, J. A. (2017). On the syenite-trachyte problem. *Geology* **45**, 1067-1070.

Wolff, J. A. & Ramos, F. C. (2014). Processes in caldera-forming high-silica rhyolite magma: Rb-Sr and Pb isotope systematics of the Otowi member of the Bandelier Tuff, Valles caldera, New Mexico, USA. *Journal of Petrology* **55**, 345-375.

Wolff, J. A., Ellis, B. S., Ramos, F. C., Starkel, W. A., Boroughs, S., Olin, P. H. & Bachmann, O. (2015). Remelting of cumulates as a process for producing chemical zoning in silicic tuffs: a comparison of cool, wet and hot, dry rhyolitic magma systems. *Lithos* **236-237**, 275-286.

Wooden, J. L. & Mueller, P. A. (1988). Pb, Sr, and Nd isotopic compositions of a suite of Late Archean, igneous rocks, eastern Beartooth Mountains: implications for crust-mantle evolution. *Earth and Planetary Science Letters* **87**, 59-72.

Wotzlaw, J.-F., Bindeman, I. N., Stern, R. A., D'Abzac, F.-X. & Schaltegger, U. (2015). Rapid heterogeneous assembly of multiple magma reservoirs prior to Yellowstone supereruptions. *Scientific Reports* **5**, 14026.

Zhou, Q., Liu, L. & Hu, J. (2018). Western US volcanism due to intruding oceanic mantle driven by ancient Farallon slabs. *Nature Geoscience* **11**, 70-76.

FIGURE CAPTIONS

Fig. 1 Simplified geological map of the Yellowstone Plateau volcanic field, adapted from Christiansen (2001) and Christiansen *et al*. (2007). Outcrop areas of the HRT are shown in red and key sampling localities for this study are numbered.

Fig. 2 Schematic diagram of the stratigraphy of the HRT and estimates for intra-eruption timescales based on fieldwork by C. J. N. Wilson (Wilson, 2009 and Wilson *et al*., in prep.). Initial fall deposits were episodic, with short time breaks indicated by reworking and fine ash tops to individual horizons (Myers *et al*., 2016; Swallow *et al*., 2018a). A cessation in activity of weeks to months between members B and C is inferred from welding breaks, and rheomorphic deformation of member A but not B (see Supplementary Data Fig. S1). A years to decades time break between members B and C is estimated from cooling breaks indicated by welding intensities, but also the presence of vapour-phase alteration of pre-C fall deposits or the base of member C ignimbrite where it rests directly on the top of ignimbrite member B (Fig. S1).

Fig. 3 Schematic flow chart to show the logic structure underlying the data presentation in this paper. The sampled felsic materials are labelled on field criteria into the nine *clast types* (see Table 1 for descriptions), then grouped on geochemical and mineralogical grounds into the seven *compositional suites* and then, when coupled with isotopic data, allocated to four *magmatic systems*. The felsic and mafic components combined contribute to the overall magmatic complex that fed the Huckleberry Ridge Tuff (HRT) eruption.

Fig. 4 Photographs showing representative of clast types sampled for this study. (a), (b) two examples of typical crystal-rich type J1 clasts (see Table 1) from member B at locality 65 (Fig. 1: YP028: 74.36 wt % SiO_2; YP085: 75.23 wt % SiO_2: Supplementary Data Electronic Appendix 3). Note the large crystal sizes and presence of glomerocrysts. (c) Type J2 clast YP251 (75.01 wt % SiO_2) from member A, exhibiting a characteristic crystal-rich, dense texture with darkened groundmass glass. (d) Type J3 clast (not sampled) from member A showing coarse, intact euhedral feldspars within dark groundmass glass. (e) Type J4 mingled pumice from upper member B at locality 65 (Fig. 1). The scoria component was analysed as YP083SCORIA (55.56 wt % SiO_2: data presented in

Swallow *et al*., 2018b, and in Supplementary Data Electronic Appendix 3). (f) Outcrop photograph of characteristically non-vesicular, crystal-poor and devitrified type J5 clasts within member C ignimbrite from the Red Mountains. (g) Crystal-poor type J7 pumice (YP134: 76.61 wt % SiO_2) from locality 332 (Fig. 1) in member C. Note the characteristic small crystal sizes, and the pink-oxidised rinds. (f) Examples of type J8 pumices from locality 057 (Fig. 1). Although uniformly crystal-poor to -moderate, and highly to extremely vesicular, note the wide variations in vesicle texture reflected in the colour variations.

Fig. 5 Total alkalis-silica plot for samples analysed in this study for the entire HRT (and relevant regional mafic eruptives) and individual members. All major-element data plotted here represent values plotted on a volatile-free basis to total 100%. Symbol shapes relate to the host ignimbrite member from which the clast was sampled. Symbol colours denote the clast type (see Table 1 for details). Silicic suites (A1, B1 etc.) are those defined from compositional groupings (see text for details). Mafic suites 1-3 were defined in Swallow *et al*. (2018b) and labelled as M1-M3 here for clarity. For the mafic materials, new data presented in this study are shown in larger symbols; data from Swallow *et al*. (2018b) in smaller symbols. For the full data set presented in these and other bivariate plots, see Supplementary Data Electronic Appendix 3. Classification fields from Le Bas & Streckeisen (1991). Analytical 2s.d. precisions are smaller than the symbol size.

Fig. 6 Al_2O_3 *versus* SiO_2 for samples analysed in this study for the whole HRT, individual members and relevant regional mafic eruptives (the latter from Swallow *et al*., 2018b). Analytical 2 s.d. precisions are smaller than the symbol size. Other information as in Fig. 5. Full data set in Supplementary Data Electronic Appendix 3.

Fig. 7 P_2O_5 *versus* SiO_2 for samples analysed in this study for the whole HRT, individual members and relevant regional mafic eruptives (the latter from Swallow *et al*., 2018b). Analytical 2 s.d. precisions are smaller than the symbol size. Other information as in Fig. 5. Full data set in Supplementary Data Electronic Appendix 3.

Fig. 8 Ba (by XRF techniques) *versus* SiO_2 for samples analysed in this study for the whole HRT, individual members and relevant regional mafic eruptives (the latter from Swallow *et al*., 2018b). Analytical 2 s.d. precisions are smaller than the

symbol size. Other information as in Fig. 5. Full data set in Suplementary Data Electronic Appendix 3.

Fig. 9 Sr *versus* SiO_2 for samples analysed in this study for the whole HRT, individual members and relevant regional mafic eruptives (the latter from Swallow *et al*., 2018b). Analytical 2 s.d. precisions are smaller than the symbol size. Other information as in Fig. 5. Full data set in Supplementary Data Electronic Appendix 3.

Fig. 10 Nb *versus* SiO_2 for samples analysed in this study for the whole HRT, individual members and relevant regional mafic eruptives (the latter from Swallow *et al*., 2018b). Analytical 2 s.d. precisions are smaller than the symbol size. Other information as in Fig. 5. Full data set in Supplementary Data Electronic Appendix 3.

Fig. 11 Sc *versus* SiO_2 for samples analysed in this study for the whole HRT, individual members and relevant regional mafic eruptives (the latter from Swallow *et al*., 2018b). Analytical 2 s.d. precisions are smaller than the symbol size. Other information as in Fig. 5. Full data set in Supplementary Data Electronic Appendix 3.

Fig. 12 C1 chondrite-normalised rare earth-element (REE) plots for samples from members A, B and C of the HRT. Compositional fields (grey and pink shaded regions) of mafic suites M1-M3 are from Swallow *et al*. (2018b), plus new data from this study (see Supplementary Data Electronic Appendix 3). Normalising values from McDonough & Sun (1995).

Fig. 13 $^{87}Sr/^{86}Sr$ *versus* $^{143}Nd/^{144}Nd$ (where $^{87}Sr/^{86}Sr$ is age-corrected to an eruption age of 2.08 Ma) for samples from the HRT and relevant regional mafic eruptives. Field of Archean crust from McCurry & Rogers (2009). ε_{Nd} calculated from DePaolo & Wasserburg (1976: see text for details). Individual 2 s.e. analytical uncertainties are smaller than symbol size unless shown. Full data set in Supplementary Data Electronic Appendix 3.

Fig. 14 $^{87}Sr/^{86}Sr$ *versus* indices of evolution for samples from the HRT and relevant regional eruptives. See Fig. 5 for symbol and suite details. Individual 2 s.e. analytical uncertainties are smaller than symbol size unless shown. Full data set in Supplementary Data Electronic Appendix 3.

Fig. 15 Pb isotopic compositions for samples from the HRT and relevant regional eruptives. Insets show enlarged fields of data from all suites from members A and B plus suite C3. Individual 2 s.e. analytical uncertainties are smaller than symbol size unless shown. Full data set in Supplementary Data Electronic Appendix 3.

Fig. 16 Ba *versus* La concentrations of groundmass glasses from pumice from members A, B and C of the HRT. Large crosses show the means of each compositional cluster in the fall deposit (fall glass cluster FGC; obsidian [pyroclast] cluster: OGC) and basal ignimbrite (ignimbrite glass cluster: IGC; from Swallow *et al*., 2018a). Black crosses in member A plot represent 2 s.d. analytical uncertainties at the plotted concentrations (400, 50 and 50, 120 ppm for Ba and La, respectively) derived through error slope regression (from Swallow *et al*., 2018a). Full data set in Supplementary Data Electronic Appendix 4.

Fig. 17 Sr/Rb *versus* Ba/Rb for groundmass glasses from pumice from members A, B and C of the HRT. Large crosses show the means of each compositional cluster in the fall deposit (fall glass cluster FGC; obsidian [pyroclast] cluster: OGC) and basal ignimbrite (ignimbrite glass cluster: IGC: from Swallow *et al*., 2018a). Black crosses in member A plot represent 2 s.d. analytical uncertainties at the plotted concentration derived through error slope regression (as in Swallow *et al*., 2018a). Full data set in Supplementary Data Electronic Appendix 4.

Fig. 18 Ternary diagrams showing feldspar compositions for crystals from members A, B and C of the HRT. (a): All analyses from members A and B samples. (b): All analyses from member C samples. Details of clast types are in Table 1. Compositional fields are labelled with the classification of Deer *et al*. (1966).

Fig. 19 Mol% Cn versus Or contents of sanidine rim compositions (including overgrowths) in samples from HRT members A, B and C. Compositional fields of interior zones (cores and intermediate zones) are shown for comparison. Histogram bin widths are 0.1 mol% Cn and red lines are pdf curves derived from Isoplot (Ludwig, 2008) using a 2 s.d. error of ±0.3 mol% Cn. Cross in the top right indicates 2 s.d. analytical precision. Full data set in Supplementary Data Electronic Appendix 5.

Fig. 20 Backscattered electron images of representative feldspar textures found in the HRT members and juvenile clast types (Table 1), annotated with compositional data from electron microprobe analyses (Supplementary Data Electronic Appendix 5). (a) Homogenous sanidine crystal from YP416 (member A, type J1),

typical of suite A3 and C3 sanidines. (b) Plagioclase and sanidine crystals from YP023 (member B, type J1) showing the contrast between homogeneous plagioclase (found in all suites) and zoned sanidines characteristic of suites A1 and B1. (c) Sanidines from YP191 (member A, type J3) showing textural diversity in suite A2 samples. High Ba rims on sanidines are present, as are homogenous crystals. (d) Ba-rich rim characteristic of sanidines from suite C2 (YP282, type J8). (e), (f) Anti-rapakivi feldspars present in suites A2 (YP191, type J3) and B1 (YP056, type J4), respectively, with a plagioclase interior and Ba-rich sanidine overgrowth. (g), (h) Bright, high-Ba rims found in suite B1 type J4 scoria-bearing pumices (YP056 and YP061, respectively). (i), (j) Carbonate-cemented sanidine (YP307: type J1) and plagioclase (YP414: type J1) crystals in member A. (k), (l) 'Plutonic-textured' feldspars present in type J4 (YP071: member B) and J8 clasts (YP282: member C) marked by feldspar intergrowths and dissolution textures (e.g. corroded cores).

Fig. 21 Pyroxene quadrilaterals for crystals from members A, B and C of the HRT. (a) All pyroxene analyses from members A and B. (b) Pyroxene rim compositions from member A and B samples. Compositional fields (grey shaded regions) copied across from panel (a) for comparison. (c) All pyroxene analyses from member C. (d) Pyroxene rim compositions from member C. Compositional fields (grey shaded regions) copied across from panel (c) for comparison. Compositional labels from Poldervaart & Hess (1951). Full data set in Supplementary Data Electronic Appendix 5.

Fig. 22 Backscattered electron images of representative ferromagnesian minerals and textures found in the HRT and compositional data from electron microprobe analyses (Supplementary Data Electronic Appendix 5). (a) Bright pigeonite core within a augite crystal from YP140 ('B in C' type J1 clast, suite B1). (b) Dark Mg-rich augite core within lighter Fe-rich augitic rim from YP414 (type J1, suite A1). (c) Zoned augite crystal from YP363 (type J1, suite A1) Adhering crystals are Fe-Ti oxides. (d) Altered olivine with bright, homogeneous unaltered regions and darker oxidised domains, commonly around rims and along fractures (YP562: type J9, suite C2). (e), (f) Zoned chevkinite crystals in YP255 (type J1, suite A3).

Fig. 23 Summary schematic diagram showing the broad eruptive timescale and stratigraphy of the HRT along with the four inferred silicic magmatic systems

(with their associated magmatic suites and mafic root zones) tapped during the eruption. See text for discussion. Colours based on symbol colours that distinguish the systems/suites in earlier figures.

Fig. 24 Flow chart showing the distinguishing features of each of the four HRT magmatic systems and their petrogenetic pathways. The overall characteristics of the silicic systems are controlled in turn by their parental mafic root zone, the degrees of interaction with crustal protoliths and preceding intrusions, and spatial relationship to the focus of mafic influx. See text for discussion. See also Swallow *et al*. (2018b) for background to the source regions for the mafic magma suites. Colours based on symbol colours that distinguish the systems/suites in earlier figures.

Fig. 25 Semi-quantitative diagram showing the behaviour of the HRT magmatic complex throughout the eruption sequence. (a) Multiple laterally-adjacent melt-dominant bodies tapped at the onset of eruption (initial fall deposits) and into widespread deposition of member A ignimbrite were recognised on the basis of glass and feldspar compositions to represent two magmatic lineages (Swallow *et al*., 2018a). (b) Member A ignimbrite compositions reflect the continued tapping of these multiple melt-dominant bodies, with the lineages recognised here to represent magmatic systems 1 and 2. A deeper, separate suite A2 body was also tapped during member A deposition. Influx of mafic material predominantly in the form of dense clasts (Swallow *et al*., 2018b). (c) During a time break of weeks to months, extensive mixing occurred between a renewed influx of mafic material of at least two lineages (erupted at the surface as scoria in upper member B ignimbrite) and magmatic system 1 material. Member B then evacuated magmatic system 1 but there was a cessation in evacuation of system 2. (d) During a time break of years to decades, magmatic system 2 was rejuvenated, forming a new melt-dominant body (suite C3). Coevally, melt-dominant bodies from two previously unerupted magmatic systems (3 and 4) formed. Member C evacuated melt-dominant bodies from systems 2, 3 and 4, but no material representing system 1 has been found. Colours and suite names as in Swallow *et al*. (2018a) and Fig. 5. See text and Table 4 for classification of the magmatic systems.

Fig. 26 Semi-quantitative diagram summarising the HRT magmatic complex from the upper mantle to the surface. Bracketed numbers indicate key processes, as

follows. (i) HRT mafic melts are generated from regions of the mantle enriched by high *P-T* fluids derived from the subducted Farallon slab. Early HRT mafic melts ascend through contemporaneously or previously (in late Cretaceous or Eocene times) hybridised crust (see Swallow *et al*., 2018b). (ii) Melts stall and crystallise in the middle crust to form protolith 1. (iii) Partial melts of protolith 1 ascend and become parental melts that differentiate to form the melt-dominant bodies of magmatic systems 1 and 2. (iv) Crystalline residuum associated with these fractionates forms protolith 2, which is remelted to form suite A2. (v) Suite M1 HRT mafic melts ascend through the crust and intersect and mix with magmatic system 1. Magmatic system 2 is located away from the focus of mafic influx. (vi) Spatially separated from magmatic systems 1 and 2, as well as within a region of un-modified Archean crust (Swallow *et al*., 2018b), melts from enriched (suite M1) and non-enriched (suite M2) source zones ascend from the uppermost mantle, stall in the middle crust, hybridise with surrounding Archean crust, crystallise and solidify. (vii) Partial melts of these hybridised cumulates ascend and feed magmatic systems 3 (suite C2) and 4 (suite C1). Crustal/mantle boundary depths from Huang *et al*. (2015).

ELECTRONIC MATERIALS

Supplementary Material: Further details of analytical methods, and Supplementary Figures referred to in the main text

Electronic Appendix 1: Sample listing and localities

Electronic Appendix 2: Crystal contents in juvenile clasts

Electronic Appendix 3: Major elements, trace elements and isotopes

Electronic Appendix 4: Glass analytical data

Electronic Appendix 5: Mineral analytical data

Table 1: Descriptions of silicic clast types in the HRT and their characteristic petrographic features

Clast type	Members where clasts sampled	Physical characteristics	Geochemical suite(s)
J1	A and B (C as surficial pick-ups)	• Pumices: white, brown where oxidised (Fig. S2a) • Moderately to highly vesicular (rounded to elongate vesicles) • Fibrous, common schlieren and 'adobe-type' textures • Coarse crystals (up to 8 mm), crystal-rich (11-20 wt%), common glomerocrysts • Flattened, devitrified fiamme equivalents also sampled	A1, A3, B1
J2	A and B	• Dense, poorly vesicular • Dark grey-black through microlite growth (Fig. S2b) • Coarse crystals (up to 8mm), crystal rich (27-35 wt%)	A1, B1
J3	A and B	• Black to dark brown (Fig. S2c) • Moderately to poorly vesicular • 10-20% euhedral feldspars up to 10 mm	A2, B1
J4	B (upper) and C (pickups)	• Mingled, scoria-bearing rhyolitic clasts (Fig. S2a) • Cm-scale lenses of scoria within pumices similar to J1-type • Sparse incorporation of J3-type material	B1
J5	C	• Black, devitrified material (Fig. S2d) • Non-vesicular • Angular rigid to flattened, fluidal fiamme or rounded clasts • Equant (welded) to elongate (rheomorphic ignimbrite) • Small crystals (<3 mm) and crystal poor (<15%); feldspar and rare quartz	C1, C2
J6	C (Red Mountains)	• Visually identical to J5-type clasts • Minor intrusions into hot, still-plastic member C ignimbrite	C1
J7	C (Teton River: loc. 332, Fig. 1)	• Rounded pumices with equant vesicles (Fig. S2e) • Small crystals (<3 mm), crystal poor-moderate (11-15 wt%)	C3
J8	C (Bitch Creek: loc. 057, Fig. 1)	• Dark brown-grey, mid-grey or pale buff pumices (Fig. S2f), sometimes colour-mingled • Elongate to platey in shape • Moderately vesicular with sub-100 μm bubbles to extremely vesicular, coarsely cellular to fibrous with 1-10 mm bubbles • Small crystals (<3 mm) and crystal poor-moderate (7-11 wt%)	C2
J9	C (Red Mountains and Huckleberry Mountain)	• Pale-coloured yellow to grey devitrified fiamme • Sometimes vuggy appearance • Occasionally micro- to macro-spherulitic • Similar crystal sizes and abundance to J8-type pumices	C2

Table 2: Representative major and trace element data for juvenile materials in the Huckleberry Ridge Tuff

Sample	YP114	YP459	YP251	YP191	YP255	YP078	YP061	YP266	YP139	YP271	YP504	YP611
Locality	263	397	397	99	397	65	65	64	332	332	502	509
Host unit	(A)	(A)	(A)	(A)	(A)	(B)	(B)	(B)	(B in C)	(B in C)	(C)	(C)
Clast type	J1	J1	J2	J3	J1	J1	J4	J4	J1	J1	J5	J5
Suite	A1	A1	A1	A2	A3	B1	B1	B1	B1	B1	C1	C1
MS	1	1	1	1	2	1	1	1	1	1	4	4
SiO_2	72.98	77.30	75.01	69.87	77.00	76.27	71.43	73.74	77.07	76.44	75.94	72.21
TiO_2	0.26	0.12	0.17	0.47	0.11	0.14	0.33	0.27	0.13	0.11	0.31	0.56
Al_2O_3	13.56	11.69	12.72	14.05	11.85	12.21	13.75	13.14	11.99	11.62	11.88	12.05
Fe_2O_3	2.96	1.59	2.14	4.87	1.58	1.85	3.88	3.02	1.66	1.58	3.59	6.79
MnO	0.05	0.03	0.05	0.11	0.03	0.04	0.09	0.06	0.03	0.03	0.05	0.07
MgO	0.08	0.07	0.05	0.24	0.08	0.09	0.15	0.13	0.03	0.19	0.05	0.09
CaO	0.82	0.70	0.80	1.65	0.61	0.74	1.49	1.21	0.70	1.93	0.72	1.40
Na_2O	4.05	2.86	3.58	3.68	2.89	3.39	3.68	3.06	3.26	3.11	3.52	2.99
K_2O	5.22	5.64	5.45	4.94	5.83	5.27	5.14	5.31	5.11	4.96	3.92	3.36
P_2O_5	0.04	0.02	0.03	0.11	0.02	0.02	0.05	0.05	0.02	0.02	0.02	0.10
Total	99.24	100.24	99.80	99.91	100.36	99.32	99.20	99.89	100.22	100.57	99.47	100.53
LOI	0.27	2.25	1.85	2.76	2.27	2.40	2.72	2.96	2.31	3.52	0.76	2.67
K/Na	1.44	2.21	1.71	1.50	2.26	1.74	1.56	1.94	1.75	1.79	1.25	1.26
Li	24	26	37	26	30	18.8	20	19	24	26	41	93
Sc	3.2	1.4	2.1	5.8	1.5	1.8	4.5	3.5	1.8	1.6	4.7	20
V	1.8	0.3	1.2	7.5	0.2	0.6	3.3	2.8	0.4	0.5	1.2	2.6
Cr	1.0	1.3	0.4	2.1	2.3	1.1	1.1	1.3	3.8	1.5	2.3	3.7
Co	0.6	0.2	0.4	2.1	0.2	0.5	1.0	1.3	0.6	0.5	0.4	1.1
Ni	0.3	0.1	0.3	1.7	0.2		0.0	0.3	0.1		0.7	0.3
Cu	4.9	2.3	4.2	6.5	5.2	9.0	3.0	14.7	12.7	7.8	5.5	13.3
Zn	95	56	70	97	64	58	101	86	31	49	88	129
Ga	25	18	20	21	20	19	23	22	22	20	17.5	21
Rb	124	124	119	83	161	126	106	122	153	164	96	98
Sr	60	21	34	76	12	35	67	54	32	39	182	232
Y	53	50	52	51	62	51	54	54	56	59	36	49
Zr	347	158	222	604	155	186	488	357	176	149	481	615
Nb	46	45	46	40	53	44	46	46	47	50	28	26
Cs	1.22	2.5	2.2	1.2	3.1	2.1	1.50	1.82	2.6	2.8	2.5	2.8
Ba	2398	676	1358	3374	301	1024	3021	2167	928	542	1575	1465
La	78	70	90	75	81	87	79	89	90	68	53	63
Ce	172	136	176	141	157	163	154	172	173	130	104	82
Pr	17.0	14.4	18.8	16.9	16.7	17.6	17.3	19	18.5	14.4	11.4	14.4
Nd	63	50	67	63	58	62	64	68	67	52	43	56
Sm	12.2	10.4	12.3	12.5	12.1	11.8	12.9	13	12.6	11.0	8.8	11.4
Eu	3.6	1.0	1.8	3.8	0.69	1.5	3.8	2.7	1.5	0.94	3.6	3.8
Gd	13.1	10.3	12.2	11.9	12.0	12.1	12.4	12.5	13.6	10.9	8.7	12.1
Tb	2.1	1.7	1.9	1.85	2.0	1.8	1.9	1.9	2.1	1.8	1.4	1.9
Dy	11.2	9.5	9.9	9.9	11.3	9.7	10.3	10.3	11.1	10.5	7.5	10.1
Ho	2.20	1.8	1.9	1.92	2.2	1.9	2.0	2.0	2.2	2.1	1.44	2.1
Er	6.4	5.7	5.8	5.7	6.8	5.8	6.2	6.0	6.6	6.3	4.2	6.0
Tm	0.89	0.80	0.80	0.81	0.94	0.79	0.84	0.83	0.92	0.89	0.56	0.83
Yb	5.7	5.1	5.1	5.0	6.0	5.0	5.5	5.3	6.0	5.6	3.5	5.5
Lu	0.83	0.96	0.91	1.01	1.05	0.96	1.02	0.96	0.86	0.92	0.65	0.84
Hf	9.8	6.3	7.5	14.2	6.4	6.9	13.1	10.1	6.4	6.0	10.9	12.2
Ta	1.6	4.1	3.6	3.0	4.5	3.7	3.3	3.4	1.4	3.8	2.2	0.88
Pb	25	31	28	21	36	25	23	23	27	40	29	32
Th	19.4	20	21	13.7	24	22	16.1	19.2	25	22	13.0	13.0
U	2.2	4.7	4.0	2.8	5.5	4.3	3.4	3.8	5.0	5.1	3.9	4.3
Rb/Sr	2.1	6.0	3.5	1.10	12.9	3.6	1.58	2.3	4.9	4.2	0.53	0.42
La/Yb	13.6	13.8	17.7	14.9	13.5	17.2	14.5	16.7	14.9	12.1	15.1	11.5
Eu*	0.86	0.30	0.45	0.94	0.18	0.38	0.90	0.63	0.36	0.26	1.25	0.98
1/Sr	0.017	0.048	0.029	0.013	0.080	0.029	0.015	0.019	0.032	0.025	0.005	0.004
1/Nd	0.016	0.020	0.015	0.016	0.017	0.016	0.016	0.015	0.015	0.019	0.023	0.018

Major elements and Ba by XRF; trace elements by solution ICP-MS (see Supplementary Material for details). Major element values are recalculated to 100 % but with the original totals and LOI figures given. Fe_2O_3 is total iron as determined by XRF. Full data are given in Electronic Appendix 3. See Table 1 for definition of clast types, and text for characterisation of compositional suites and their host magmatic systems. MS = magmatic system; DM = dense mafic clasts, Intr. = intrusive body cutting plastic, still-hot member C ignimbrite.

Table 2: continued

Sample	YP648	YR225	YP282	YP105	YP366	YP502	YP133	YP575	YP186	YP227	YP212
Locality	498	351	57	57	465	502	332	361	109	46	363
Host Unit	(C)	Intr	(C)	(C)	(C)	(C)	(C)	(A)	(A)	(B)	(B)
Clast type	J5	J6	J8	J8	J9	J9	J7	DM	DM	Scoria	Scoria
Suite	C1	C1	C2	C2	C2	C2	C3	M1	M1	M1	M2
Mag. sys	4	4	3	3	3	3	2	1	1	1	1
SiO_2	66.46	68.69	75.78	76.84	77.64	77.23	76.69	53.74	64.25	57.99	53.46
TiO_2	1.09	0.86	0.25	0.12	0.13	0.16	0.10	3.13	1.42	1.27	1.19
Al_2O_3	11.54	11.55	12.77	12.35	12.00	11.72	12.04	14.92	15.02	14.46	14.53
Fe_2O_3	10.68	9.05	2.80	1.62	1.32	1.98	1.55	13.48	9.20	9.19	13.32
MnO	0.15	0.13	0.05	0.02	0.01	0.06	0.02	0.08	0.21	0.15	0.20
MgO	0.47	0.26	0.05	0.04	0.00	0.02	0.25	1.02	0.55	4.32	4.33
CaO	3.91	3.58	0.81	0.43	0.35	0.35	1.45	5.69	1.69	7.23	6.77
Na_2O	2.91	3.02	2.72	2.85	3.55	3.43	3.03	4.00	3.04	3.65	3.87
K_2O	2.18	2.60	4.76	5.72	4.97	4.80	4.85	2.13	4.12	1.59	2.19
P_2O_5	0.38	0.26	0.03	0.01	0.02	0.01	0.02	1.81	0.50	0.15	0.15
Total	100.22	99.78	100.09	99.15	100.28	100.51	100.41	99.39	99.70	99.61	99.71
LOI	1.75	0.62	2.98	3.32	0.26	0.75	4.26	1.64	2.32	0.32	0.93
K/Na	0.84	0.96	1.96	2.25	1.57	1.57	1.79	0.59	1.52	0.49	0.63
Li	35	17.0	40	40	54	36	27	13.5	39	25	56
Sc	39	38	3.2	3	2	2.8	1.2	35	15.1	23	24
V	6.1	5.6	1.0	0.2	0.1	0.5	0.2	108	25	193	163
Cr	7.7	1.8	2.1	1.6	2.6	2.7	1.6	5.7	2.7	59	100
Co	6.3	4.7	0.5	0.7	0.1	0.2	0.3	12.7	11.7	28	16.6
Ni	0.9	0.8	0.5		0.1		0.1	4.6		39	25
Cu	8.7	8.8	15.9	43	2.2	5.7	6.5	17.9	14.1	31	16.2
Zn	103	130	83	70	63	62	48	400	196	192	432
Ga	16.9	20	19.0	18.5	17.8	19.1	21	28	28	23	27
Rb	57	89.8	101	138	126	143	175	39	65	46	55
Sr	245	307	108	18.6	16.9	47	25	334	113	183	166
Y	27	38	39	50	14.5	28	68	184	139	40	67
Zr	310	491	379	210	197	280	158	1689	761	185	61
Nb	17.0	26	28	32	30	28	60	31	47	26	87
Cs	7.9	2.4	3.2	4.8	2.9	3.0	3.6	0.73	1.55	1.02	1.13
Ba	798	952	2559	449	470	1520	98	3571	2539	477	388
La	32	45	59	70	35	41	42	132	182	52	97
Ce	65	92	110	134	54	114	89	157	180	102	140
Pr	7.5	10.8	12.6	15.1	7.6	9.2	10.4	34	42	11.6	23
Nd	29	42	47	55	28	34	39	145	166	45	87
Sm	6.3	8.7	9.7	11.4	5.6	7.0	10.0	33	34	9.2	17.3
Eu	2.4	3.3	3.3	0.89	1.05	2.1	0.38	9.8	5.4	1.78	1.55
Gd	6.3	8.5	9.2	11.3	4.8	6.6	10.5	36	36	10.1	18.5
Tb	1.0	1.25	1.40	1.76	0.74	1.04	2.0	5.9	5.5	1.53	2.8
Dy	5.3	7.1	7.7	9.6	3.7	5.6	11.9	35	30	8.6	15.1
Ho	1.02	1.40	1.50	1.86	0.67	1.09	2.4	7.3	5.9	1.71	2.9
Er	3.0	3.9	4.4	5.7	2.0	3.3	7.4	22	17.1	5.0	8.3
Tm	0.40	0.56	0.61	0.77	0.27	0.45	1.06	3.1	2.2	0.67	1.10
Yb	2.6	3.5	3.9	4.8	1.8	3.0	6.7	21	14.0	4.5	6.9
Lu	0.50	0.54	0.71	0.89	0.35	0.50	1.19	3.2	2.1	0.63	0.97
Hf	7.0	10	9.5	7.2	6.8	7.8	7.0	31	28	6.6	5.1
Ta	1.48	1.44	2.4	2.9	2.9	2.1	5.3	2.3	6.4	2.0	2.5
Pb	16.8	27	35	42	31	29	42	27	31	31	17.2
Th	7.7	10.6	15	20.0	17.9	17.1	25	7.3	19.1	12.8	8.5
U	2.5	3.1	4.0	6.0	4.1	4.2	6.4	1.91	5.2	2.2	1.58
Rb/Sr	0.23	0.29	0.94	7.44	7.47	3.02	7.1	0.12	0.58	0.25	0.33
La/Yb	12.4	12.6	15.1	14.5	19.8	13.9	6.2	6.3	13.1	11.7	13.9
Eu*	1.17	1.18	1.05	0.24	0.62	0.93	0.11	0.87	0.47	0.56	0.26
1/Sr	0.004	0.003	0.009	0.054	0.059	0.021	0.041	0.0030	0.0089	0.0055	0.0060
1/Nd	0.034	0.024	0.021	0.018	0.036	0.030	0.026	0.0069	0.0060	0.0060	0.0115

Table 3: Representative single clast isotopic ratios for silicic juvenile components from members A, B and C in the HRT

Sample	Host unit	Clast type	Suite	SiO_2 wt%	Rb ppm	Sr ppm	$^{87}Sr/^{86}Sr$	2se	$^{143}Nd/^{144}Nd$	2se	$^{206}Pb/^{204}Pb$	2se	$^{207}Pb/^{204}Pb$	2se	$^{208}Pb/^{204}Pb$	2se
YP459	(A)	J1	A1	77.30	124	21	0.71213	3.6E-06	0.51215	6.6E-06	17.01	8.0E-04	15.49	8.8E-04	38.06	2.6E-03
YP457	(A)	J1	A1	74.10	110	38	0.71163	3.6E-06	0.51216	4.5E-06	17.01	8.5E-04	15.49	9.9E-04	38.05	3.0E-03
YP255	(A)	J1	A3	77.00	161	12.5	0.71256	6.0E-06	0.51214	2.3E-06	17.02	9.6E-04	15.50	1.1E-03	38.06	3.4E-03
YP251	(A)	J2	A1	75.01	119	34	0.71188	3.5E-06	0.51216	2.9E-06	16.99	8.2E-04	15.49	9.2E-04	38.05	2.7E-03
YP191	(A)	J3	A2	69.87	83	76	0.71009	3.9E-06	0.51220	2.5E-06	16.95	1.0E-03	15.48	1.3E-03	38.02	3.9E-03
YP078	(B)	J1	B1	76.27	126	35	0.71179	3.8E-06	0.51215	2.7E-06	16.99	2.2E-03	15.49	3.0E-03	38.03	9.6E-03
YP208	(B)	J1	B1	72.23	98	54	0.71091	4.1E-06	0.51219	3.6E-06	16.98	1.1E-03	15.49	1.3E-03	38.03	3.9E-03
YP061	(B)	J4	B1	71.43	106	67	0.71076	2.6E-06			16.90	5.4E-03	15.46	5.2E-03	37.95	1.4E-02
YP299	(C)	J5	C1	69.39	46	228	0.72486	3.5E-06	0.51172	2.7E-06	18.16	1.3E-03	15.76	1.5E-03	37.88	4.7E-03
YP648	(C)	J5	C1	66.46	57	245	0.72464	3.4E-06	0.51174	8.0E-06	18.16	8.8E-04	15.75	9.2E-04	37.92	2.6E-03
YP282	(C)	J8	C2	75.78	108	39	0.72590	3.9E-06	0.51172	2.6E-06	17.91	1.1E-03	15.70	1.4E-03	37.90	4.2E-03
YP105	(C)	J8	C2	76.84	138	18.6	0.72735	4.1E-06	0.51170	2.8E-06	17.89	1.5E-03	15.69	1.8E-03	37.89	5.7E-03
YP133	(C)	J7	C3	76.69	175	25	0.71102	3.7E-06	0.51214	2.6E-06	16.99	1.4E-03	15.48	1.8E-03	38.03	5.8E-03

For analytical details, see Supplementary Material, and for full data set see Electronic Appendix 3. $^{87}Sr/^{86}Sr$ values are age-corrected to 2.08 Ma, using measured parent-daughter rations (EA 3).

Table 4: Distinguishing geochemical and petrological characteristics of the four HRT magmatic systems

Magmatic system	Members, suites and clast types	Major element characteristics	Trace element characteristics	Isotopic characteristics	Glass characteristics	Crystal characteristics
1	Members A and B. Suites A1 (J1-, J2-type clasts) and A2 (J3-type) in member A, that are linked in member B by suite B1 (J1-, J3- and J4-type clasts)	• High in alkalis, and Al_2O_3 • Depleted in FeO, CaO	• Large range in Ba and Zr • Low Sr and Sc abundances • None to negative Eu anomaly	• Moderately radiogenic isotope systematics • Increasing $^{87}Sr/^{86}Sr$ with increasing 1/Sr, decreasing Ba • Constrained Pb isotopic ratios identical to HRT mafics	• Clustered compositions • Similar to FGC/OGC3 and IGC2-8 in the fall deposit and basal ignimbrite • Suite A2 unique to member A; gap with A1 infilled by J4-type pumices in member B	• >0.4 mol% Cn in sanidines • Orthopyroxene cores/inclusions, clinopyroxene rims • Olivines in J4-type clasts have higher CaO
2	Members A and C. Suites A3 (J1-type pumices) and C3 (J7-type clasts)	• Similar to magmatic system 1	• Elevated Nb, Rb • Low Ba, Sr, LREE • Moderate to high negative Eu anomaly	• Similar to system 1 for Pb and Nd isotopes and Sr in member A • Regeneration in member C contains less radiogenic $^{87}Sr/^{86}Sr$	• Low Ba and Sr (similar to FGC/OGC1+2 and IGC1)	• Low (<0.35 mol%) Cn sanidines • Lower MgO olivines relative to system 1
3	Member C. Suite C2 comprised of J8-type pumices together with J9- and rare J5-type clasts	• Offset to higher SiO_2 from the system 1 trends • Low in alkalis • Moderate in FeO and TiO_2	• Trend back to higher Ba, Sr, Zr • Low Nb, LREE • No Eu anomaly to moderately –ve Eu anomaly	• Highly radiogenic isotopic systematics • Negative $^{208}Pb/^{204}Pb$ correlation with $^{206}Pb/^{204}Pb$ • Positive correlation between $^{87}Sr/^{86}Sr$ and 1/Sr	• Clustered compositions • Offset to higher Ba, Sr and lower La, Zr compared to system 1 • Negatively correlated Ba and La	• Fe-rich olivines and clinopyroxenes • High Cn sanidine
4	Member C. Suite C1 comprised of J5- and J6-type juvenile clasts	• Elevated in FeO, CaO, P_2O_5 and TiO_2 • Low in Al_2O_3 and alkalis	• Elevated in Sr and Sc • Low in Ba, Zr, Nb and LREE • No Eu anomaly	• Highly radiogenic isotopic systematics • Negative $^{208}Pb/^{204}Pb$ correlation with $^{206}Pb/^{204}Pb$ • Positive correlation between $^{87}Sr/^{86}Sr$ and 1/Sr	• N/A- only ever found as devitrified clasts	• Continuum in compositions between orthopyroxene and clinopyroxene • Calcic plagioclase

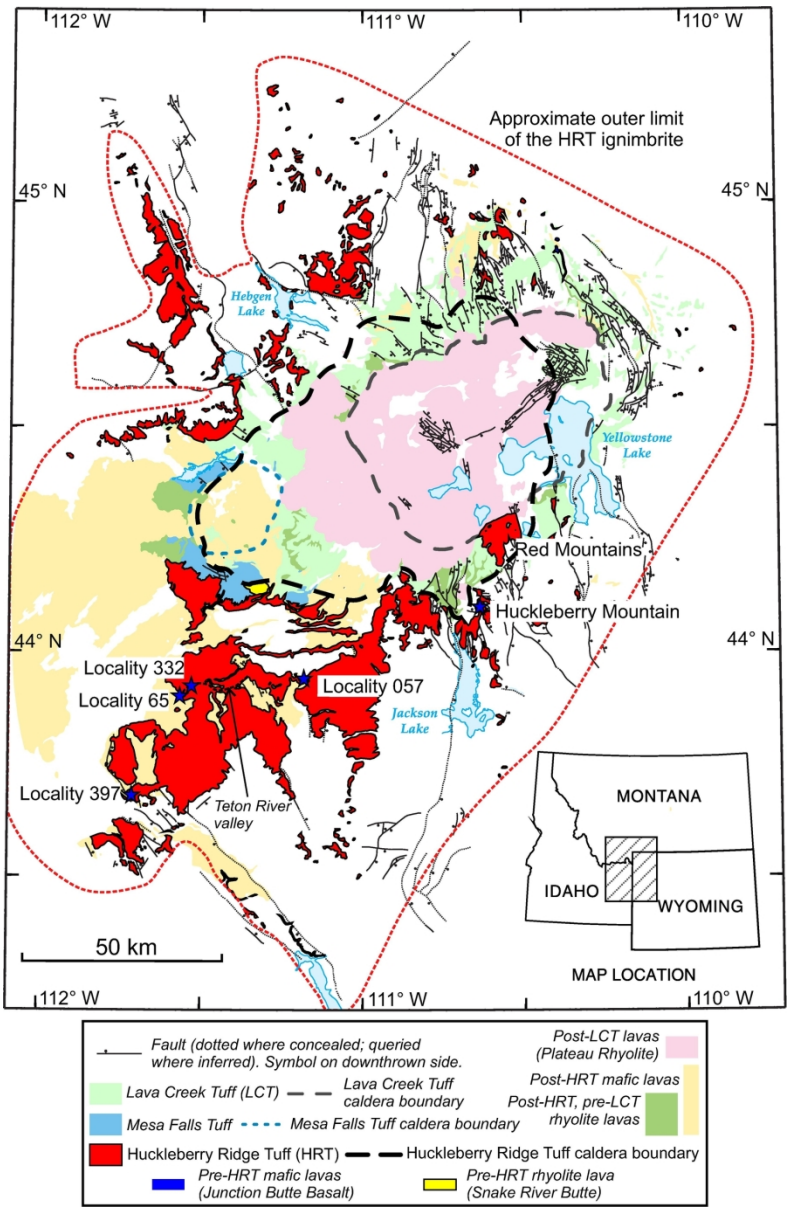

Swallow et al. Figure 1 revised

140x214mm (300 x 300 DPI)

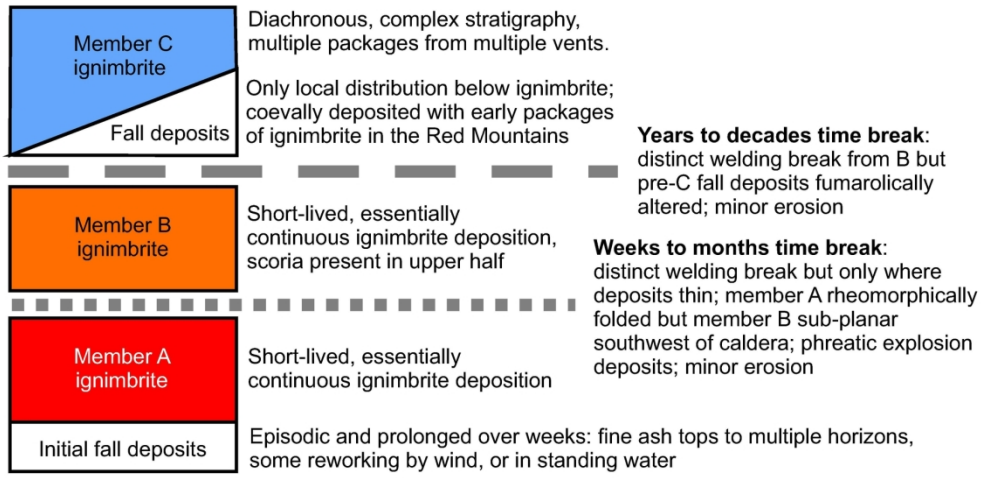

Swallow et al. Figure 2 revised

165x87mm (300 x 300 DPI)

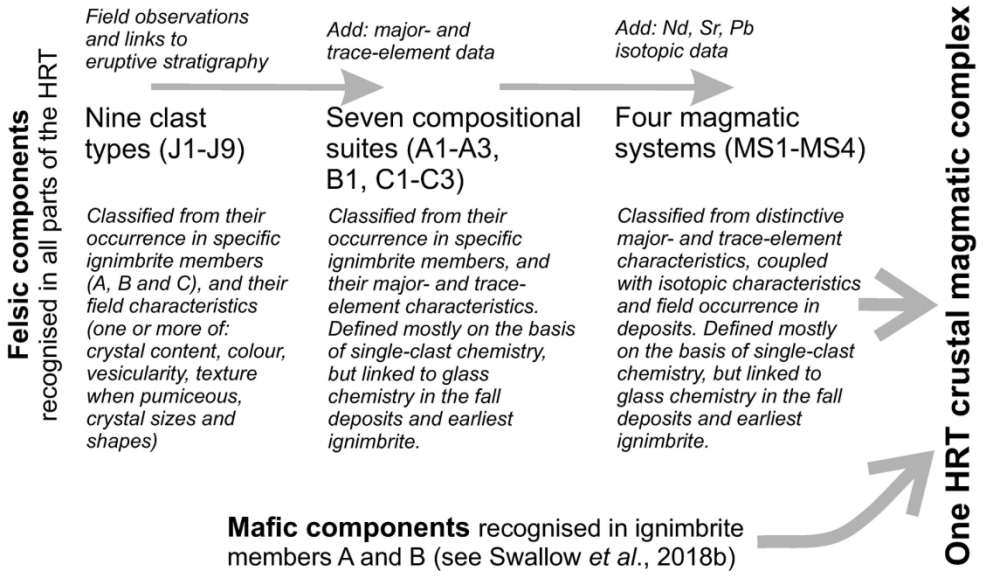

Swallow et al. Figure 3 revised

160x93mm (300 x 300 DPI)

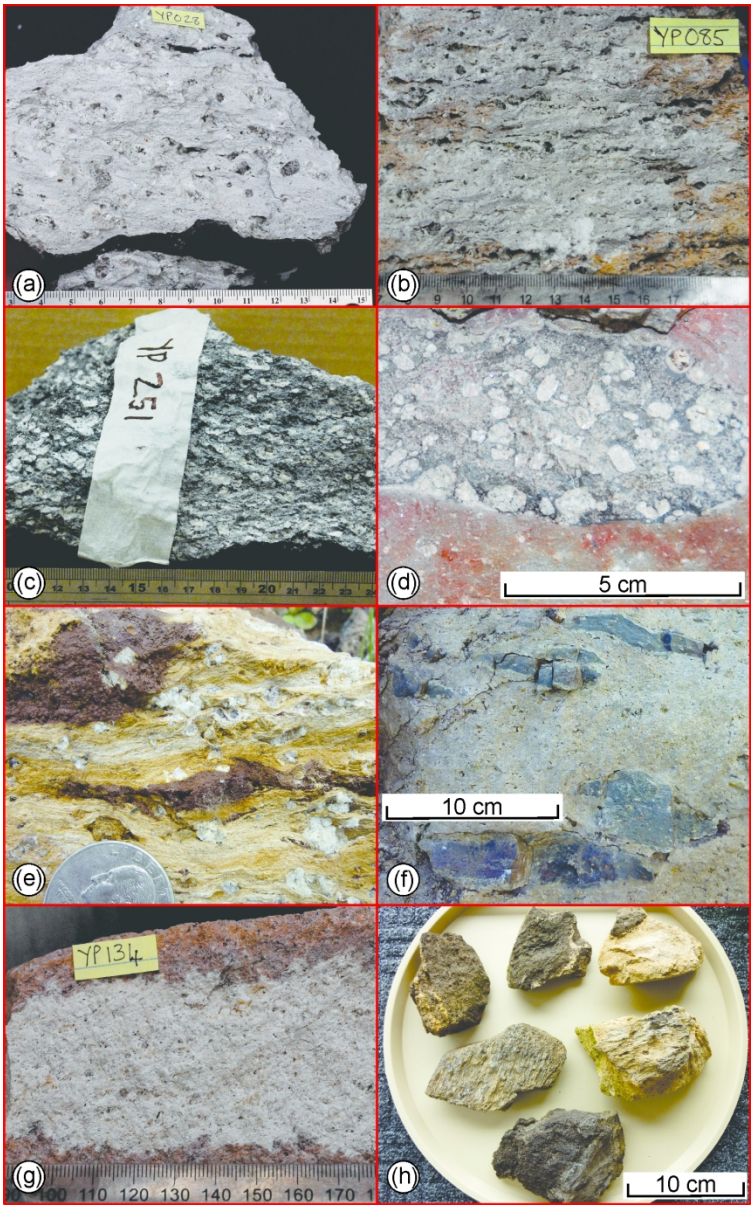

Swallow et al. Figure 4 revised

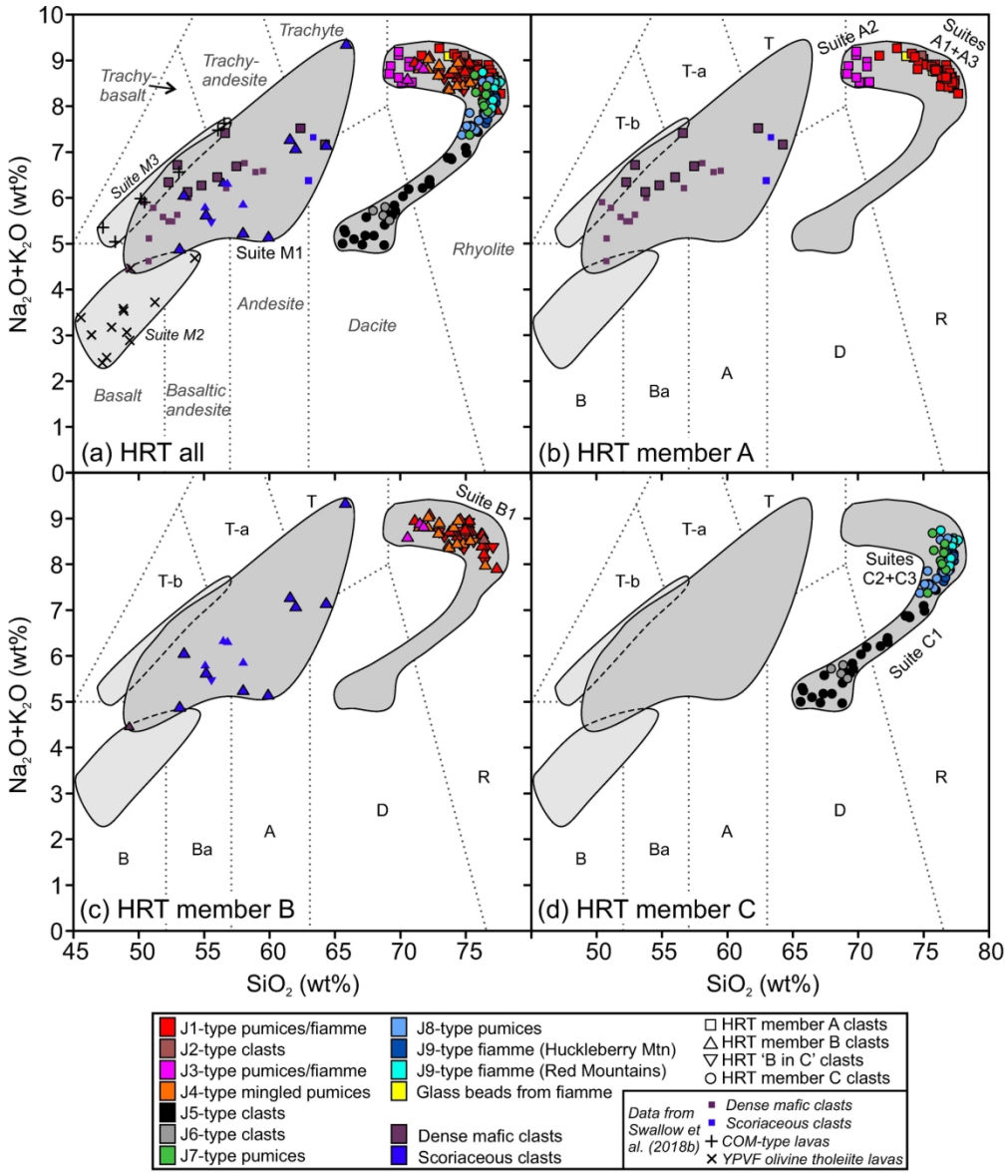

Swallow et al. Figure 5 revised

165x193mm (300 x 300 DPI)

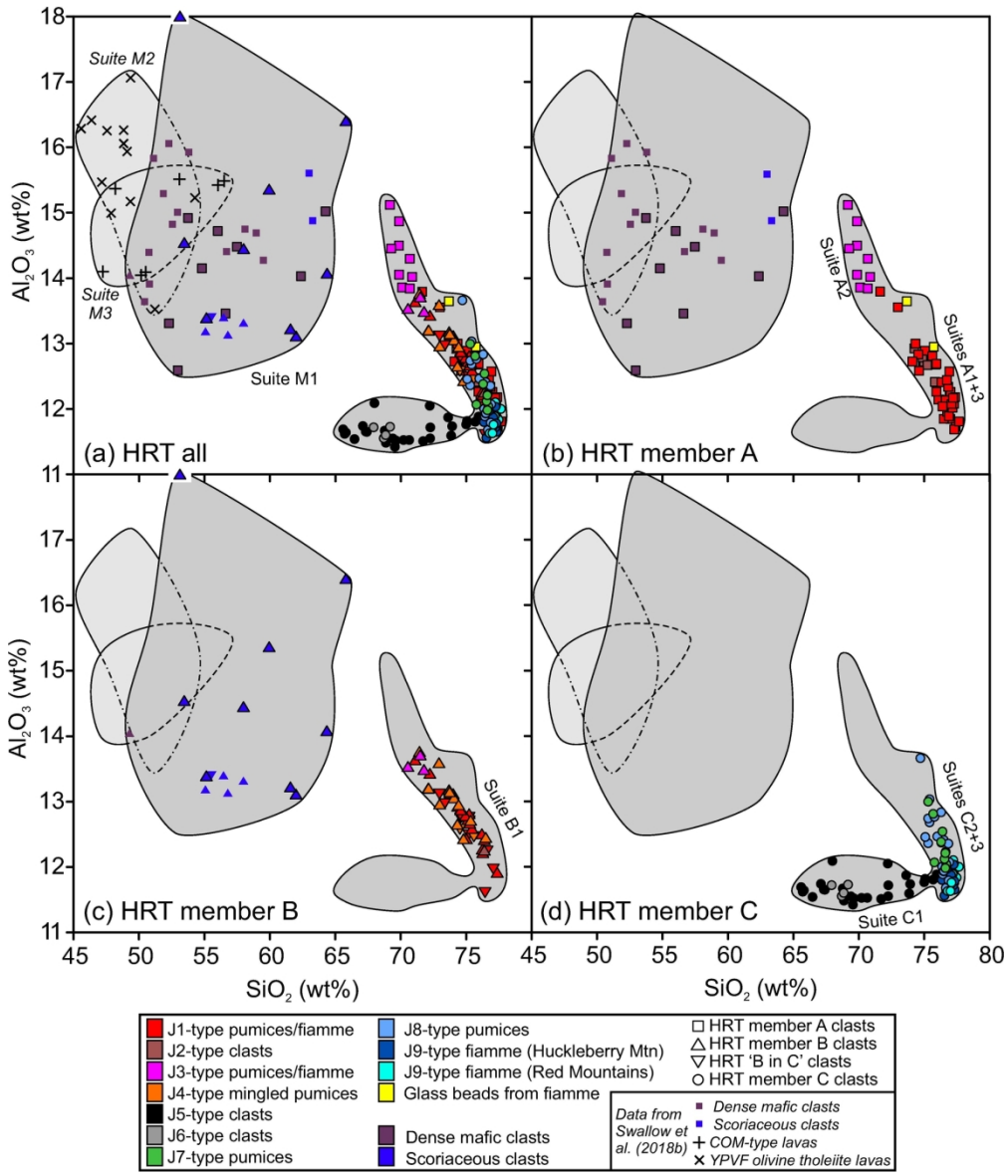

Swallow et al. Figure 6 revised

165x193mm (300 x 300 DPI)

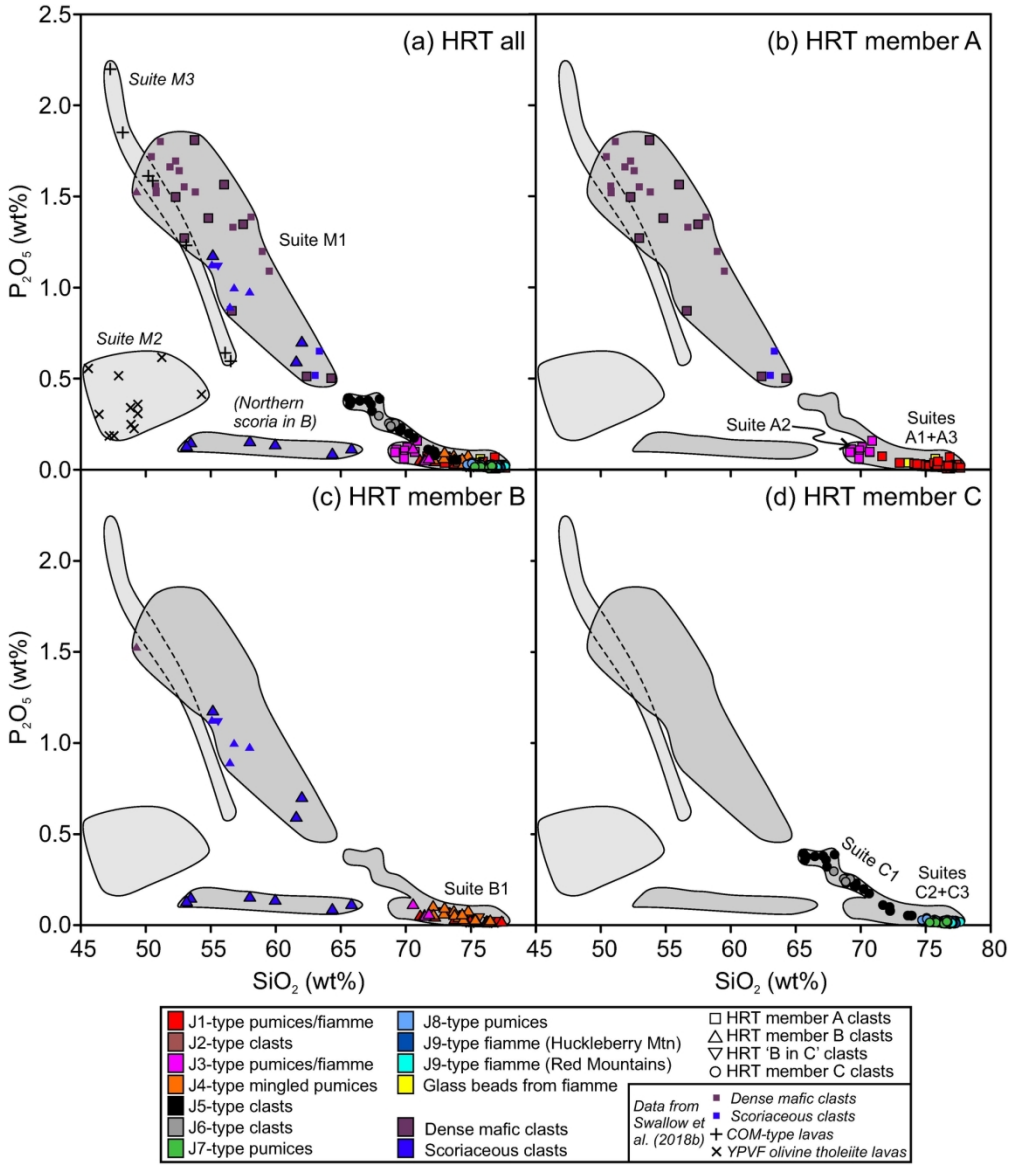

Swallow et al. Figure 7 revised

165x191mm (300 x 300 DPI)

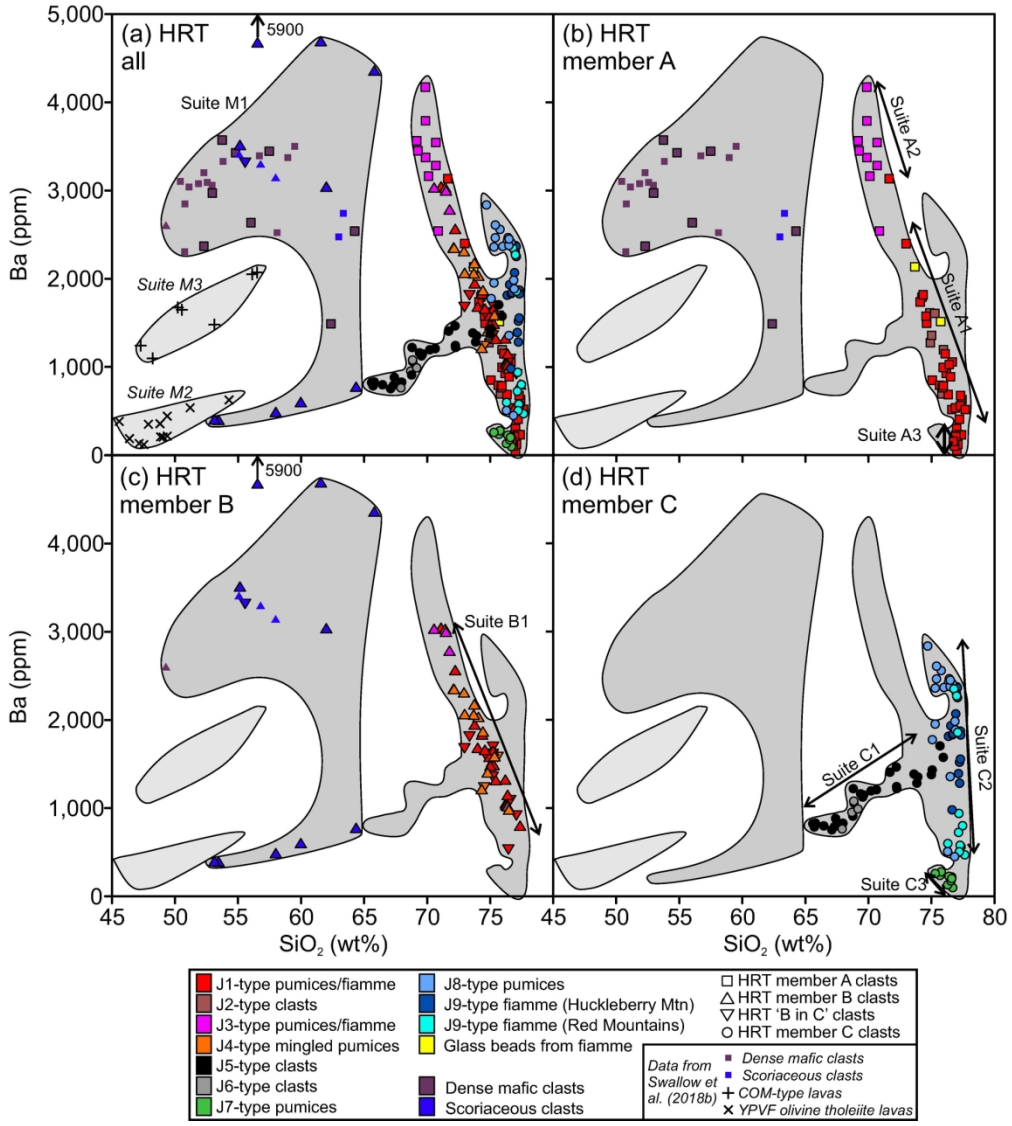

Swallow et al. Figure 8 revised

165x184mm (300 x 300 DPI)

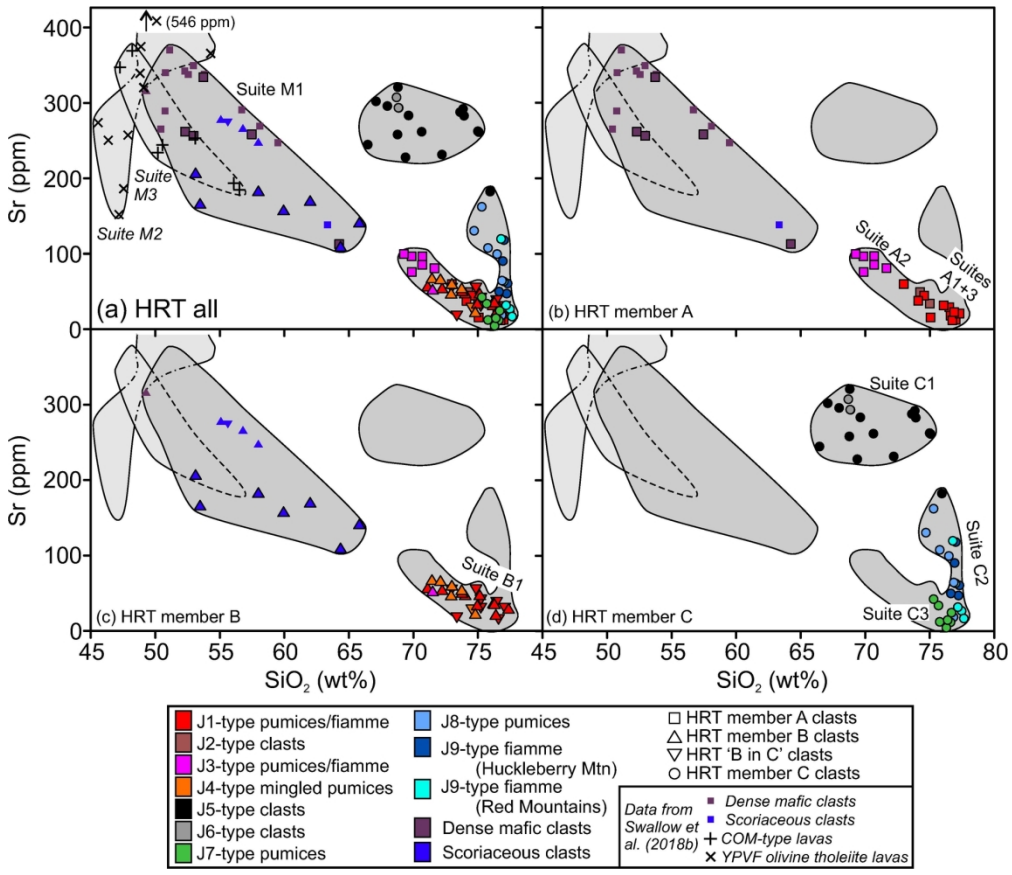

Swallow et al. Figure 9 revised

165x142mm (300 x 300 DPI)

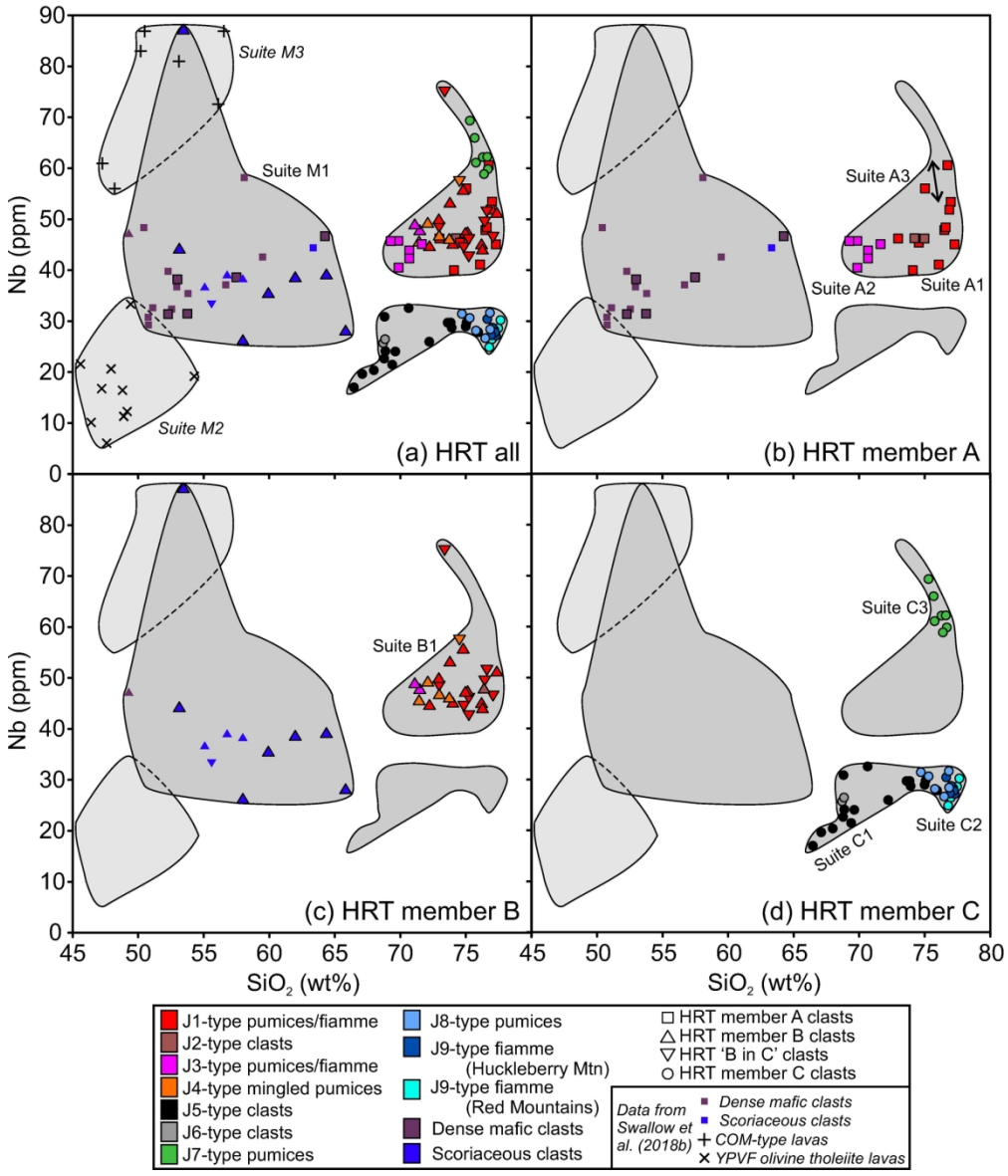

Swallow et al. Figure 10 revised

165x193mm (300 x 300 DPI)

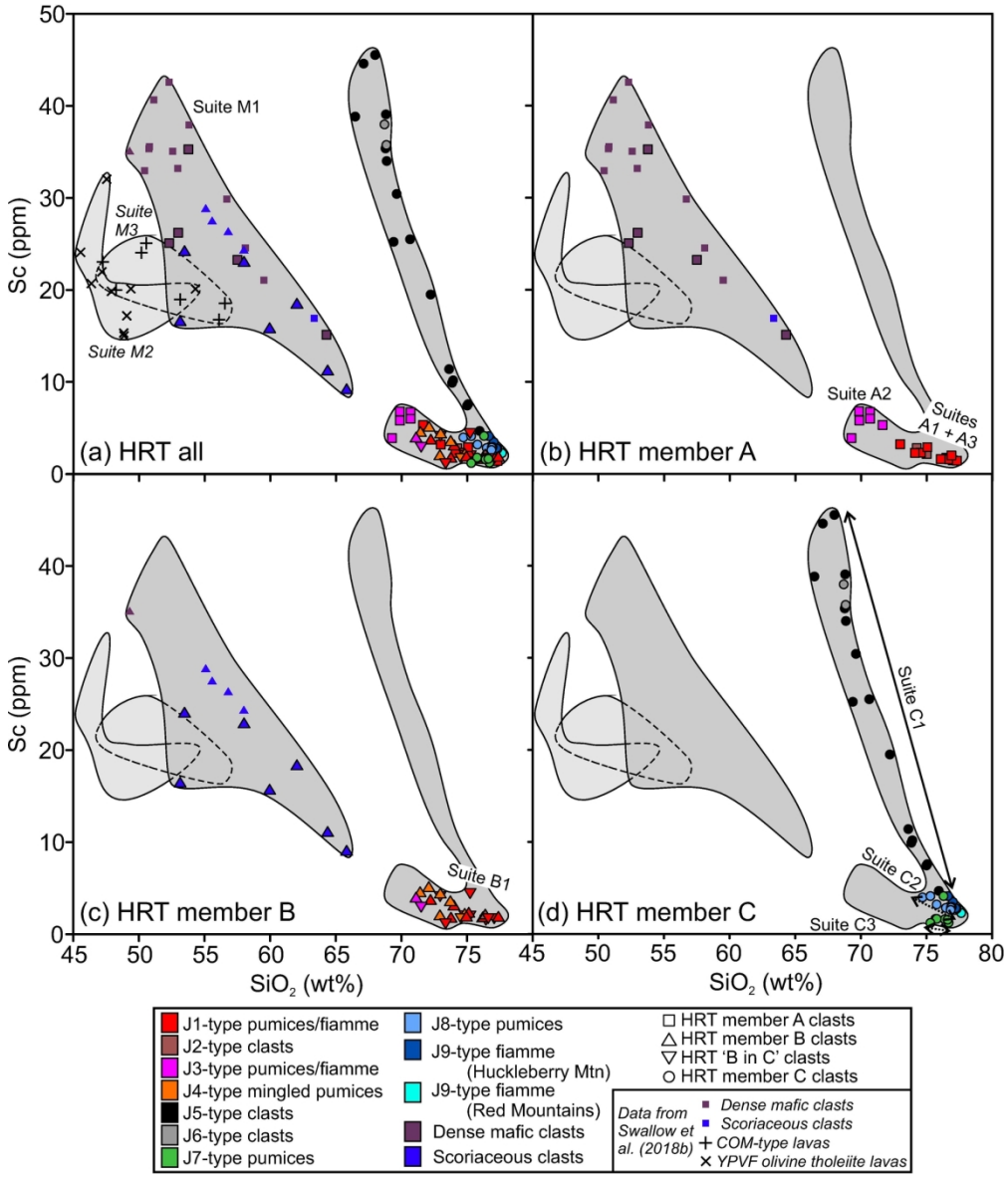

Swallow et al. Figure 11 revised

165x193mm (300 x 300 DPI)

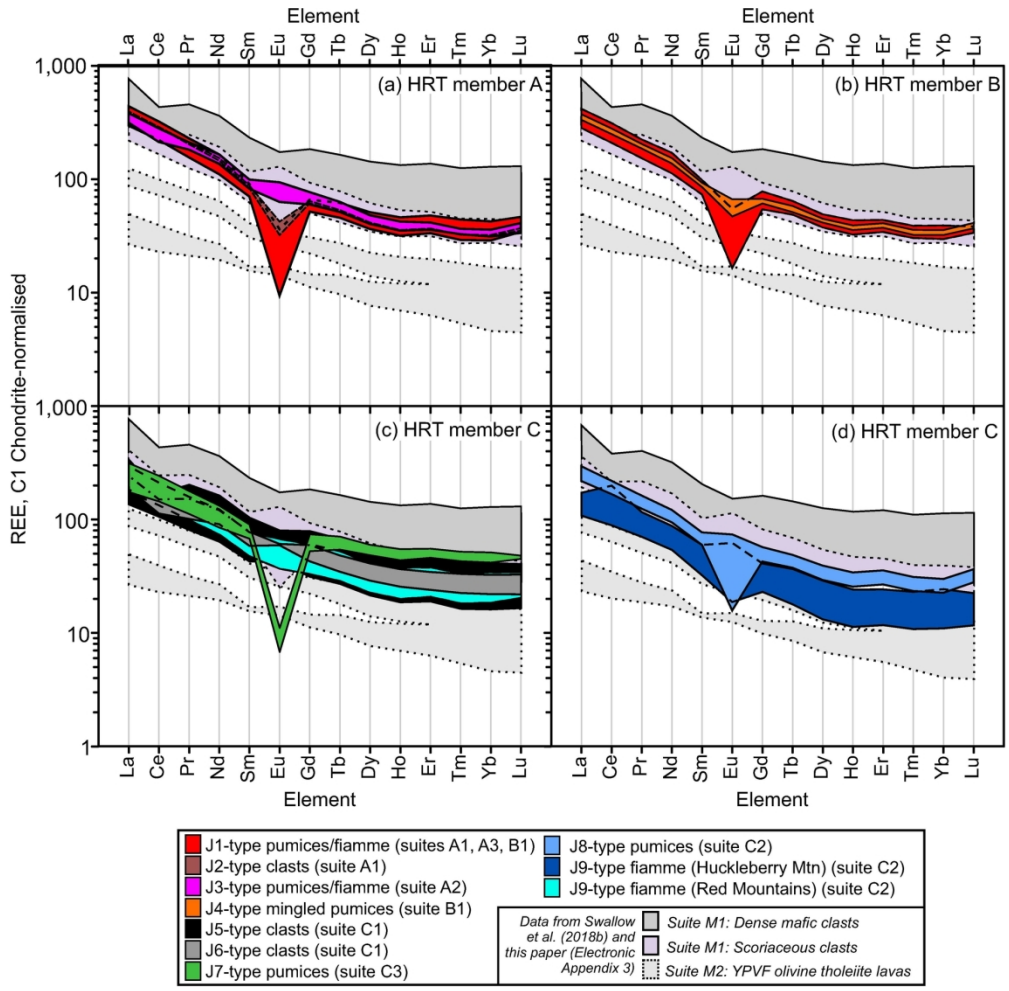

Swallow et al. Figure 12 revised

165x162mm (300 x 300 DPI)

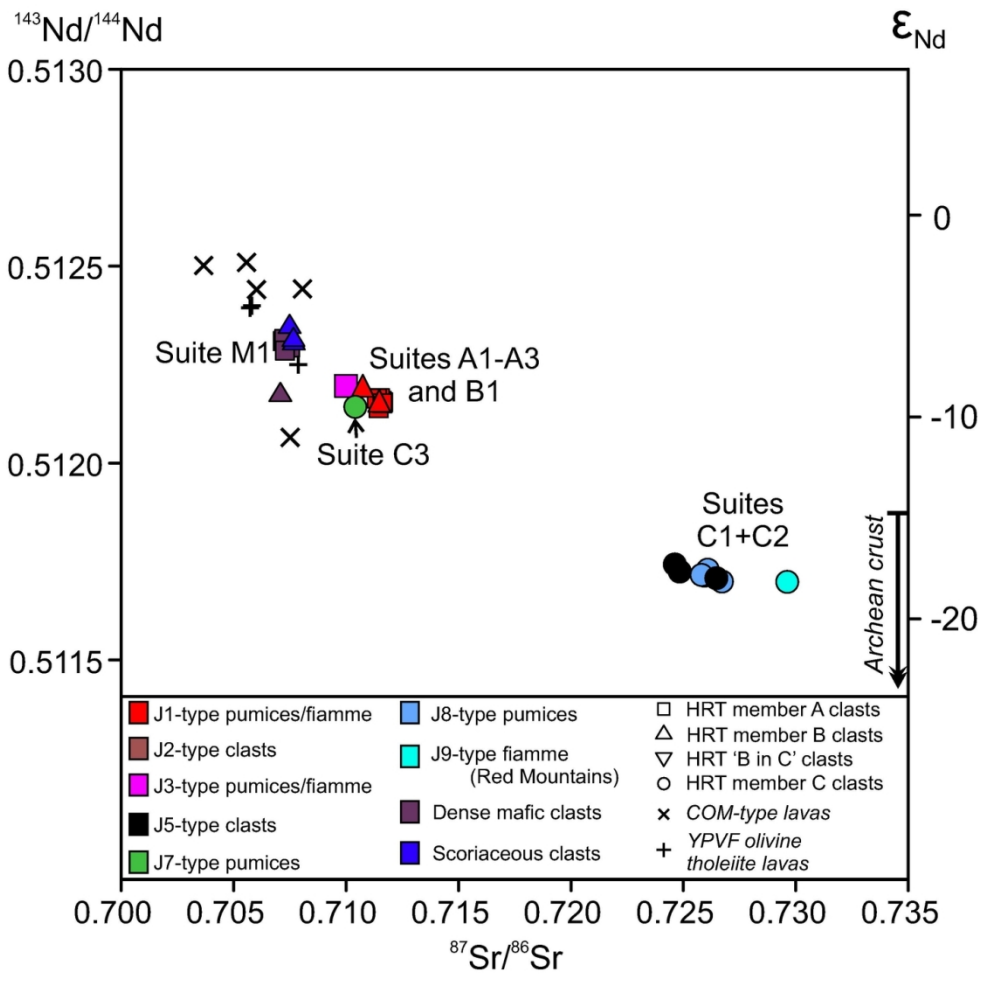

Swallow et al. Figure 13 revised

123x121mm (300 x 300 DPI)

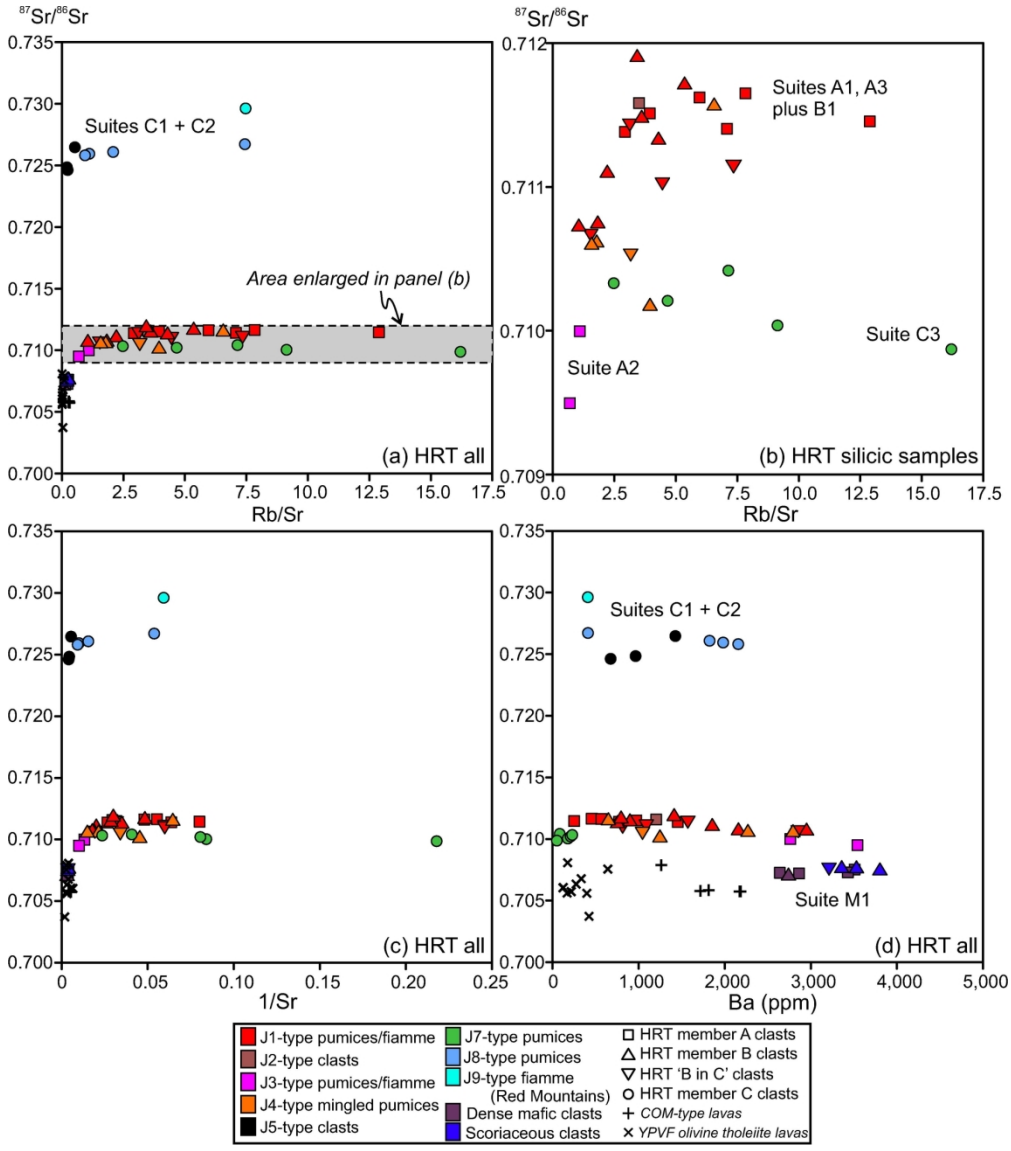

Swallow et al. Figure 14 revised

165x187mm (300 x 300 DPI)

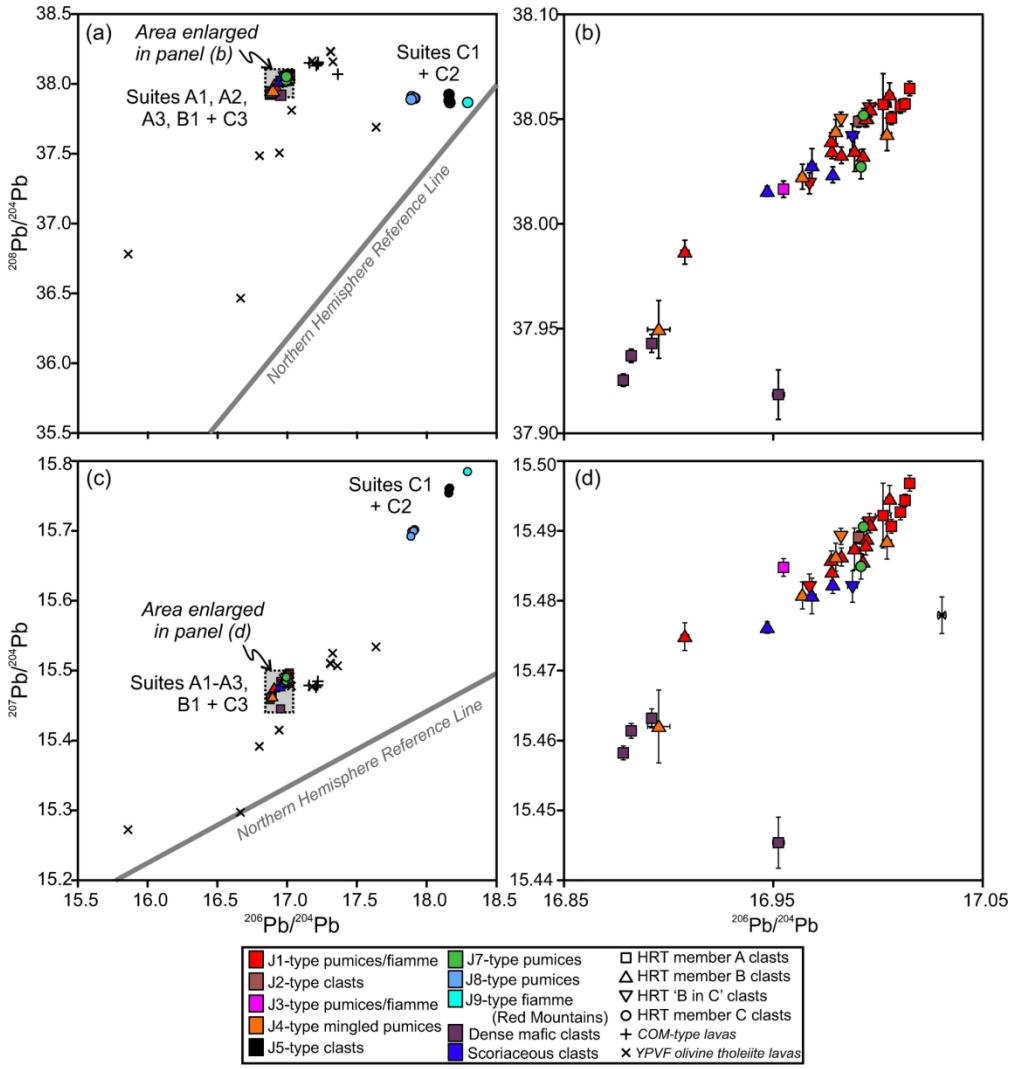

Swallow et al. Figure 15 revised

165x174mm (300 x 300 DPI)

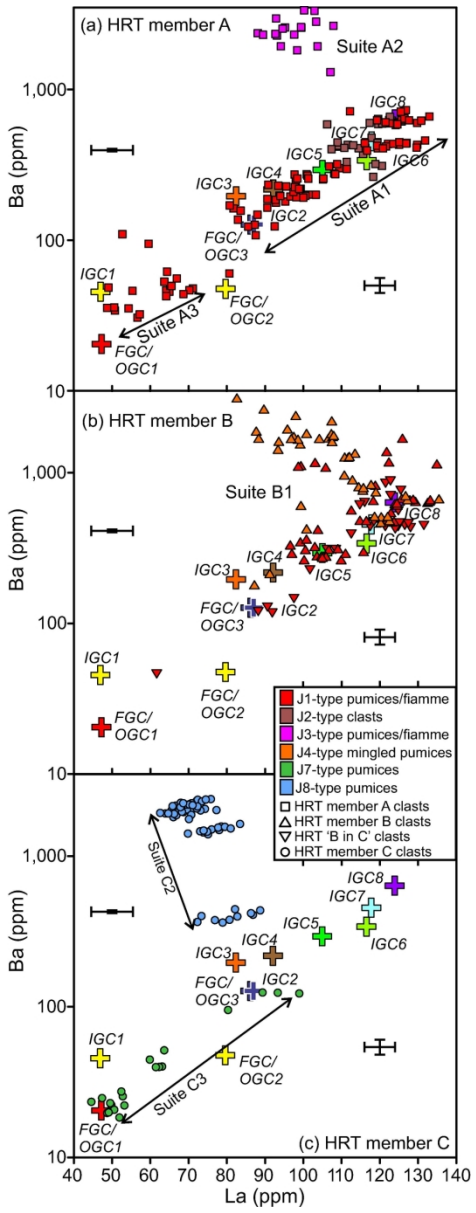

Swallow et al. Figure 16 revised

82x214mm (300 x 300 DPI)

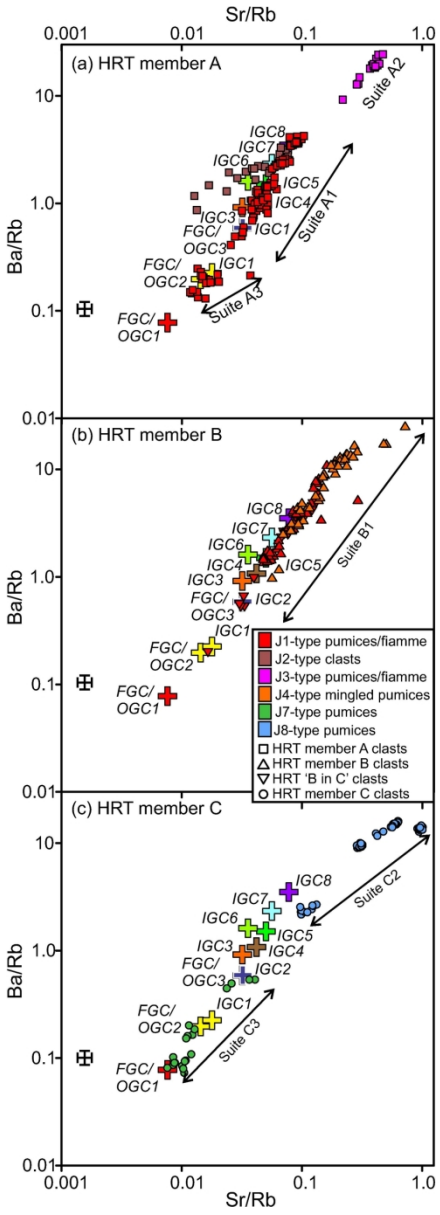

Swallow et al. Figure 17 revised

76x214mm (300 x 300 DPI)

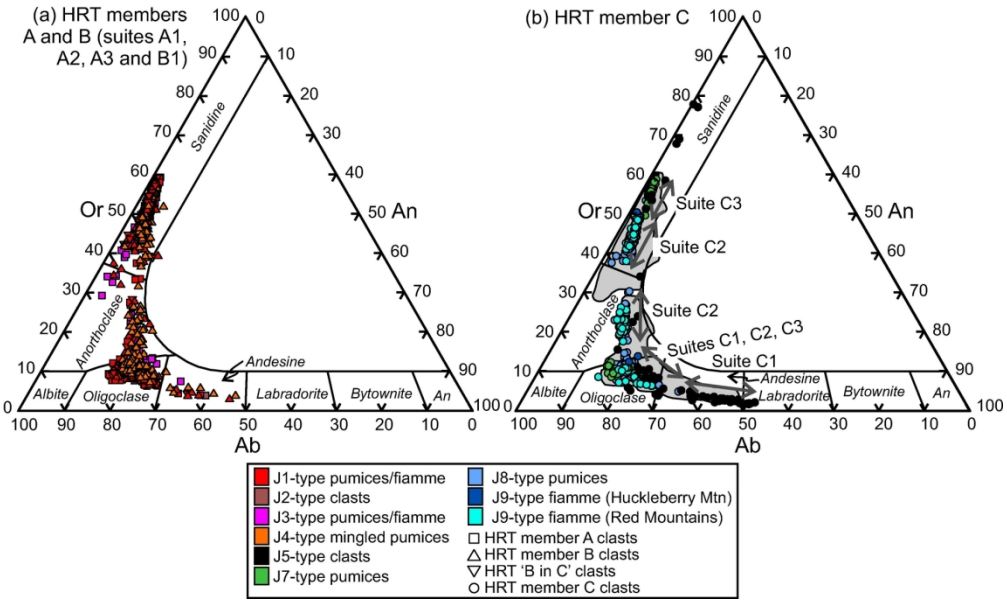

Swallow et al. Figure 18 revised

165x97mm (300 x 300 DPI)

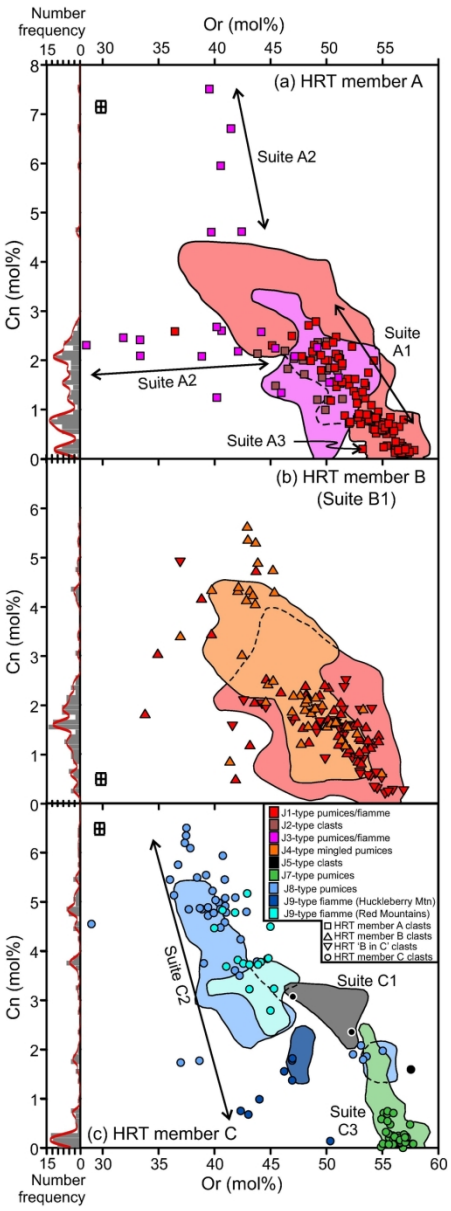

Swallow et al. Figure 19 revised

79x214mm (300 x 300 DPI)

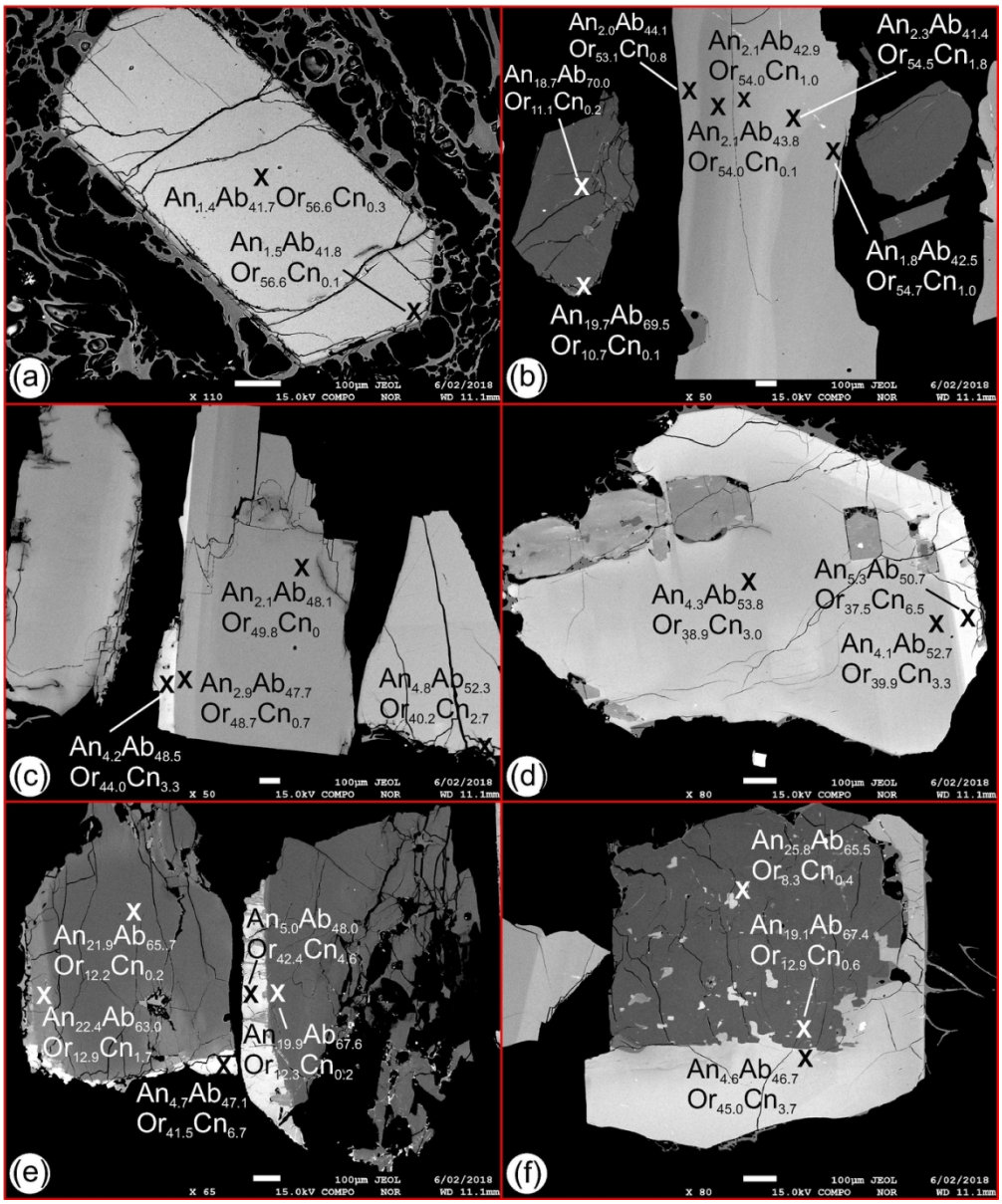

Swallow et al. Figure 20 revised part 1 of 2

116x139mm (300 x 300 DPI)

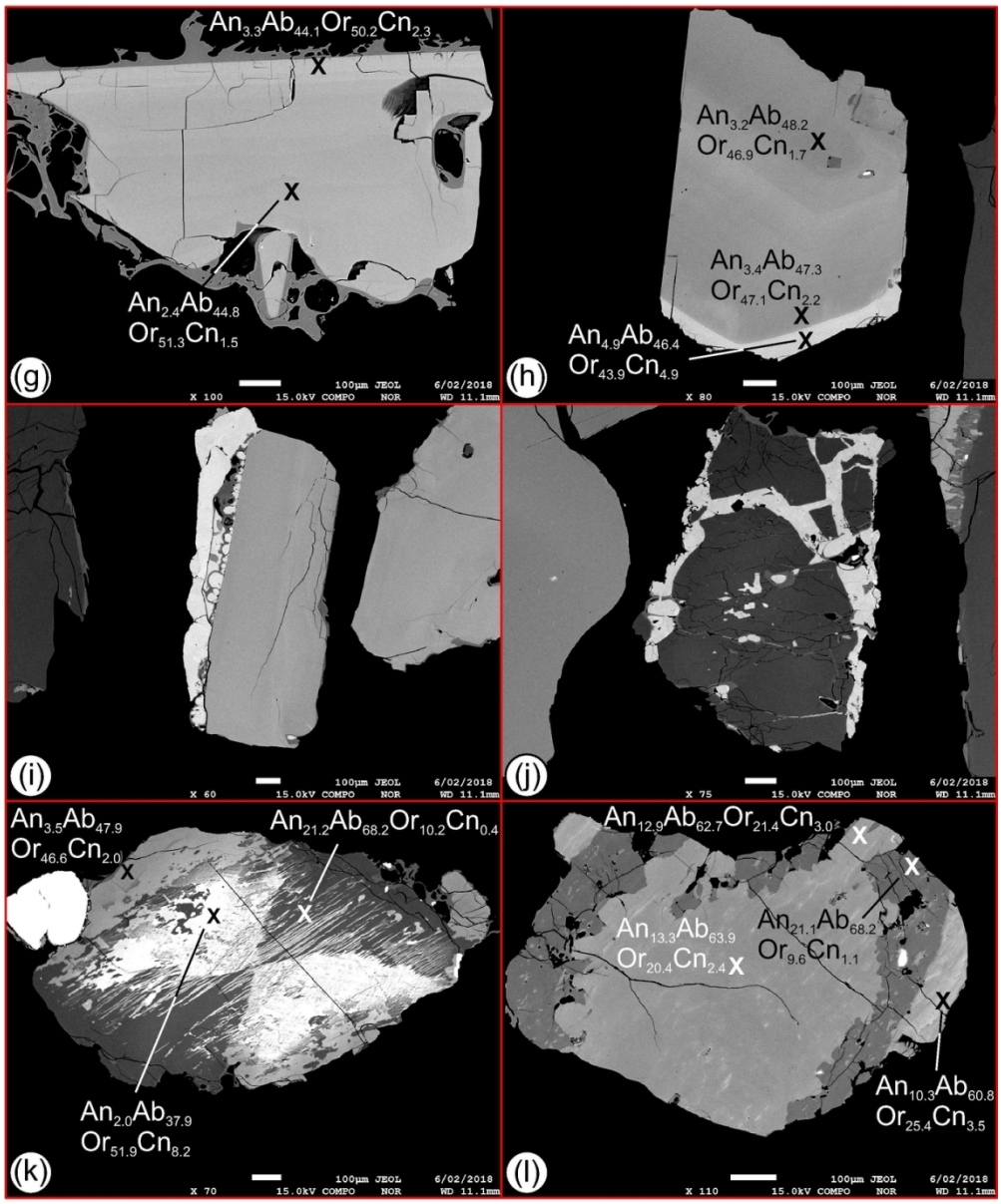

Swallow et al. Figure 20 revised part 2 of 2

116x140mm (300 x 300 DPI)

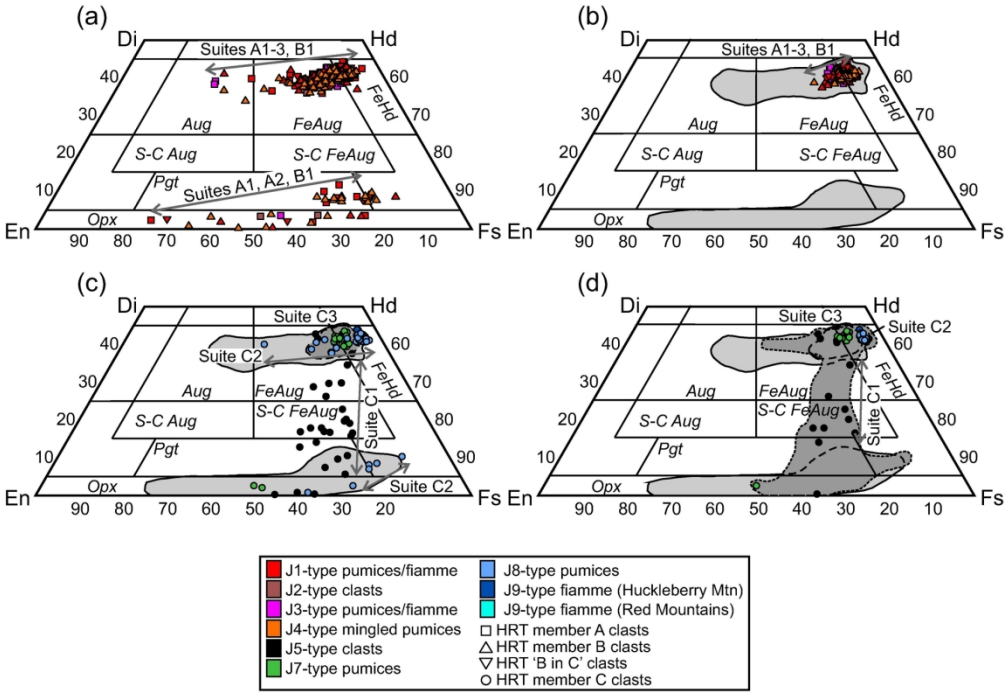

Swallow et al. Figure 21 revised

165x113mm (300 x 300 DPI)

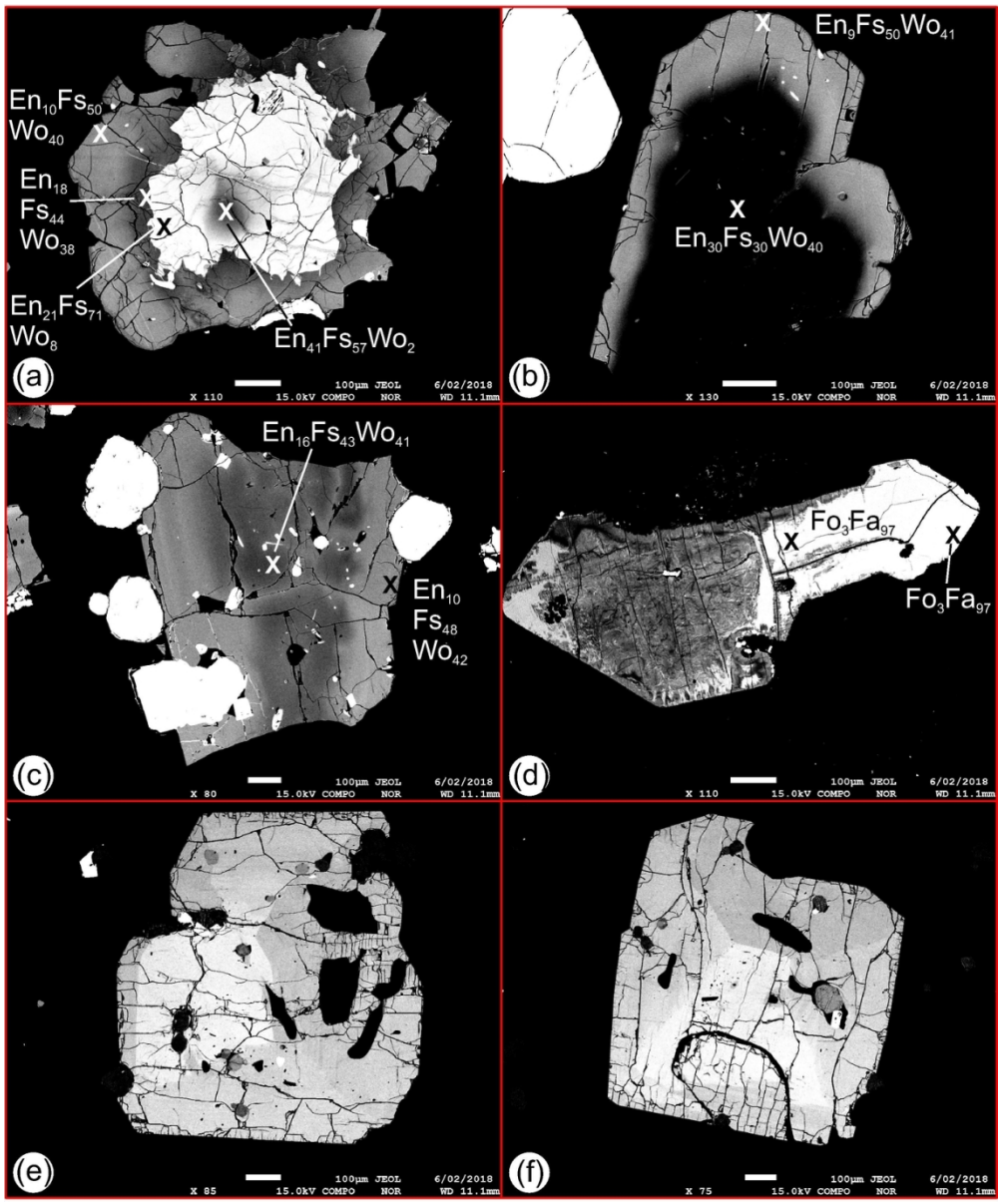

Swallow et al. Figure 22 revised

116x140mm (300 x 300 DPI)

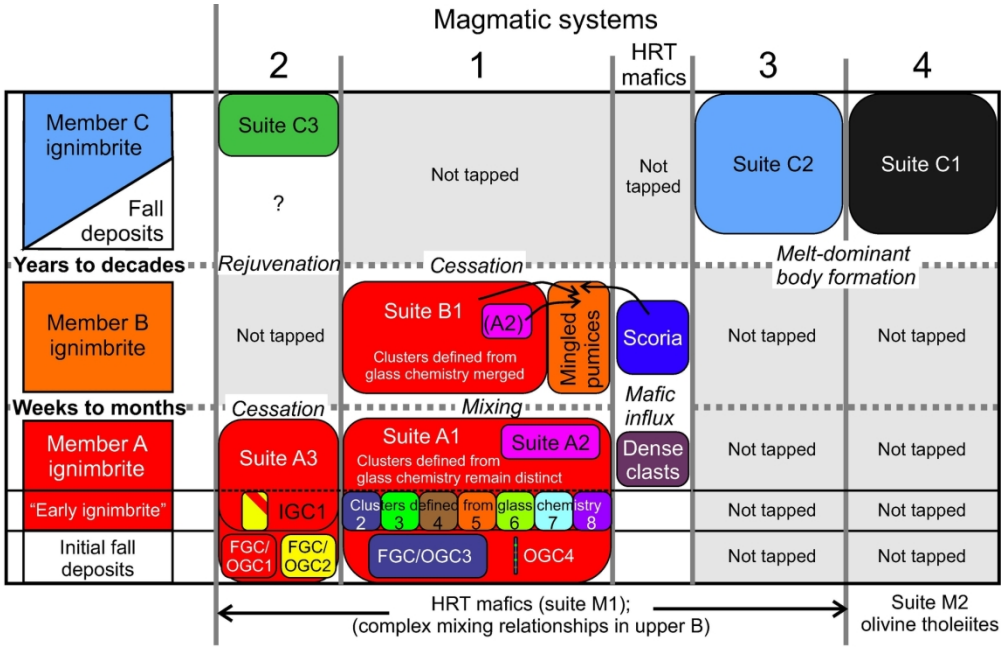

Swallow et al. Figure 23 revised

165x106mm (300 x 300 DPI)

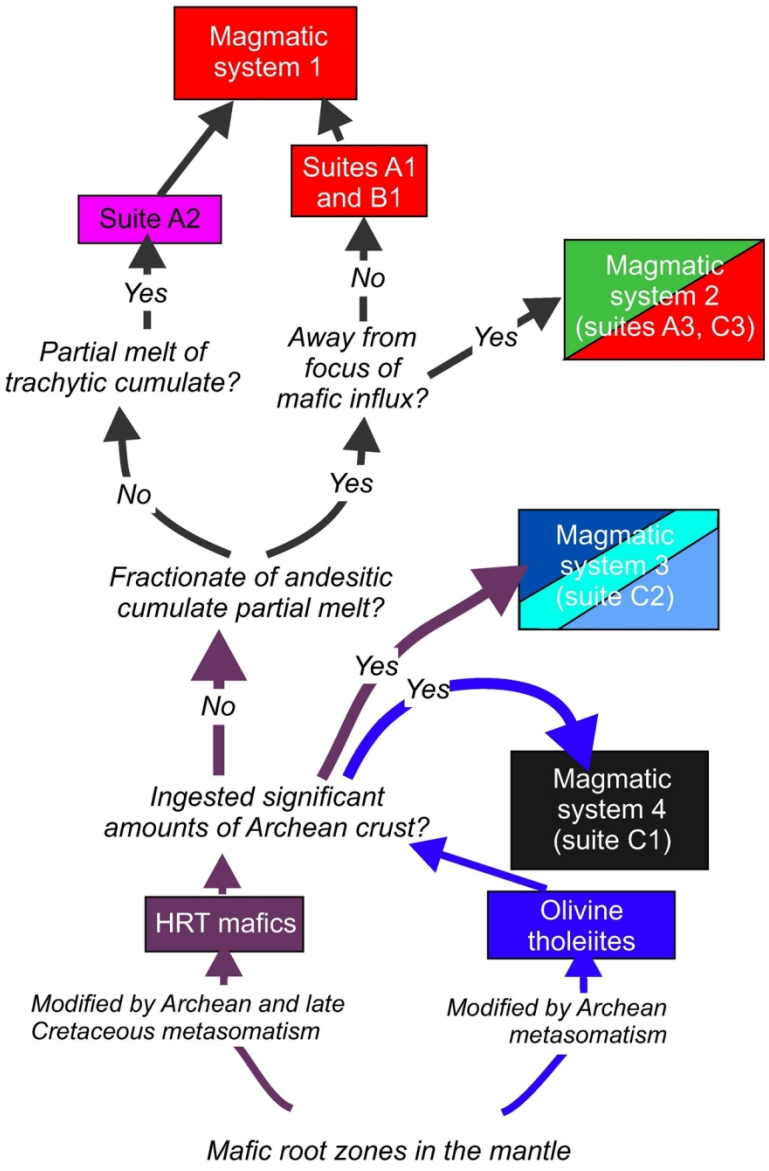

Swallow et al. Figure 24 revised

109x166mm (300 x 300 DPI)

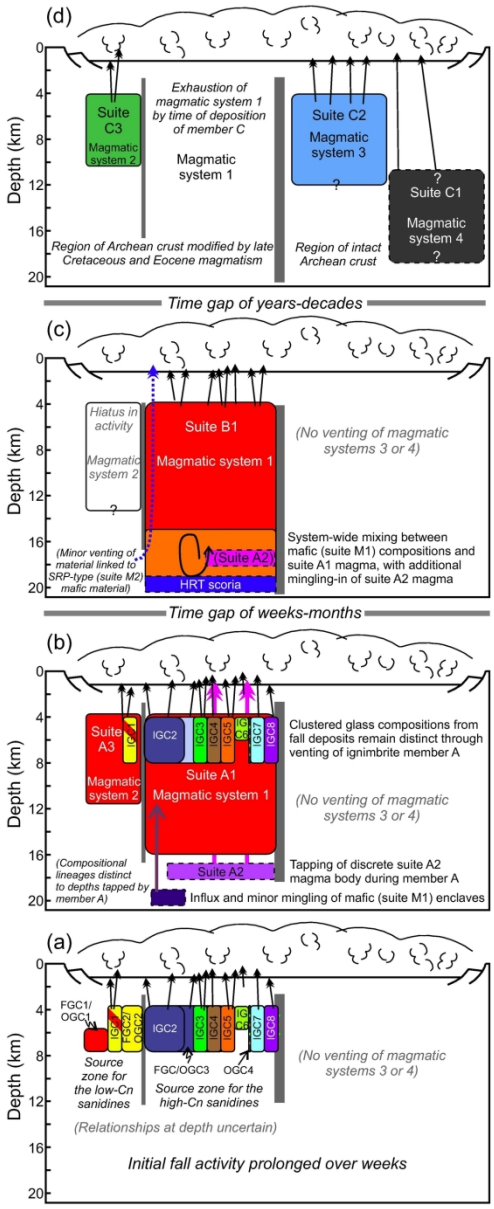

Swallow et al. Figure 25 revised

97x238mm (300 x 300 DPI)

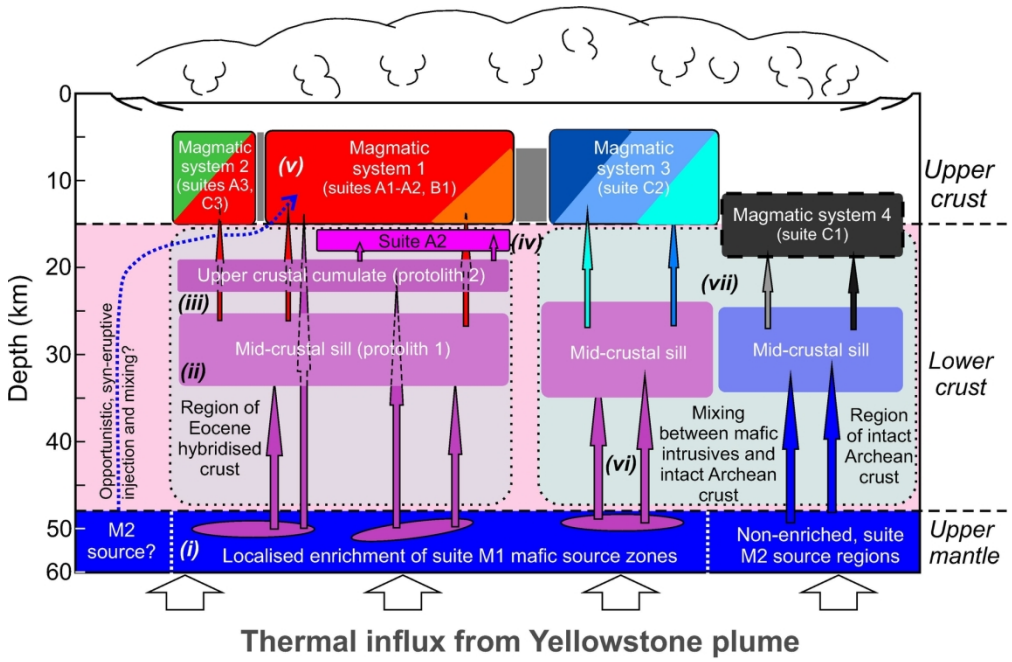

Swallow et al. Figure 26 revised

163x107mm (300 x 300 DPI)